

# VLT/VIMOS integral field spectroscopy of luminous and ultraluminous infrared galaxies: 2D kinematic properties<sup>\*</sup>

Enrica Bellocchi<sup>1</sup>, Santiago Arribas<sup>1</sup>, Luis Colina<sup>1</sup>, and Daniel Miralles-Caballero<sup>2</sup>

<sup>1</sup> Centro de Astrobiología, Departamento de Astrofísica, CSIC-INTA, Cra. de Ajalvir Km. 4, 28850 Torrejón de Ardoz, Madrid, Spain

e-mail: [bellocchie@cab.inta-csic.es](mailto:bellocchie@cab.inta-csic.es)

<sup>2</sup> Instituto de Física Teórica, Universidad Autónoma de Madrid, 28049 Madrid, Spain

Received 29 December 2012 / Accepted 21 June 2013

## ABSTRACT

**Context.** (Ultra) Luminous infrared galaxies [(U)LIRGs] host the most extreme star-forming events in the present universe and are places where a significant fraction of the past star formation beyond  $z \sim 1$  has occurred. The kinematic characterization of this population is important to constrain the processes that govern such events.

**Aims.** We present and discuss the 2D kinematic properties of the ionized gas (H $\alpha$ ) in sample local (U)LIRGs, for which relatively high linear resolution and signal-to-noise (S/N) ratio can be obtained.

**Methods.** We have obtained Very Large Telescope VIMOS optical integral field spectroscopy (IFS) for 38 local ( $z < 0.1$ ) (U)LIRGs (31 LIRGs and 7 ULIRGs, 51 individual galaxies). This sample covers well the less studied LIRG luminosity range, and it includes the morphological types corresponding to the different phases along the merging process (i.e., isolated disks, interacting and merging systems).

**Results.** The vast majority of objects have two main kinematically distinct components. One component (i.e., *narrow* or *systemic*) extends over the whole line-emitting region and is characterized by small-to-intermediate velocity dispersions (i.e.,  $\sigma$  from 30 to 160 km s<sup>-1</sup>). The second component (*broad*) has a larger velocity dispersion (up to 320 km s<sup>-1</sup>); it is mainly found in the inner regions and is generally blueshifted with respect to the systemic component. The largest extensions and extreme kinematic properties are observed in interacting and merging systems, and they are likely associated with nuclear outflows. The systemic component traces the overall velocity field, showing a large variety of kinematic 2D structures, from very regular velocity patterns typical of pure rotating disks (29%) to kinematically perturbed disks (47%) and highly disrupted and complex velocity fields (24%). Thus, most of the objects (76%) are dominated by rotation. We find that rotation is more relevant in LIRGs than in ULIRGs. There is a clear correlation between the different phases of the merging process and the mean kinematic properties inferred from the velocity maps. In particular, isolated disks, interacting galaxies, and merging systems define a sequence of increasing mean velocity dispersion and decreasing velocity field amplitude, characterized by average dynamical ratios ( $v_{\text{shear}}^*/\sigma_{\text{mean}}$ ) of 4.7, 3.0 and 1.8, respectively. We also find that the  $\sigma_{\text{central}}/\sigma_{\text{mean}}$  vs.  $\sigma_{\text{mean}}$  plane is an excellent discriminating plane between disks and interacting/merging systems: disks show a mean ratio a factor of 2 larger than those characterizing the other two classes. The LIRGs classified as isolated disks have similar velocity amplitudes but larger mean velocity dispersions (44 vs. 24 km s<sup>-1</sup>) than local spirals, implying a larger turbulence and thicker disks. Interacting systems and mergers have values closer to those of low velocity dispersion elliptical/lenticular galaxies (E/SOs). The subclass of (U)LIRGs classified as mergers have kinematical properties similar to those shown by the Lyman break analogs (LBAs), although the dynamical mass of LBAs is five times lower on average. Therefore, despite the difference in mass and dust content, the kinematics of these two local populations appears to have significantly noncircular motions. These motions may be induced by the tidal forces, producing dynamically hot systems. The dynamical masses range from  $\sim 0.04 m_{\star}$  to  $1.4 m_{\star}$  (i.e.,  $m_{\star} = 1.4 \times 10^{11} M_{\odot}$ ), with ULIRGs being more massive (i.e.,  $\sim 0.5 \pm 0.2 m_{\star}$ ) than LIRGs by, on average, a factor of about 2. The mass ratio of individual pre-coalescence galaxies is  $< 2.5$  for most of the systems, confirming that most (U)LIRG mergers involve sub- $m_{\star}$  galaxies of similar mass.

**Key words.** Galaxy: evolution – Galaxy: kinematics and dynamics

## 1. Introduction

Luminous and ultraluminous infrared galaxies (LIRGs,  $L_{\text{IR}} = [8-1000 \mu\text{m}] = 10^{11}-10^{12} L_{\odot}$ , and ULIRGs,  $L_{\text{IR}} > 10^{12} L_{\odot}$ , respectively) are important populations to study galaxy evolution. They are systems of intense star formation (SF), whose spectral energy distributions (SEDs) are dominated by dust thermal emission arising from the reprocessing of ultraviolet (UV) photons produced by young massive stars and/or active galactic nucleus (AGN) heating (e.g., U et al. 2012, and references therein). It has been proposed that ULIRGs are systems that transform

gas-rich disk galaxies into moderate-mass ellipticals through merger events (i.e., Genzel et al. 2001; Tacconi et al. 2002), with some, but not all, evolving to quasars (QSOs; Colina et al. 2001; Sanders et al. 2003). These objects exhibit a large variety of morphologies, which suggest different dynamical phases: from mostly isolated disks for low-luminosity LIRGs to a majority of merger remnants for ULIRGs (e.g., Veilleux et al. 2002; Arribas et al. 2004). Although (U)LIRGs are rare in the local universe (e.g., Lagache et al. 2005), they are much more numerous at high- $z$  and are relevant contributors to the whole past star formation beyond  $z \sim 1$  (e.g., Le Floch et al. 2005; Pérez-González et al. 2005, 2008). Therefore, low- $z$  (U)LIRGs offer a unique opportunity to study, at high linear resolution and signal-to-noise

<sup>\*</sup> Appendices are available in electronic form at <http://www.aanda.org>

ratio (S/N), extreme SF events and compare them with those observed at high- $z$ .

The 2D kinematic characterization of galaxies is a key element to study the physical processes that govern their formation and evolution. For instance, it provides a powerful diagnostic i) to infer the main source of dynamical support (e.g., Puech et al. 2007; Epinat et al. 2009); ii) to distinguish between relaxed virialized systems and merger events (e.g., Flores et al. 2006; Shapiro et al. 2008; Bellocchi et al. 2012); iii) to detect and characterize radial motions associated with feedback mechanisms, like outflows (e.g., Shapiro et al. 2009; Rupke & Veilleux 2013); and iv) to infer fundamental galaxy quantities like dynamical masses (e.g., Colina et al. 2005) among other topics.

Despite their relevance, the number of spatially resolved kinematic studies of low- $z$  (U)LIRGs is rather limited. Most optical and near-IR integral field spectroscopy (IFS) analysis has been focused on individual objects (e.g., Colina et al. 1999; Tecza et al. 2000; Arribas et al. 2001; García-Marín et al. 2006; Bedregal et al. 2009; Piqueras López et al. 2012) or small samples (e.g., Monreal-Ibero et al. 2006), generally at the highest luminosity (i.e., ULIRGs). Colina et al. 2005 discussed IFS-based  $H\alpha$  velocity maps for 11 ULIRGs, finding that in general their kinematics do not correspond to that of an ordered rotating system but are dominated by motions associated with tidal forces. Recently Westmoquette et al. (2012) have expanded this census by presenting optical ( $H\alpha$ ) IFS of 18 ULIRGs observed with VIMOS at the Very Large Telescope (VLT), finding a larger fraction of objects dominated by rotation.

In this paper we significantly expand previous samples (in number and characteristics) by obtaining spatially resolved kinematics of 38 local (U)LIRG systems (51 individual galaxies) observed with the VIMOS/VLT integral field unit (IFU). The sample contains a large fraction (i.e., 31/38) of sources in the less studied LIRG luminosity range. This is relevant for two main reasons. On the one hand, it complements previous studies focused on ULIRGs, filling the gap between the extreme cases and the general population of local star-forming galaxies (SFGs). On the other hand, several authors have suggested that high- $z$  LIRGs are scaled-up versions of low- $z$  LIRGs (e.g., Pope et al. 2006; Papovich et al. 2007; Elbaz et al. 2010, 2011; Nordon et al. 2010, 2012; Takagi et al. 2010).

The main goals of the present paper are i) to present the atlas of ionized gas velocity fields and velocity dispersion maps for this sample of (U)LIRGs; ii) to characterize their main 2D kinematic properties; and iii) to compare such properties with those of other relevant low- $z$  samples. More focused studies, including a detailed comparison with high- $z$  samples, will be presented in future papers.

This is part of a series of papers belonging to a large project aiming at characterizing the properties of (U)LIRGs on the basis of optical and infrared IFS. In particular, the first results of the VIMOS survey were presented in Arribas et al. (2008, hereafter, Paper I), along with a detailed kinematic study of two galaxies representative, respectively, of interacting pairs (i.e., IRAS F06076-2139) and morphologically regular spirals (i.e., IRAS F12115-4656). Monreal-Ibero et al. (2010, hereafter, Paper II) studied the nature and origin of the ionization mechanisms operating in the extra-nuclear regions of LIRGs as a function of the interaction phase and infrared luminosity. The morphologies of the stellar continuum and the ionized gas ( $H\alpha$ ) emissions have been analyzed in Rodríguez-Zaurín et al. (2011, hereafter, Paper III). In Arribas et al. (2012), the analogy between local LIRGs and ULIRGs, observed with

INTEGRAL/WHT and VIMOS/VLT and high- $z$  massive SFGs is studied by comparing their basic  $H\alpha$  structural characteristics.

The paper is structured as follows. In Sect. 2, we present the sample as well as some details about the observations, data reductions, line fitting and map construction. Section 3 is focused both on the 2D kinematic properties derived from the velocity maps and the global properties for the main kinematically distinct components found. Section 4 discusses how the kinematic properties of (U)LIRGs depend on infrared luminosity and on the different dynamical phases along the merging process. This section is also devoted to deriving and discussing the dynamical masses of (U)LIRGs, which, together with the main kinematic properties, are compared with other local samples. Finally, the main results and conclusions are summarized in Sect. 5. In the Appendix, the kinematic maps, comments on the individual objects, and details on the method followed to derive the effective radii are presented. Throughout the paper we will consider  $H_0 = 70 \text{ km s}^{-1} \text{ Mpc}^{-1}$ ,  $\Omega_M = 0.3$  and  $\Omega_\Lambda = 0.7$ .

## 2. Observations, data reduction, data analysis

### 2.1. The sample

The sample analyzed here contains a total of 38 (U)LIRGs systems (51 individual galaxies) of the southern hemisphere drawn from the Revised Bright Galaxy Sample (RBGS, Sanders et al. 2003). Of these systems 31 are LIRGs (i.e.,  $\langle L_{\text{IR}} \rangle = 2.9 \times 10^{11} L_\odot$ ) with a mean redshift of 0.024 (corresponding to  $D \sim 100 \text{ Mpc}$ ), and the remaining seven are ULIRGs (i.e.,  $\langle L_{\text{IR}} \rangle = 1.6 \times 10^{12} L_\odot$ ) with a mean redshift of 0.069 ( $D \sim 300 \text{ Mpc}$ ; see Table 1 and Paper I for details). Therefore, this sample includes a good representation of the relatively less studied LIRG luminosity range. It encompasses a wide variety of morphological types, suggesting different dynamical phases (isolated spirals, interacting galaxies, and ongoing- and post-mergers), and nuclear excitations (HII, Seyfert, and LINER). Some objects have evidence in their optical spectra of hosting an AGN, showing high [NII]/ $H\alpha$  values and/or broad  $H\alpha$  emission lines (e.g., IRAS F05189-2524, IRAS F21453-3511; Monreal-Ibero et al. 2010, Arribas et al. 2012). The sample is complete neither in luminosity nor in distance. However, it covers well the relevant luminosity range and is representative of the different morphologies within the (U)LIRG phenomenon.

The morphology class was derived using ground-based images (i.e., Digital Sky Survey (DSS) and additional archival Hubble Space Telescope (HST) images when available). The sources have been morphologically classified following a simplified version of the scheme proposed by Veilleux et al. (2002), with three main classes instead of five (see Rodríguez-Zaurín et al. 2011 for further details). Briefly, the three morphological classes are defined as follows:

- Class 0: objects that appear to be single isolated galaxies, with a relatively symmetric disk morphology and without evidence for strong past or ongoing interaction (hereafter *disk*).
- Class 1: objects in a pre-coalescence phase with two well-differentiated nuclei separated a projected distance  $> 1.5 \text{ kpc}$ . For these objects, it is still possible to identify the individual merging galaxies and their corresponding tidal structures due to the interaction (hereafter *interacting*).
- Class 2: objects with two nuclei separated a projected distance  $\leq 1.5 \text{ kpc}$  or a single nucleus with a relatively asymmetric morphology suggesting a post-coalescence merging phase (hereafter *merger*).

**Table 1.** General properties of the (U)LIRGs sample.

ID1 IRAS (1)	ID2 Other (2)	$z$ (3)	$D$ (Mpc) (4)	Scale (pc'') (5)	$\log L_{\text{IR}}$ ( $L_{\odot}$ ) (6)	Class (7)	Notes (8)
F01159-4443	ESO 244-G012	0.022903	99.8	462	11.48 (N)	1	a, d
F01341-3735	ESO 297-G011/G012	0.017305	75.1	352	11.18 (G11:10.99; G12:10.72)	1	a, d
F04315-0840	NGC 1614	0.015983	69.1	325	11.69	2	
F05189-2524		0.042563	188.2	839	12.19	2	
F06035-7102		0.079465	360.7	1501	12.26	1	
F06076-2139		0.037446	165	743	11.67 (N)	1	a, d
F06206-6315		0.092441	423.3	1720	12.27	1	
F06259-4780	ESO 255-IG007	0.038790	171.1	769	11.91 (N)	1	b,d
F06295-1735	ESO 557-G002	0.021298	92.7	431	11.27	0	
F06592-6313		0.022956	100	464	11.22	0	
F07027-6011	AM 0702-601	0.031322	137.4	626	11.64 (S:11.51; N:11.04)	0	a, d
F07160-6215	NGC 2369	0.010807	46.7	221	11.16	0	
08355-4944		0.025898	113.1	521	11.60	2	
08424-3130	ESO 432-IG006	0.016165	70.1	329	11.04 (S)	1	a, d
F08520-6850	ESO 60-IG016	0.046315	205.4	909	11.83	1	
09022-3615		0.059641	267	1153	12.32	2	
F09437+0317	IC-563 / 564	0.020467	89	415	11.21(S:10.82; N:10.99)	1 (0)	a, c, d
F10015-0614	NGC 3110	0.016858	73.1	343	11.31	0	
F10038-3338	ESO 374-IG032	0.034100	149.9	679	11.77	2	
F10257-4339	NGC 3256	0.009354	40.4	192	11.69	2	
F10409-4556	ESO 264-G036	0.021011	91.4	425	11.26	0	
F10567-4310	ESO 264-G057	0.017199	74.6	350	11.07	0	
F11255-4120	ESO 319-G022	0.016351	70.9	333	11.04	0	
F11506-3851	ESO 320-G030	0.010781	46.6	221	11.30	0	
F12043-3140	ESO 440-IG058	0.023203	101.1	468	11.37 (S)	1	a, d
F12115-4656	ESO 267-G030	0.018489	80.3	375	11.11	0	
12116-5615		0.027102	118.5	545	11.61	2 (0)	
F12596-1529	MCG-02-33-098	0.015921	69.0	324	11.07	1	
F13001-2339	ESO 507-G070	0.021702	94.5	439	11.48	2 (0/1)	
F13229-2934	NGC 5135	0.013693	59.3	280	11.29	0	
F14544-4255	IC 4518	0.015728	68.2	320	11.11(E:10.80; W:10.80)	1	a, d
F17138-1017		0.017335	75.2	352	11.41	2 (0)	
F18093-5744	IC 4687/4686/4689	0.017345	75.3	353	11.57 (N:11.47; C:10.87)	1	b, d
F21130-4446		0.092554	423.9	1722	12.09	2	
F21453-3511	NGC 7130	0.016151	70.0	329	11.41	2	
F22132-3705	IC 5179	0.011415	49.3	234	11.22	0	
F22491-1808		0.077760	352.5	1471	12.17	1	
F23128-5919	AM 2312-591	0.044601	197.5	878	12.06	1	

**Notes.** Column (1): object designation in the Infrared Astronomical Satellite (IRAS) Faint Source Catalog (FSC). Column (2): other identification. Column (3): redshift from the NASA Extragalactic Database (NED). Column (4): luminosity distance assuming a  $\Lambda$ CDM cosmology with  $H_0 = 70 \text{ km s}^{-1} \text{ Mpc}^{-1}$ ,  $\Omega_M = 0.3$ , and  $\Omega_\Lambda = 0.7$ , using the E. L. Wright Cosmology calculator, which is based on the prescription given by Wright (2006). Column (5): scale. Column (6): infrared luminosity ( $L_{\text{IR}} = L(8-1000) \mu\text{m}$ ) in units of solar bolometric luminosity, calculated using the fluxes in the four IRAS bands as given in Sanders et al. (2003) when available. Otherwise, the standard prescription given in Sanders & Mirabel (1996) with the values in the IRAS Point and Faint Source catalogs was used. Column (7): morphological class defined as follows: 0 identifies *isolated* objects, 1 *pre-coalescence* systems, and 2 stands for *merger* objects. For those objects for which the morphological classification is uncertain, the various possible classes are shown in the table with the preferred morphological classification indicated in the first place and the alternative classification within brackets (see text for further details). Column (8): notes with the following code: (a) system composed of two galaxies. (b) System composed of three galaxies. (c) There are two VIMOS pointings for the northern source. (d) Interacting system (i.e., see notes *a* and *b*) for which the total infrared luminosity  $L_{\text{IR}}$  could be approximately assigned among the members of the system according to the *Spitzer*/MIPS photometry\*. (The estimations for the individual sources are shown in parentheses in Col. (6)). When the whole infrared luminosity contribution is assigned only to one of the sources of the system, either *Spitzer* data at  $24 \mu\text{m}$  are not available or the limited angular resolution does not allow the different galaxies to be separated. Each source is identified according to its position in the VIMOS FoV according to N, S, C, E, and W which stand for the northern, southern, central, eastern, and western object, respectively. \**Spitzer*/MIPS data are available at the NASA/IPAC Infrared Science Archive (<http://irsa.ipac.caltech.edu>).

In Table 1 we present the main properties of the sample. In some cases the properties of individual galaxies in multiple systems could be inferred separately and were therefore treated individually. As part of the analysis, additional galaxies with available IFS data have been included to increase the number of systems in the ULIRG luminosity range. These data (Colina et al. 2005; García-Marín et al. 2007, 2009) correspond to our own observations taken with INTEGRAL/WHT.

## 2.2. Observations

The observations have been described in detail in previous papers (e.g., Monreal-Ibero et al. 2010). In brief, they were carried out using the IFU of VIMOS (Le Fèvre et al. 2003) at the VLT, covering the spectral range (5250–7400) Å with the high-resolution grating GG435 (“HR-orange” mode) and a mean spectral resolution of 3470 (dispersion of  $0.62 \text{ Å pix}^{-1}$ ). The



field of view (FoV) in this configuration is  $27'' \times 27''$ , with a spaxel scale of  $0.67''$  per fiber (i.e., 1600 spectra are obtained simultaneously from a  $40 \times 40$  fiber array). A square 4 pointing dithering pattern was used. With a relative offset of  $2.7''$  (i.e., 4 spaxels), this pattern provides an effective FoV of  $29.5'' \times 29.5''$ . The exposure time per pointing ranges from 720 to 850 s, so that, the total integration time per galaxy is between 2880 and 3400 s.

### 2.3. Data reduction

The VIMOS data were reduced with a combination of the pipeline *Esoresx* (versions 3.5.1 and 3.6.5) which is included in the pipeline provided by ESO, and different customized IDL and IRAF scripts. The basic data reduction (i.e., bias subtraction, flat field correction, spectra tracing and extraction, correction of fiber and pixel transmission, and relative flux calibrations) is performed using the *Esoresx* pipeline. The four quadrants per pointing are reduced individually and then combined into a single data cube. After that, the four independent dithered pointing positions are combined to end up with the final “supercube”, containing  $44 \times 44$  spaxels for each object (i.e., 1936 spectra).

To estimate the absolute wavelength calibration accuracy and the spectral resolution (i.e., instrumental profile), we first fitted the [O I] $\lambda 6300.3$  Å sky line to a single Gaussian for all spectra of each individual source, obtaining the mean central wavelength and FWHM for each object. Since we are going to concentrate on a wavelength range around the H $\alpha$  and the [N II] $\lambda 6548.1$ , 6583.4 Å emission lines, the [O I] $\lambda 6300.3$  Å sky line is suitable due to its proximity to these lines. The mean values for the central wavelength and FWHM for the whole sample were  $(6300.29 \pm 0.07)$  Å and  $(1.80 \pm 0.07)$  Å, respectively, which also gives a good estimate of the uncertainties due to calibration. The wavelength calibration, the instrumental profile, and fiber-to-fiber transmission correction are checked for all the galaxies using the aforementioned sky line. A more detailed description of the data reduction process is given in Papers I and III.

### 2.4. Line fitting and map generation

The observed H $\alpha$  and [NII] $\lambda 6548$ , 6583 Å emission lines of the individual spectra are fitted to Gaussian profiles using an IDL routine (i.e., MPFITEXPR, implemented by Markwardt). This algorithm derives the best set of lines that match the available data. In case of adjusting multiple lines, the line flux ratios and wavelengths of the different lines are fixed according to the atomic physics. The widths are constrained to be equal for all the lines and greater than the instrumental contribution ( $\sigma_{\text{INS}}$ ).

We select spaxels where H $\alpha$  lines are detected with  $S/N > 4$ , fitting automatically all the lines to single Gaussian profiles (i.e., 1 component (1c) fit), which gave good results for the majority of the spectra. However, for certain regions of the galaxies, a multi-component fit (i.e., 2 components (2c) per line) was added when clearly required in order to adequately fit the data. In these cases, we can identify systemic (or *narrow*) and secondary (or *broad*) components, according to their widths. This approach tends to underestimate the role of the second component (i.e., flux and extension) when compared with other methods which assume the existence of two (or more) components. These components usually have different central velocities, confirming that they are two kinematically distinct components. The lines associated with different components were fitted simultaneously, maintaining for each component the assumptions mentioned before. The

narrow component usually extends over the whole galaxy line-emitting region, while the broad component covers a smaller area corresponding to the nuclear regions of the galaxies.

We check all the spectra by visual inspection. Looking at the H $\alpha$  line profile and the residuals of the fit, we decided to apply 1c or 2c fitting. Where the presence of one or two components was dubious the percentage of spectra was generally small (i.e., typically a few percent) since it was clear that one or two components were preferred for a large majority. There are a few cases where decomposition introduces some uncertainties, and these are commented on Appendix A. Two components are considered when the 2c fits give a significantly lower  $\chi^2$  value than that derived when using 1c fits (i.e.,  $\chi^2_{2c} / \chi^2_{1c} < 0.5$ ). A couple of examples showing two different kinds of fittings, 1c and 2c, are shown in Fig. 1. Only a few systems do not show clear signs of broad components (e.g., IRAS F06259-4780 S, IRAS F09437+0317 S, IRAS F12043-3140 N, and IRAS F22132-3705).

For each emission line/component, we end up with the following information: line flux, central wavelength ( $\lambda_c$ ), and intrinsic width ( $\sigma_{\text{line}} = \sqrt{\sigma_{\text{obs}}^2 - \sigma_{\text{INS}}^2}$ )<sup>1</sup>, together with their corresponding fitting errors. However, a better estimate of the actual uncertainties associated with the kinematic parameters is obtained by combining in quadrature fitting and calibration errors (see Sect. 2.3). For high S/N spectra fitting errors are small (typically,  $\Delta\lambda < 0.1$  Å;  $\Delta\sigma < 0.1$  Å) and calibration errors can be considered the main source of uncertainty (and vice versa for spectra with  $S/N < 5$ ).

Flux intensity, velocity field, and velocity dispersion maps for the narrow and broad components (see Appendix A) are obtained using IDL procedures (i.e., jmaplot, Maíz-Apellániz 2004). As reference, we also include the continuum image generated from the VIMOS-IFU data cube. When HST imaging is available, it is also shown.

We note that due to the different resolving power of the original spectra, authors use a different number of line components to fit the observed profiles. For instance, Colina et al. (2005) consider only one component for most of their sample due to the relatively low spectral resolution of their INTEGRAL/WHT data (i.e.,  $R = 1500$ ), while Westmoquette et al. (2012) use two or three components (see Sect. 3.1.3 for details) thanks to the higher spectral resolution of the VIMOS/VLT data (i.e.,  $R = 3100$ ). When considering only one component,  $v$  and  $\sigma$  are in general similar to those of the narrow component in a 2-Gaussian fit. We have used our sample to quantify the effects on the kinematic quantities (i.e.,  $v_{\text{shear}}$ ,  $\sigma_{\text{mean}}$  (see Sect. 3.1.1) and  $\sigma_c$  (see Sect. 4.2)). We find that the central velocity dispersion,  $\sigma_c$ , increases on average by  $\sim 20\%$  if one (instead of two) component fitting is applied to about dozen cases (e.g., IRAS F09022-3615, IRAS F01341-3735 G11, IRAS F06035-7102, IRAS F07160-6215, IRAS F08355-4944, IRAS F14544-4255 W, IRAS F22491-1808) that are potentially affected by the selected approach. On the other hand, the mean velocity dispersion,  $\sigma_{\text{mean}}$ , only increases by a few percent (up to 10% in the case of IRAS F08355-4944). The velocity shear,  $v_{\text{shear}}$ , is virtually unaltered by the fitting approach. Therefore, we note that the  $\sigma_{\text{mean}}$  and  $v_{\text{shear}}$  values, on which most of the analysis is based on, are not significantly affected by the fit approach considered. Although there is evidence in a few cases for the presence of more than two components in our spectra, these were faint and/or with a very complex structure.

<sup>1</sup> An average value of the  $\sigma_{\text{INS}}$  of  $(37 \pm 2)$  km s<sup>-1</sup> is used (see Sect. 2.3).

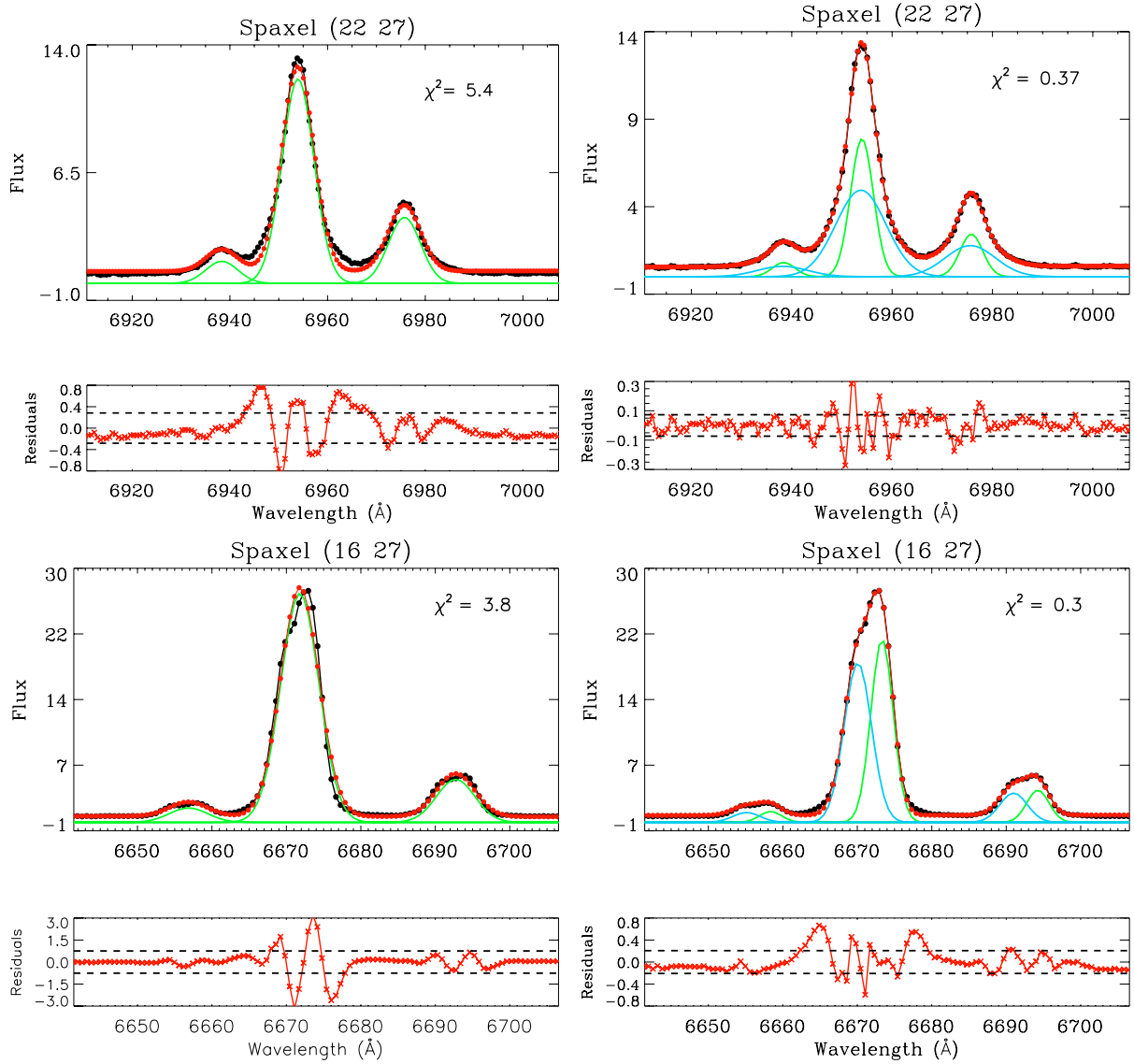


**Fig. 1.** Examples of one (1c, on the left) and two (2c, on the right) component Gaussian fits to the  $H\alpha$  + [NII] profiles in two different spaxels in IRAS F09022-3615 (top) and IRAS F18093-5744 C (bottom). The  $\chi^2$  for all the Gaussian fittings is shown for a direct comparison. The systemic (narrow) component is shown in green, while the broad one is shown in light blue. The red curve shows the total contribution coming from the  $H\alpha$  + [NII] Gaussian fit. Below, the residuals (i.e., data – model) are presented: they clearly show when two components are needed to properly fit asymmetric line profiles. The standard deviation value of the residuals (i.e.,  $\pm 1\sigma$ ) is shown using dashed lines.

### 3. Results

#### 3.1. Spatially resolved kinematics in (U)LIRGs: components properties

Figures in Appendix A show the  $H\alpha$  flux, velocity field, and velocity dispersion maps of the different kinematic components for each galaxy of the present sample. The characteristics of the velocity fields and velocity dispersion maps are discussed individually in that Appendix.

##### 3.1.1. Narrow (systemic) component

The narrow component covers the whole  $H\alpha$  line-emitting region of these galaxies and generally contains most of the  $H\alpha$  flux. Therefore, it is morphologically similar to the total flux (i.e., narrow + broad)  $H\alpha$  maps presented by Rodríguez-Zaurín et al. (2011). The spatial extension of this component (10–350 kpc<sup>2</sup>; see Table 4) is similar to that of the continuum emission, though in some cases there are significant structural differences (e.g., F01341-3735 (S, N); see also

Rodríguez-Zaurín et al. 2011). Its spatial distribution and kinematic properties represent those of the entire galaxy, and it is therefore identified as the systemic component.

This narrow (systemic) component shows a large variety of 2D kinematic properties. The kinematic maps of some sources show very regular patterns, with a spider-like velocity field and a centrally peaked velocity dispersion distribution, as expected for pure rotating disk (e.g., IRAS F11506-3851, IRAS F12115-4656). However, most of the objects have some kind of irregularities and distortions in their velocity maps, despite a large rotation component in many cases. These departures from a regular rotation pattern include: i) kinematic axes that are poorly defined (e.g., IRAS F13229-2934), nonperpendicular each to another (e.g., IRAS F11255-4120), and/or shifted with respect to the photometric axes (e.g., IRAS F10038-3338); ii) asymmetry between the approaching and receding regions (e.g., IRAS F13229-2934); and iii) off-nuclear kinematic center (e.g., IRAS F12596-1529). In addition, the velocity dispersion maps generally show an asymmetric structure. Although the highest

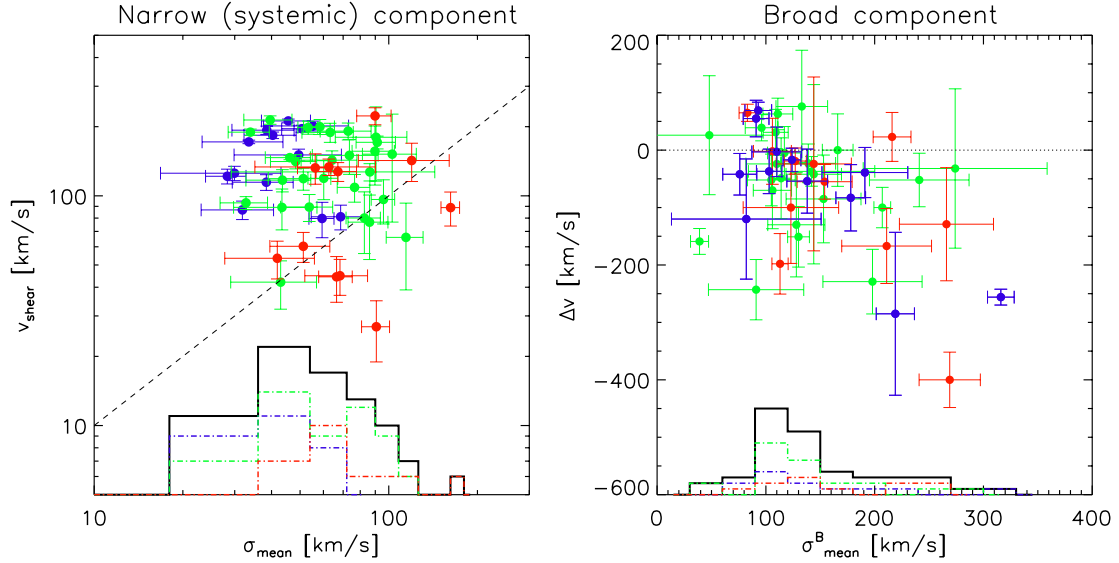


**Fig. 2.** *Left panel:* velocity shear,  $v_{\text{shear}}$ , versus the mean velocity dispersion,  $\sigma_{\text{mean}}$ , for the narrow (systemic) component. Blue, green, and red dots distinguish, respectively, morphological classes 0 (isolated disks), 1 (interacting), and 2 (mergers). The distribution of  $\sigma_{\text{mean}}$  values is also shown, with the contribution of the different morphological classes. The 1:1 dot line is shown as reference to highlight the fact that most of the sources have  $v_{\text{shear}} > \sigma_{\text{mean}}$ . *Right panel:* velocity shift,  $\Delta v$ , between the broad and narrow components versus the mean velocity dispersion of the broad component,  $\sigma_{\text{mean}}^{\text{B}}$ . The horizontal dot line indicates the zero velocity shift. Most of the objects have a blueshifted broad component.

velocity dispersion is usually coincident with the optical nucleus and therefore seems to trace the mass, there are cases where the absolute peak is associated with (tidal) structures located at large galactocentric distances (e.g., in IRAS F04315-0840 at 3.6 kpc; in IRAS F10015-0614 at 4 kpc; in F12043-3140 S at 3.4 kpc). Interestingly, a significant number of systems have ring-like structures of high velocity dispersion (i.e.,  $\sigma \sim 150\text{--}200 \text{ km s}^{-1}$ ) in their outer regions (e.g., IRAS F07027-6011S, IRAS 09022-3615, IRAS F12116-5615). These are regions of relatively low H $\alpha$  emission, which are likely ionized by shocks (Monreal-Ibero et al. 2010 and references therein).

We have used our IFS-based velocity maps to infer some global kinematic properties associated with this component (see Table 4). Figure 2 shows the observed (i.e., uncorrected for inclination) velocity shear,  $v_{\text{shear}}$ <sup>2</sup>, and the spatially resolved uniformly weighted mean velocity dispersion,  $\sigma_{\text{mean}}$ , of the narrow (systemic) component over the whole line-emitting region. These two properties have a relatively large range of values ( $30 < v_{\text{shear}} < 220 \text{ km s}^{-1}$ ;  $30 < \sigma_{\text{mean}} < 160 \text{ km s}^{-1}$ ). However, the scatter in the figure is dominated not by errors associated with the observations and/or the analysis but by errors associated with different intrinsic properties among the objects. This reflects that the selected (U)LIRGs represent a kinematically diverse sample. In fact, the figure shows a clear dependence on the mean  $v_{\text{shear}}$  and  $\sigma_{\text{mean}}$  values with the morphological class, with isolated disks having relatively lower values than systems in a more evolved dynamical phase (interacting and merging systems; see Table 4). In Sect. 4, we discuss in more detail the mean kinematic properties of (U)LIRGs as a function of their morphology/dynamical status.

### 3.1.2. Broad component

The broad component is generally restricted to the central regions, though in some cases it is found at very large galactocentric distances (up to  $\sim 7$  kpc in IRAS F23128-5919). Although

in most of the cases, the (projected) area covered by the broad component is smaller than  $3 \text{ kpc}^2$ , there is a significant fraction (12/46) of objects with an extension larger than  $5 \text{ kpc}^2$  (see Table 5). In a few cases, the broad component can be dominant in terms of flux in the innermost spaxels (e.g., IRAS F05189-2524, IRAS F08355-4944). In some cases the broad emission is offset with respect to the photometric nucleus, thus defining an asymmetric structure (e.g., IRAS F12043-3140 S, IRAS F18093-5744 N). At some locations the broad component can be due to the line-of-sight overlapping of two physically distinct structures (e.g., IRAS F06076-2139, where the emission from the northern galaxy overlaps with the ring of the southern source; see also Paper I).

Due to sampling limitations, compactness, and low-surface brightness constraints, the detailed study of the 2D kinematic structure of this component is sometimes difficult. However, in several sources it is clearly resolved, and the kinematic axes can be well defined. For instance, in IRAS F04315-0840 (NGC 1614) the kinematic axes associated with the broad component are nearly perpendicular to those of the narrow component, which is a clear feature of outflows perpendicular to the disk (Heckman et al. 1990; Bellocchi et al. 2012). The velocity dispersion maps of several objects do not have a radial symmetry and/or have an off-nuclear kinematic center of symmetry (e.g., IRAS F04315-0840, IRAS F06035-7102, IRAS F07160-6215, IRAS F10038-3338).

The range of the global kinematic properties of the broad component (right panel of Fig. 2) in velocity dispersions is significantly larger than that of the narrow component, with values of up to  $\sim 320 \text{ km s}^{-1}$  (i.e.,  $FWHM \sim 750 \text{ km s}^{-1}$  for IRAS F07027-6011N). However, a large fraction of sources (i.e., 26/46) are in the range  $90 < \sigma_{\text{mean}}^{\text{B}} < 150 \text{ km s}^{-1}$  (see Table 5). The mean central velocity of the broad component is blueshifted with respect to that of the narrow component for a majority of sources, reaching values up to  $\Delta v = -400 \text{ km s}^{-1}$  (i.e., IRAS F05189-2524). There is however, a significant fraction of objects (9/46) with redshifted velocities, which seem to cluster around velocity dispersion values of  $\sim 100 \text{ km s}^{-1}$ .

<sup>2</sup>  $v_{\text{shear}}$  is defined as half of the difference between the median value of the 5 percentile at each end of the velocity distribution (i.e.,  $v_{\text{shear}} = \frac{1}{2}(v_{\text{max}}^{5\%} - v_{\text{min}}^{5\%})$ ), following previous works (e.g., Gonçalves et al. 2010).



**Table 2.** Mean (and median) kinematic properties for the different (U)LIRG samples.

Sample	$\langle \log L_{\text{IR}} \rangle$ ( $L_{\odot}$ )	$SFR$ ( $M_{\odot} \text{ yr}^{-1}$ )	$v_{\text{shear}}$ ( $\text{km s}^{-1}$ )	$v_{\text{shear}}^*$ ( $\text{km s}^{-1}$ )	$\sigma_{\text{mean}}$ ( $\text{km s}^{-1}$ )	$v_{\text{shear}}^*/\sigma_{\text{mean}}$	$R_{\text{eff}}^{\text{IR}}$ (kpc)	$M_{\text{dyn}}^{\text{IR}}$ ( $10^{10} M_{\odot}$ )	$K$ class* (RD; PD; CK)/T
(1)	(2)	(3)	(4)	(5)	(6)	(7)	(8)	(9)	(10)
ALL	$11.4 \pm 0.4$	$88 \pm 15$ (45)	$130 \pm 7$ (128)	$171 \pm 9$ (177)	$63 \pm 4$ (58)	$3.2 \pm 0.3$ (2.6)	$2.5 \pm 0.2$ (2.4)	$4.9 \pm 0.6$ (3.5)	(14; 23; 12)/49
LIRG	$11.3 \pm 0.3$	$44 \pm 6$ (34)	$130 \pm 8$ (128)	$170 \pm 9$ (167)	$59 \pm 3$ (54)	$3.4 \pm 0.5$ (3.3)	$2.5 \pm 0.2$ (2.4)	$4.5 \pm 0.5$ (3.5)	(14; 22; 6)/42
ULIRG	$12.2 \pm 0.1$	$278 \pm 20$ (272)	$130 \pm 26$ (150)	$178 \pm 24$ (190)	$95 \pm 12$ (90)	$2.0 \pm 0.4$ (1.9)	$2.8 \pm 0.6$ (2.4)	$7.1 \pm 2.6$ (4.8)	(0; 1; 6)/7
(U)LIRG class 0	$11.3 \pm 0.3$	$48 \pm 18$ (32)	$150 \pm 14$ (171)	$195 \pm 17$ (182)	$44 \pm 4$ (46)	$4.7 \pm 0.5$ (4.3)	$2.7 \pm 0.3$ (3.0)	$5.1 \pm 1.0$ (4.9)	(6; 6; 1)/13
(U)LIRG class 1	$11.4 \pm 0.5$	$91 \pm 25$ (41)	$135 \pm 7$ (141)	$174 \pm 8$ (190)	$67 \pm 3$ (63)	$3.0 \pm 0.3$ (2.5)	$2.6 \pm 0.2$ (2.4)	$4.8 \pm 0.5$ (3.5)	(8; 12; 5)/25
(U)LIRG class 2	$11.7 \pm 0.3$	$129 \pm 32$ (86)	$98 \pm 18$ (89)	$134 \pm 21$ (157)	$80 \pm 11$ (67)	$1.8 \pm 0.3$ (1.5)	$2.6 \pm 0.5$ (2.0)	$4.7 \pm 1.9$ (1.7)	(0; 5; 6)/11
(U)LIRG RD	$11.4 \pm 0.3$	$65 \pm 25$ (35)	$159 \pm 12$ (180)	$207 \pm 16$ (207)	$50 \pm 5$ (46)	$4.7 \pm 0.5$ (5.4)	$2.7 \pm 0.4$ (2.5)	$5.8 \pm 1.0$ (5.1)	(14; 0; 0)/49
(U)LIRG PD	$11.3 \pm 0.4$	$56 \pm 15$ (36)	$123 \pm 10$ (119)	$160 \pm 13$ (163)	$58 \pm 4$ (53)	$3.1 \pm 0.3$ (3.1)	$2.4 \pm 0.2$ (2.3)	$4.1 \pm 0.6$ (3.5)	(0; 23; 0)/49
(U)LIRG CK	$11.7 \pm 0.5$	$161 \pm 36$ (202)	$112 \pm 15$ (127)	$155 \pm 17$ (157)	$91 \pm 8$ (90)	$1.7 \pm 0.2$ (1.7)	$2.7 \pm 0.5$ (2.3)	$5.9 \pm 1.8$ (3.4)	(0; 0; 12)/49

**Notes.** Column (1): sample: class 0 identifies isolated disks, class 1 denotes pre-coalescence interacting systems, and class 2 stands for mergers (see Sect. 2.1). RD stands for rotation dominated, PD perturbed disks and CK complex kinematic (see Sect. 4.1). Column (2): infrared luminosity. Column (3): star formation rate derived from the infrared luminosity listed in Col. 2 applying the Kennicutt (1998) relation. Column (4): observed velocity shear as defined in the text. Column (5): intrinsic velocity shear (i.e., inclination corrected). Column (6): mean velocity dispersion. Column (7): dynamical ratio between the intrinsic velocity shear and the mean velocity dispersion. Column (8): infrared effective radius, derived as explained in Appendix B. Column (9): dynamical mass derived as explained in the text. Column (10): number of galaxies classified as RD, PD, CK with respect to the total number of galaxies in the sub-sample. (\*) The total number of galaxies in the present sample is 51, but for the galaxy IRAS F08424-3130 N and IRAS F12596-1529 the kinematical classification was not possible as explained in the text. So, the number of galaxies with kinematical classification is 49.

The presence of AGNs may affect the kinematic properties of this component (e.g., L pari et al. 2003; Westmoquette et al. 2012; Rupke & Veilleux 2013; Arribas et al., in prep.). One of the two class 0 objects with large FWHM and  $\Delta v$  offset (i.e., IRAS F07027-6011 N) has evidence of hosting an AGN (see Rodr guez-Zaur n et al. 2011; Arribas et al. 2012). Excluding this object, most of the systems with  $\Delta v > 100 \text{ km s}^{-1}$  and/or  $\sigma_{\text{mean}}^{\text{B}} > 200 \text{ km s}^{-1}$  are class 1 and 2. Among these sources in an advance merging phase, several (i.e., IRAS F05189-2524, IRAS F06206-6315, IRAS F13229-2934, IRAS F14544-4255 W, IRAS F18093-5744 C, IRAS F21453-3511, and IRAS F23128-5919) also have evidence of hosting an AGN according to the optical spectroscopic classification (see Paper III) and/or the evidence for a broad H  line (see Arribas et al. 2012).

As for the spatial extension of the broad component, there is a clear trend with the morphological class. Specifically, the median areas covered by the broad component for classes 0, 1, and 2 are  $1.1 \text{ kpc}^2$ ,  $1.5 \text{ kpc}^2$ , and  $5.2 \text{ kpc}^2$ , respectively.

In summary, the present data show that an extended broad component is observed in most of LIRGs and ULIRGs. The mean velocity of most of the objects is blueshifted with respect to the narrow component, with values up to  $-400 \text{ km s}^{-1}$  and  $FWHM \sim 750 \text{ km s}^{-1}$ . The largest extensions and extreme kinematic properties ( $\Delta v$ , FWHM) are observed in interacting and merging systems (classes 1 and 2). The detailed study of the kinematic properties of the broad component will be done elsewhere (Arribas et al., in prep.).

### 3.1.3. Comparison with previous IFS studies

As mentioned above, the detailed comparison of the component properties with previous IFS studies is not straightforward. On the one hand, most of the previous studies are focused on the ULIRG luminosity range (e.g., Colina et al. 2005 and Westmoquette et al. 2012), while a large fraction of the present sources are LIRGs. On the other hand, there is some heterogeneity in the way in which the line fitting and component map construction are performed among the different works. In Colina et al. (2005) only one single component was in general adjusted to the observed profiles since the relatively low

spectral resolution of the INTEGRAL/WHT data does not allow the presence of multiple components in the lines to be reliably distinguished on a spaxel by spaxel basis. However, in general the derived kinematical values of  $v$  and  $\sigma$  in a 1-Gaussian fit are similar to those of the narrow component when applying a 2-Gaussian fit. In Westmoquette et al. (2012) multiple components were fitted for most of the sample thanks to the higher spectral resolution of the VIMOS/VLT data. The different components were assigned to the lines mainly using a line intensity criterion (rather than a line width criterion), regardless of the relative velocities of the components. Thus, they do not necessarily represent kinematically distinct components, as in our case. The morphological features seen in our kinematic maps are similar to those reported in these works, which also find asymmetries and departures from rotation for most of their objects. The range of  $\sigma$  found by Colina et al. (2005) (i.e.,  $50 < \sigma < 150 \text{ km s}^{-1}$ ) is similar to the one found here for the narrow component of the present sample. Westmoquette et al. (2012) also found it necessary to adjust multiple components over relatively extended regions. In addition, they discovered motions associated with outflows for a relatively large fraction of objects in their sample (11/18). However, as we discuss in the next section, we find a larger fraction of rotating systems than in their samples.

## 4. Discussion

### 4.1. Kinematical classification: the role of rotation in (U)LIRGs and its dependence on $L_{\text{IR}}$

The present sample is formed by a group of morphologically diverse objects, classified on the basis of optical imaging into three groups according to their suggested dynamical status (i.e., isolated relaxed rotating disks: class 0, interacting systems: class 1, and mergers: class 2; see Sect. 2 for more detailed definitions). In this section we perform a simple kinematic classification of the (U)LIRG sample based on the velocity fields and the velocity dispersion maps of the systemic component. This classification is similar to the one proposed by Flores et al. (2006) and distinguishes three main groups:

1. Rotating disks (RD): both the velocity field and the velocity dispersion maps show the expected pattern for rotation. The

major kinematic axis in the velocity field follows the major photometric axis of the continuum map, and the  $\sigma$ -map shows a peak near the galaxy nucleus. Regions of high velocity dispersions associated with the outer faint emission, such as those studied by Monreal-Ibero et al. (2010), are not considered a significant deviation from the global rotation pattern.

2. Perturbed disks (PD): the velocity field shows a general rotation pattern with well-defined approaching and receding regions, but the kinematic axes show some distortions and/or the  $\sigma$ -map has a peak shifted off the center;
3. Complex kinematics (CK): systems with both velocity field and velocity dispersion maps discrepant from the expected normal rotating disks showing the evidence of radial motions and/or disturbed velocity dispersion distribution.

From a total of 51 galaxies in the sample, 49 could be classified according to this scheme<sup>3</sup>. Of these, 14 are undoubtedly RD (29%), while for 23 additional ones rotation is likely to be dominant, despite the presence of clear asymmetries (PD, 47%). The remaining 12 show CK (24%). Therefore, for 76% of the galaxies (i.e., 37/49) rotation plays an important role.

As for the global properties, objects classified as RD, PD and CK have increasing values of  $\sigma_{\text{mean}}$  (i.e.,  $50 \pm 5$ ,  $58 \pm 4$ , and  $91 \pm 8$  km s<sup>-1</sup>, respectively) and decreasing  $v_{\text{shear}}$  ( $159 \pm 12$ ,  $123 \pm 10$ , and  $112 \pm 15$  km s<sup>-1</sup>, respectively), as shown in Table 2.

The fraction of rotating systems is considerably larger than those reported previously in ULIRGs by Colina et al. (2005) and Westmoquette et al. (2012). In particular, Colina et al. (2005) found while studying a sample of 11 ULIRGs that the velocity field of the ionized gas is dominated by tidally induced flows and generally does not correspond to rotationally supported systems. Only one system (i.e., IRAS 17208-0014, Arribas & Colina 2003) shows a dominant rotation pattern when fitting the emission lines to a single Gaussian component, and two more (i.e., Arp 220, see Arribas et al. 2001; Colina et al. 2004 and IRAS 08572+3915, see Arribas et al. 2000) could be considered as candidates for rotating systems after a kinematic decomposition similar to the one performed in the present paper. Westmoquette et al. (2012) find a larger fraction of rotating systems (i.e., 8/18) in their sample of ULIRGs. These fractions are significantly smaller than our finding of 37 out of 49 in the present (U)LIRG sample. This may be explained by the fact that the present work includes a large fraction of systems with lower luminosity (i.e., 31/38 LIRGs) than in the mentioned works, which only cover the ULIRG luminosity range.

In fact, we find that the kinematic class clearly correlates with the infrared luminosity  $L_{\text{IR}}$ . A large fraction (i.e., 6/7) of ULIRGs were classified as CK, while most of the objects with luminosity lower than  $10^{11.4} L_{\odot}$  are classified as PD or RD (i.e., PD = 11/21 and RD = 7/21, respectively). Therefore, large deviations from rotation are generally associated with ULIRGs, while the lower end of the luminosity range (i.e., LIRGs) is generally populated by rotation-dominated systems. However, exceptions to this rule exist: there is a ULIRG (i.e., IRAS F06206-6315) with a regular rotation pattern and there are a few LIRGs (e.g., IRAS F13001-2339, IRAS F13229-2934) showing complex kinematics.

It is also worth mentioning that a quantitative analysis of the relative importance of rotation with respect to the kinematic

asymmetries, based on the application of kinemetry methodology (Krajnović et al. 2006), has been presented in Bellocchi et al. (2012) for four sources. This methodology will be applied to the whole sample in a forthcoming work (Bellocchi et al. 2013). However, it is important to note that the kinemetry methodology by itself is not able to kinematically classify objects in terms of disk and interacting and merging systems. It requires some references to interpret the kinematic asymmetries associated with the different dynamical phases. Shapiro et al. (2008) and Bellocchi et al. (2012) propose different frontiers (i.e., total kinematic asymmetry) to distinguish disks from mergers, indicating that this topic deserves further investigation.

#### 4.2. Global kinematic properties along the merging process: $\sigma_c/\sigma_{\text{mean}}$ vs. $\sigma_{\text{mean}}$ a good discriminator between disks and interacting/merging systems

The kinematic classification described above shows that rotation is more frequent in systems classified as isolated (class 0) than in those classified as interacting (class 1) and mergers (class 2). The fraction of RD decreases from 46% to 32% for isolated and interacting systems, while none of the mergers are classified as RD. In contrast, only one isolated object presents CK, while the fraction of CK increases to 20% and 55% for interacting systems and mergers, respectively (see Table 2).

When the central (nuclear) velocity dispersion<sup>4</sup>,  $\sigma_c$ , of the systemic component is compared with its spatially resolved mean value,  $\sigma_{\text{mean}}$ , a clear segregation between isolated disks and interacting/merging systems is found (Fig. 3). Specifically, the derived mean  $\sigma_c/\sigma_{\text{mean}}$  ratios for disks, as well as for interacting and merging systems, are, respectively,  $(1.8 \pm 0.15)$ ,  $(1.1 \pm 0.05)$ , and  $(0.97 \pm 0.09)$ . On the one hand, this trend can be explained as a consequence of the tidal effects on the gas velocity dispersion. Isolated relaxed disks (class 0) have relatively low velocity dispersions outside the nuclear region, with a  $\sigma_{\text{mean}} \approx 44$  km s<sup>-1</sup> (i.e., a factor of  $\sim 2$  larger than that derived for local spiral galaxies, see Tables 2 and 3) and, generally, centrally peaked velocity dispersion maps, making the mentioned ratio relatively large. On the other hand, as in principle the beam smearing of the central velocity gradient in a disk might be significant to enhance the  $\sigma_c/\sigma_{\text{mean}}$  ratio (see Davies et al. 2011), the comparison of samples in this diagram should be done ideally at similar linear resolution. For our particular case, the effects on this ratio are expected to be small (i.e.,  $\sim 10\%$  in the most extreme case), as further discussed in Sect. 4.3.1. In the pre-coalescence (class 1) objects, the velocity dispersion outside the nucleus increases because the main body of the system is perturbed by tidal forces associated with interactions, reducing significantly such a ratio. The largest  $\sigma_{\text{mean}}$  values are reached for the ongoing, postcoalescence mergers (class 2). However, though  $\sigma_c$  and, to a lesser degree,  $\sigma_{\text{mean}}$  may (slightly) depend on the fitting approach (i.e., to one or two components), the general trend observed in the plot does not depend on the fitting approach<sup>5</sup>.

We note that this could be a good kinematic diagnostic diagram for classifying spatially resolved high- $z$  sources, though similar linear resolutions to the ones considered here should be used for a direct comparison. This is the case of several

<sup>3</sup> No kinematic classification has been possible for IRAS F08424-3130 N since it is located on the edge of the VIMOS FoV. For IRAS F12596-1529 the kinematic classification was not possible due to the limited linear resolution.

<sup>4</sup> The H $\alpha$  central velocity dispersion is derived as the mean value of the  $4 \times 4$  spaxels around the VIMOS continuum flux peak.

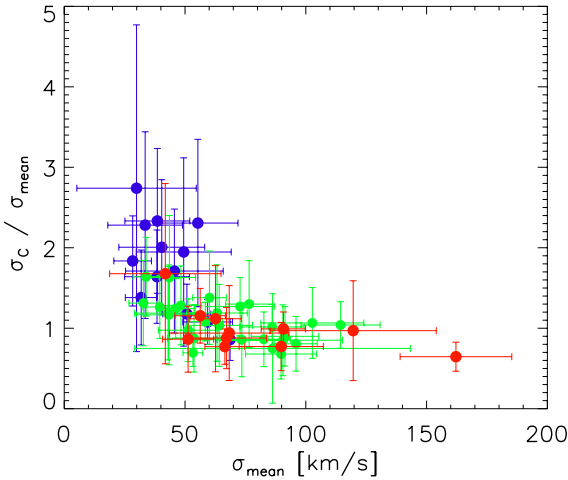
<sup>5</sup> We note that the narrow component of a 2-Gaussian fit has, in general, similar properties compared to those of a single Gaussian fitted line.



**Table 3.** Mean (and median) observed kinematic properties for low- $z$  comparison samples from the literature.

Sample	SFR [ $M_{\odot} \text{ yr}^{-1}$ ]	$v$ ( $\text{km s}^{-1}$ )	$\sigma$ ( $\text{km s}^{-1}$ )	$v/\sigma$	$R_{\text{eff}}$ (kpc)	$M_{\text{dyn}}$ ( $10^{10} M_{\odot}$ )
(1)	(2)	(3)	(4)	(5)	(6)	(7)
Spiral	$1.8 \pm 0.4$ (0.7)	$162 \pm 7$ (143)	$24 \pm 0.5$ (24)	$7.0 \pm 0.3$ (6.3)	$5.5 \pm 0.3$ (4.8)	$11.5 \pm 1.5$ (4.9)
E/S0	$0.12 \pm 0.04$ (0.08)	$47 \pm 4$ (44)	$162 \pm 9$ (163)	$0.34 \pm 0.03$ (0.34)	$2.9 \pm 0.3$ (2.4)	$13.8 \pm 3.2$ (6.9)
LBA	$26.7 \pm 7.1$ (17.0)	$67 \pm 11$ (63)	$71 \pm 6$ (67)	$0.95 \pm 0.11$ (1.1)	$1.4 \pm 0.1$ (1.5)	$1.0 \pm 0.2$ (1.0)

**Notes.** Column (1): low- $z$  sample: spiral sample is drawn from [Epinat et al. \(2010\)](#), E/S0 from [Cappellari et al. \(2007\)](#) and LBAs from [Gonçalves et al. \(2010\)](#). Column (2): star formation rate (SFR). For spirals, it has been derived using only 50 objects, for which the SFRs have been computed from  $H\alpha$  measurements by [James et al. \(2004\)](#) using Salpeter IMF ([Salpeter 1955](#)) and applying the [Kennicutt et al. \(1994\)](#) relation. For E/S0 galaxies we considered the SFR computed in [Shapiro et al. \(2010\)](#) for a subsample of 13 sources using the *Spitzer*/IRAC data at  $8.0 \mu\text{m}$ . They have calibrated this relation from the [Yun et al. \(2001\)](#) relation between SFR and radio continuum. If the [Kennicutt \(1998\)](#) SFR- $H\alpha$  conversion is applied to calibrate the  $8.0 \mu\text{m}$  SFR estimator, the SFR would lower by  $\sim 13\%$  (see [Wu et al. 2005](#)). For the LBAs, the star formation rates are measured by [Gonçalves et al. \(2010\)](#) from combined  $H\alpha$  and MIPS  $24 \mu\text{m}$  data using [Kroupa \(2008\)](#) IMF. The resulting SFRs are lower by a factor of  $\sim 1.5$  compared to a [Salpeter \(1955\)](#) IMF. Column (3): observed velocity amplitude obtained as follows: for spirals, it is the observed maximum rotational velocity; for the E/S0 sample it is the luminosity-weighted squared velocity (i.e.,  $v = \sqrt{\langle v^2 \rangle}$ ) within  $1 R_{\text{eff}}$ ; for LBAs the velocity amplitude has been defined as the  $v_{\text{shear}}$  in this work. Column (4): velocity dispersion derived as follows: for spirals, it is the (uniformly weighted) mean velocity dispersion; for E/S0s it is the luminosity-weighted squared velocity dispersion (i.e.,  $\sigma = \sqrt{\langle \sigma^2 \rangle}$ ) within  $1 R_{\text{eff}}$ ; for LBAs the velocity dispersion is the average velocity dispersion of each spaxel, weighted by flux. Column (5): dynamical ratio determined as the ratio between the values shown in Cols. (3) and (4). Column (6): effective radius for the different samples. For spirals it has been derived as half of the optical radius ( $R_{\text{opt}}$ ) associated with the isophotal level at 25 mag arcsec $^{-2}$  in the  $B$ -band, where  $R_{\text{opt}} = 1.9 \times R_{\text{eff}}$  (see [Epinat et al. 2009](#)); for E/S0 the half-light radius is measured in the  $I$ -band from WPC2/HST images; for LBAs the effective radius was derived by selecting  $N$  spaxels with  $S/N > 6$  such that  $R_{\text{eff}} = \sqrt{(N/\pi)}$  (see [Law et al. 2007](#)). Column (7): dynamical mass determined as follows: for spirals we compute the total mass using the formula employed in their paper for rotation-dominated objects; we compute the dynamical masses for E/S0 using the formula  $K\sigma^2 R_{\text{eff}}/G$  as explained in [Cappellari et al. \(2006\)](#); finally, the dynamical masses of LBAs have been derived in [Gonçalves et al. \(2010\)](#) using the formula  $5\sigma^2 R_{\text{eff}}/G$ .

**Fig. 3.** Relationship between the central velocity dispersion,  $\sigma_c$ , of the systemic component and its mean velocity dispersion over the observed area,  $\sigma_{\text{mean}}$ , for the three different morphological classes. The color code is the same as the one used in Fig. 2.

AO-assisted IFS works of high- $z$  SFG samples (e.g., [Law et al. 2007](#); [Förster Schreiber et al. 2009](#); [Swinbank et al. 2012](#)), which can reach a sub-kpc scale of the order of those of low- $z$  (U)LIRGs observed under seeing-limited conditions.

In the following section we discuss the dynamical ratio  $v/\sigma$  and its dependence on the kinematical and morphological classes.

#### 4.3. Dynamical support in (U)LIRGs

The dynamical ratio between the velocity amplitude and the local velocity dispersion  $v/\sigma$  of a system is a useful parameter to kinematically characterize a system. It allows the distinction between rotation-dominated  $v/\sigma > 1$  and

random-motion-dominated systems  $v/\sigma < 1$  (e.g., [Epinat et al. 2012](#) and references there in). We note that for systems whose kinematic is dominated by tidal forces and/or radial motions (e.g., outflows),  $v_{\text{shear}}$  may not be tracing rotation. Similarly, in those cases  $\sigma_{\text{mean}}$  does not necessarily give a measure of velocity dispersion, but it can be the result of integrating several kinematically distinct components. However, since only a small fraction of systems show complex kinematics (see Sect. 4.1) and a kinematic decomposition has been applied (Sects. 3.1.1 and 3.1.2.),  $v_{\text{shear}}$  and  $\sigma_{\text{mean}}$  should trace, respectively, rotation and dispersion in most of the cases.

##### 4.3.1. From rotating disks to dispersion-dominated systems

In Fig. 4 the dynamical ratio  $v/\sigma$  with respect to the mean velocity dispersion is presented. A clear trend is shown among the different morphological classes with *disk* (class 0) galaxies having higher  $v/\sigma$  than objects in a more advanced interaction/merging phase (classes 1, 2; see Table 2)<sup>6</sup>.

Kinematical data of samples of nearby galaxies with available IFS are also included for comparison: elliptical/lenticular galaxies drawn from the SAURON project, studying the stellar kinematics (e.g., [Cappellari et al. 2007](#)), local spiral galaxies selected from the Gassendi  $H\alpha$  survey of Spirals (GHASP, [Epinat et al. 2010](#)), and LBAs at redshift  $\sim 0.2$  observed in  $H\alpha$  with OSIRIS/Keck (i.e., [Gonçalves et al. 2010](#))<sup>7</sup>. We note that these works use slightly different definitions for  $v$  and  $\sigma$ , but these have no significant impact on the interpretation of the  $v/\sigma$  over  $\sigma$  relationship (see caption of Fig. 4).

<sup>6</sup> Although there are two class 0 objects with relatively low  $v/\sigma$  (high  $\sigma$ ), we note that one (IRAS F13229-2934,  $v/\sigma \sim 1.4$ ) is known to be affected by the presence of an AGN ([Arribas et al. 2012](#)).

<sup>7</sup> While the LBAs have star formation rates (SFRs) similar to our local LIRGs, the spiral and E/S0 samples have considerably smaller rates (see Table 3).

**Table 4.** Kinematic properties of the narrow component for the (U)LIRGs sample.

Galaxy ID (IRAS code)	$v_{\text{sys}}$ (km s <sup>-1</sup> )	$v_{\text{amp}}$ (km s <sup>-1</sup> )	$v_{\text{shear}}$ (km s <sup>-1</sup> )	$\sigma_{\text{mean}}$ (km s <sup>-1</sup> )	$\sigma_c$ (km s <sup>-1</sup> )	$\frac{v_{\text{shear}}^*}{\sigma_{\text{mean}}}$	$i$ degree	$\delta v$ (km s <sup>-1</sup> spx <sup>-1</sup> )	$K$ class	$M_{\text{dyn}}$ (10 <sup>10</sup> $M_{\odot}$ )	Com
(1)	(2)	(3)	(4)	(5)	(6)	(7)	(8)	(9)	(10)	(11)	(12)
F06295-1735	6373	107 ± 15	87 ± 8	32 ± 9	44 ± 7	3.5 ± 1.1	52 ± 7	4.6	PD	1.9 ± 0.6	vii
F06592-6313	6942	160 ± 11	151 ± 9	49 ± 20	96 ± 20	3.6 ± 1.5	58 ± 8	12.7	PD	2.0 ± 0.8	v
F07027-6011 S	9270	95 ± 34	81 ± 10	69 ± 14	59 ± 5	2.4 ± 0.7	29 ± 4	12.7	RD	2.4 ± 1.1	v
F07027-6011 N	9582	124 ± 14	115 ± 9	38 ± 9	63 ± 10	3.9 ± 1.0	50 ± 5	10.4	PD	–	iii, v
F07160-6215	3297	237 ± 28	202 ± 10	55 ± 18	128 ± 17	3.8 ± 1.2	75 ± 3	6.2	PD (CK)	8.0 ± 1.4	iv, vii
F10015-0614	5143	218 ± 29	196 ± 7	51 ± 7	60 ± 10	4.3 ± 0.7	63 ± 3	5.3	PD	7.7 ± 1.6	iv, vii
F10409-4556	6241	214 ± 12	193 ± 8	39 ± 9	90 ± 13	5.4 ± 1.3	68 ± 6	7.2	RD	5.3 ± 1.2	iv, v
F10567-4310	5129	149 ± 11	122 ± 9	28 ± 4	52 ± 8	6.4 ± 1.1	42 ± 2	5.9	RD	5.1 ± 1.7	iv, v
F11255-4120	4958	149 ± 13	125 ± 9	30 ± 13	82 ± 25	5.1 ± 2.3	56 ± 2	5.4	PD	2.9 ± 0.9	v
F11506-3851	3114	202 ± 9	184 ± 6	40 ± 8	81 ± 18	7.6 ± 1.6	37 ± 3	13.7	RD	4.9 ± 1.2	v
F12115-4656	5282	221 ± 29	212 ± 4	46 ± 8	78 ± 20	6.9 ± 1.4	42 ± 3	12.8	RD	11.5 ± 3.2	v
F13229-2934	4059	115 ± 24	80 ± 14	59 ± 6	64 ± 10	2.2 ± 0.5	37 ± 3	5.6	CK	3.5 ± 1.6	vii
F22132-3705	3500	186 ± 5	172 ± 3	33 ± 10	76 ± 15	6.2 ± 1.9	56 ± 4	7.7	RD	10.5 ± 1.8	iv, v
F01159-4443 S	6930	130 ± 17	117 ± 13	46 ± 11	71 ± 16	3.7 ± 1.1	46 ± 8	13.6	PD	3.0 ± 1.2	ii, iv, vii
F01159-4443 N	6792	145 ± 25	119 ± 13	51 ± 12	50 ± 8	6.3 ± 3.0	22 ± 9	16.6	PD	5.0 ± 4.4	ii, vii
F01341/ESO G12	5240	199 ± 59	156 ± 45	90 ± 15	61 ± 18	2.2 ± 0.8	52 ± 10	6.4	PD	6.1 ± 5.5	i, vii
F01341/ESO G11	5200	111 ± 11	93 ± 6	33 ± 6	43 ± 9	7.3 ± 3.5	23 ± 11	10.8	PD	3.5 ± 2.3	vii
F06035-7102	23867	184 ± 27	150 ± 26	74 ± 19	63 ± 18	2.6 ± 1.4	52 ± 26	12.9	CK	9.5 ± 8.1	vi
F06076-2139 S	11810	118 ± 38	89 ± 18	43 ± 14	51 ± 11	3.4 ± 1.3	37 ± 3	10.7	PD	3.5 ± 1.5	ii, v
F06076-2139 N	11199	83 ± 52	77 ± 24	86 ± 13	87 ± 11	1.2 ± 0.5	46 ± 11	17.2	PD	3.3 ± 1.2	i, ii, iv, v
F06206-6315	27669	203 ± 21	189 ± 18	64 ± 13	75 ± 23	3.1 ± 0.7	76 ± 10	10.3	PD	4.8 ± 1.5	v
F06259-4780 S	11736	213 ± 19	198 ± 13	53 ± 4	37 ± 6	4.7 ± 0.7	53 ± 9	22.5	RD	7.9 ± 2.9	i, v
F06259-4780 C	11587	104 ± 22	89 ± 12	54 ± 11	47 ± 13	1.9 ± 0.5	62 ± 11	6.6	RD	1.1 ± 0.5	ii, v
F06259-4780 N	11935	229 ± 41	180 ± 64	91 ± 25	77 ± 19	2.3 ± 1.1	58 ± 9	20.7	RD	2.6 ± 1.7	ii, v
08424-3130 S	4914	133 ± 31	119 ± 23	60 ± 7	83 ± 25	2.5 ± 1.2	52 ± 26	11.0	PD	2.8 ± 2.3	ii, iv, vi
08424-3130 N	5029	67 ± 50	66 ± 27	114 ± 16	119 ± 17	0.7 ± 0.5	52 ± 26	–	–	4.6 ± 1.6	ii, iv, vi, viii
F08520-6850 E	13518	123 ± 10	109 ± 15	77 ± 10	100 ± 40	1.6 ± 0.3	62 ± 6	7.9	RD	2.0 ± 0.7	ii, vii
F08520-6850 W	13736	196 ± 12	191 ± 16	73 ± 14	92 ± 20	2.7 ± 0.6	77 ± 4	12.6	PD (RD)	11.3 ± 2.8	ii, vii
F09437+0317 S	5966	236 ± 22	214 ± 9	40 ± 7	50 ± 9	6.1 ± 1.2	63 ± 4	8.0	RD	8.6 ± 1.7	i, v
F09437+0317 N	5983	134 ± 11	189 ± 6	34 ± 5	56 ± 8	6.0 ± 1.0	68 ± 5	4.1	RD	12.3 ± 2.8	iv, v
12043-3140 S	7009	191 ± 35	171 ± 11	101 ± 15	82 ± 21	2.4 ± 0.4	52 ± 2	12.7	PD	6.3 ± 1.6	ii, v
12043-3140 N	7030	54 ± 10	42 ± 10	43 ± 14	51 ± 8	1.2 ± 0.7	52 ± 26	6.5	PD (CK)	0.3 ± 0.2	ii, vi
F12596-1529	4875	163 ± 22	143 ± 14	64 ± 14	66 ± 18	2.3 ± 0.6	75 ± 3	5.9	–	3.5 ± 1.4	iv, vii, viii
F14544-4255 E	4714	220 ± 88	200 ± 15	60 ± 7	63 ± 6	3.5 ± 0.5	78 ± 4	7.6	PD	10.4 ± 3.0	i, vii
F14544-4255 W	4800	146 ± 35	127 ± 11	86 ± 37	82 ± 16	1.7 ± 0.8	59 ± 7	8.7	CK (PD)	2.4 ± 2.3	i, vii
F18093-5744 S	5328	155 ± 7	141 ± 10	48 ± 9	62 ± 13	1.2 ± 0.3	53 ± 6	10.3	RD	3.4 ± 1.3	v
F18093-5744 C	4969	130 ± 25	96 ± 21	96 ± 9	77 ± 25	4.4 ± 0.8	56 ± 4	7.3	CK (PD)	>0.4 ± 0.3	i, vii
F18093-5744 N	5184	159 ± 9	147 ± 3	46 ± 8	58 ± 7	3.7 ± 0.8	47 ± 3	7.0	RD	3.6 ± 1.1	v
F22491-1808	23283	88 ± 44	80 ± 24	83 ± 11	71 ± 19	1.4 ± 0.5	44 ± 3	10.6	CK (PD)	3.4 ± 1.7	v
F23128-5919	13448	260 ± 62	152 ± 75	103 ± 21	110 ± 23	1.9 ± 1.0	53 ± 8	14.2	CK	2.7 ± 1.2	vii

**Notes.** Derived  $H\alpha$  kinematic quantities for the narrow (systemic) component. Horizontal lines distinguish class 0, 1, and 2 (from top to bottom, respectively). Column (1): IRAS name. Column (2): systemic velocity calculated as the  $H\alpha$  radial velocity. A mean error of 5–7 km s<sup>-1</sup> should be added when calibration and fitting errors are considered. Column (3):  $H\alpha$  velocity amplitude defined as the half of the observed “peak-to-peak” velocity (i.e., half the difference between the maximum and minimum values is considered without applying the inclination correction). Column (4):  $H\alpha$  velocity shear defined as the half of the difference between the median of the 5 percentile at each end of the velocity distribution (i.e.,  $v_{\text{max}}^{5\%}$  and  $v_{\text{min}}^{5\%}$ ), as in Gonçalves et al. (2010) (not corrected for the inclination). Column (5):  $H\alpha$  mean velocity dispersion. Column (6):  $H\alpha$  central velocity dispersion, derived as the mean of  $4 \times 4$  spaxels around the VIMOS continuum flux peak. Column (7): dynamical ratio between the velocity shear (corrected for the inclination) and the mean velocity dispersion values. Column (8): inclination of the galaxy, defined as  $i = \cos^{-1}(b/a)$  (i.e., where  $a$  and  $b$  are, respectively, the major and minor axes of the object). When possible, it has been inferred directly from the  $H\alpha$  map or continuum images (i.e., DSS, HST and 2MASS). When the morphology of the object was too complex, we assumed a mean inclination of about  $52^\circ \pm 26^\circ$ , equivalent to  $\langle \sin i \rangle = 0.79 \pm 0.35$  (see Appendix in Law et al. 2009). In this case, the uncertainty of the inclination has been computed as the standard deviation of the distribution of the different measures derived when  $i$  varies from  $0^\circ$  to  $90^\circ$ , using step of  $1^\circ$ . See details in Col. 12, notes (v, vi, vii). Column (9): velocity gradient (km s<sup>-1</sup>) associated with one spaxel derived as explained in the text. Column (10): kinematical classification inferred from the kinematic maps. RD stands for rotating disk, PD perturbed disk and CK are systems with complex kinematics (see text for details). The galaxy IRAS 08424-3130 N is in the edge of the FoV, and its kinematic classification was not possible. For those objects for which the kinematical classification is controversial, the possible classifications are shown in the table. Column (11): dynamical masses (see text). Column (12): comments with the following code: (i) after distributing the total IR luminosity between the individual objects forming the system, this galaxy does not qualify as LIRG as its luminosity is lower  $10^{11} L_{\odot}$ . The galaxies IRAS F01341-3735 N and IRAS F09437+0317 N are in the limit to be classified as LIRG (see Col. 6 in Table 1). (ii) Systems for which a mask has been applied to the data-cube in order to analyze separately the sources (e.g., N and S stand for northern and southern galaxies). (iii) No  $R_{\text{eff}}^{\text{IR}}$  reliable due to AGN contamination (see Arribas et al. 2012 and App. B for details). (iv) For this galaxy two pointings have been combined to derive the kinematic values. (v) The inclination has been derived using the  $H\alpha$  map. (vi) A mean inclination (i.e.,  $52^\circ \pm 26^\circ$ ) has been considered. (vii) The inclination has been derived using continuum available images (i.e., HST or DSS or 2MASS). (viii) The kinematic classification was not possible due to the poor linear resolution for IRAS F12596-1529, while the emission of the IRAS F08424-3130 N is only partially included in the FoV.

Table 4. continued.

Galaxy ID (IRAS code)	$v_{\text{sys}}$ (km s <sup>-1</sup> )	$v_{\text{amp}}$ (km s <sup>-1</sup> )	$v_{\text{shear}}$ (km s <sup>-1</sup> )	$\sigma_{\text{mean}}$ (km s <sup>-1</sup> )	$\sigma_c$ (km s <sup>-1</sup> )	$\frac{v_{\text{shear}}^*}{\sigma_{\text{mean}}}$	$i$ degree	$\delta v$ (km s <sup>-1</sup> spx <sup>-1</sup> )	$K$ class	$M_{\text{dyn}}$ (10 <sup>10</sup> M <sub>⊙</sub> )	Com
(1)	(2)	(3)	(4)	(5)	(6)	(7)	(8)	(9)	(10)	(11)	(12)
F04315-0840	4668	162 ± 36	134 ± 11	63 ± 28	70 ± 28	2.5 ± 1.1	58 ± 4	5.6	CK	1.7 ± 0.7	vii
F05189-2524	12808	30 ± 19	27 ± 8	91 ± 10	90 ± 10	0.9 ± 0.5	18 ± 9	6.3	CK	–	iii, vii
08355-4944	7782	73 ± 14	60 ± 9	51 ± 12	44 ± 12	1.5 ± 0.8	52 ± 26	5.0	PD	0.5 ± 0.4	vi
09022-3615	17918	110 ± 36	89 ± 15	162 ± 12	105 ± 12	1.1 ± 0.2	29 ± 2	12.1	CK	8.1 ± 2.5	v
F10038-3338	10287	54 ± 18	45 ± 8	68 ± 16	64 ± 16	0.8 ± 0.4	52 ± 26	5.8	CK	1.3 ± 0.7	vi
F10257-4339	2813	170 ± 34	132 ± 20	56 ± 7	65 ± 7	3.3 ± 0.9	45 ± 10	6.5	PD	3.2 ± 1.7	iv, vii
12116-5615	8163	52 ± 19	44 ± 10	66 ± 9	51 ± 9	0.9 ± 0.2	48 ± 4	7.3	PD	0.8 ± 0.4	v
F13001-2339	6540	169 ± 110	142 ± 27	120 ± 25	116 ± 34	1.3 ± 0.5	65 ± 4	11.9	CK	11.4 ± 8.3	v
F17138-1017	5274	144 ± 21	128 ± 12	67 ± 11	59 ± 11	2.4 ± 0.5	52 ± 8	12.9	PD	2.6 ± 0.7	vii
F21130-4446	28028	228 ± 28	223 ± 19	90 ± 12	69 ± 12	3.2 ± 1.5	52 ± 26	22.1	CK	20.7 ± 16.8	vi
F21453-3511	4816	78 ± 29	53 ± 10	42 ± 14	70 ± 14	1.6 ± 0.6	51 ± 2	3.7	PD	0.9 ± 0.6	iv, vii

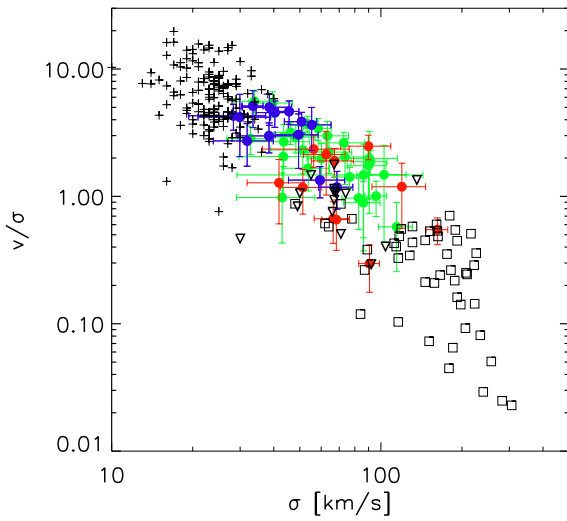


**Fig. 4.** Relationship between the observed dynamical ratio  $v/\sigma$ , taking here the  $v_{\text{shear}}/\sigma_{\text{mean}}$  (see text) and the mean velocity dispersion. Color code is the same as the one adopted in previous figures. The plus signs represent spiral GHASP galaxies (i.e., [Epinat et al. 2010](#)), empty squares E/SO objects (i.e., [Cappellari et al. 2007](#)), and top-down empty triangles LBAs (i.e., [Gonçalves et al. 2010](#)). For the spirals the  $v$  parameter is defined as the maximum amplitude of the rotational curve within the extent of the velocity field along the major axis, and  $\sigma$  is the average of the velocity dispersion map. For E/SO,  $v$  and  $\sigma$  are luminosity-weighted square quantities derived, respectively, from the velocity field and velocity dispersion maps (see details in [Cappellari et al. 2007](#)). For the LBAs, the velocity shear  $v_{\text{shear}}$  has been defined as in this work, while the velocity dispersion is the flux-weighted mean value.

The (U)LIRGs fill the gap between rotation-dominated spirals and dispersion-dominated ellipticals in the  $v/\sigma$ - $\sigma$  plane. In particular, there is a clear transition among (U)LIRGs, with isolated (class 0), interacting (class 1), and merging (class 2) sources tending to increase their mean velocity dispersion while decreasing the velocity amplitude, therefore moving from high- $\sigma$  and low- $v/\sigma$  spirals to low- $\sigma$  and high- $v/\sigma$  ellipticals. Moreover, systems classified as class 0 (LIRGs in all cases) have mean velocities  $v_{\text{shear}} = (150 \pm 14)$  km s<sup>-1</sup> similar to those of spirals (mean velocity amplitude of  $\sim 160$  km s<sup>-1</sup>) but with much higher velocity dispersion  $\sigma_{\text{mean}}$  (i.e.,  $44 \pm 4$  km s<sup>-1</sup>, while 24 km s<sup>-1</sup> for spirals, see Table 3). This suggests that class 0 LIRGs are rotating disks, more turbulent and thicker than those of normal spirals. Therefore, the main difference between the global kinematic properties of these two samples, rather than

the rotational amplitude, is the mean velocity dispersion, which is higher for LIRG disks. On the other hand, interacting (class 1) and merging systems (class 2) have lower dynamical ratios, with kinematical values closer to those obtained for the ellipticals. The trend observed in this plot is consistent with the idea that the process of merging in (U)LIRGs possibly transforms spiral galaxies into intermediate-mass ellipticals (e.g., [Genzel et al. 2001](#); [Tacconi et al. 2002](#); [Dasyra et al. 2006b](#)). These class 1 and 2 systems even share similar kinematical properties with the LBAs (see Tables 2 and 3), discussed in detail in Sect. 4.4.4.

When the number of resolution elements that characterizes a galaxy is small (i.e., galaxy size  $\sim$  PSF), the determination of the  $\sigma_{\text{mean}}$  values may be affected by the smearing of the velocity field and may lead to artificial peaks in the  $\sigma$ -map (see [Davies et al. 2011](#)). Due to the linear resolution limitations, this effect becomes common at higher redshift, as discussed in previous works (e.g., [Förster Schreiber et al. 2009](#); [Epinat et al. 2010](#)). However, for local samples, which are observed with much higher linear resolution, this effect is generally neglected. Indeed, this correction was not applied for the local comparison samples used here (i.e., spiral and elliptical/lenticular galaxies). Our LIRGs have spatial scales somewhat larger than those characterizing those systems<sup>8</sup>, but the smearing effects are still in general very small<sup>9</sup> and corrections for the individual galaxies have not been applied.

On the other hand, there could be some bias when directly comparing our results with those of LBAs at  $z \sim 0.2$  (i.e., [Gonçalves et al. 2010](#)). They actually compute the mean velocity dispersion using a flux-weighted quantity. As stated in [Davies et al. \(2011\)](#), a flux-weighted mean velocity dispersion is biased towards bright regions, typically closer to the center, where the intrinsic rotation curve has a steeper gradient: the smearing is potentially more important and the mean velocity dispersion derived in [Gonçalves et al. \(2010\)](#) might be therefore considered as an upper limit<sup>10</sup>.

<sup>8</sup> The typical linear resolutions (seeing  $FWHM \sim 1''$ ) of GHASP spirals and E/SO galaxies are, respectively, 0.27 kpc and 0.09 kpc, while for our LIRGs and ULIRGs they are 0.48 kpc and 1.32 kpc, respectively.

<sup>9</sup> To estimate the smearing effects in our data, we have calculated the velocity gradients along the central regions of our systems and derived the typical range in velocities across a spaxel ( $\delta v$ ). When quadratically subtracting  $\delta v$  from  $\sigma$ , it was confirmed that the effects of smearing are negligible (a few percent) for most of the systems. In the worst case (i.e., IRAS F06259-4780 S) the effect was  $\sim 15\%$  (see Table 4).

<sup>10</sup> The values of the flux-weighted mean velocity dispersion can be a factor of 1.5–3 larger than those derived for the uniformly weighted mean velocity dispersion (see [Davies et al. 2011](#)).



**Table 5.** Kinematic properties of the broad component for the (U)LIRGs sample.

Galaxy ID (IRAS code)	$v_{\text{amp}}$ (km s <sup>-1</sup> )	$\sigma_{\text{mean}}$ (km s <sup>-1</sup> )	Area (kpc <sup>2</sup> )	$v_{\text{amp}}/\sigma_{\text{mean}}$	$\Delta v$ offset (km s <sup>-1</sup> )
(1)	(2)	(3)	(4)	(5)	(6)
F06295-1735	90 ± 35	110 ± 23	1.33	0.8 ± 0.4	-3
F06592-6313	217 ± 133	219 ± 18	1.2	1.0 ± 0.6	-285
F07027-6011S	59 ± 10	124 ± 8	6.0	0.5 ± 0.1	-17
F07027-6011N	17 ± 5	316 ± 12	5.1	0.05 ± 0.02	-256
F07160-6215	152 ± 22	91 ± 12	0.3	1.7 ± 0.3	55
F10015-0614	66 ± 32	103 ± 12	1.1	0.6 ± 0.3	-37
F10409-4556	90 ± 97	82 ± 69	0.5	1.1 ± 1.5	-120
F10567-4310	65 ± 47	138 ± 19	1.0	0.5 ± 0.4	-54
F11255-4120	52 ± 49	178 ± 14	0.5	0.3 ± 0.3	-83
F11506-3851	77 ± 30	76 ± 16	0.3	1.0 ± 0.5	-42
F12115-4656	21 ± 20	93 ± 12	1.0	0.2 ± 0.1	69
F13229-2934	143 ± 30	191 ± 40	2.5	0.7 ± 0.2	-39
F22132-3705	—	—	—	—	—
F01159-4443 S	76 ± 10	39 ± 8	1.5	2.0 ± 0.5	-159
F01159-4443 N	84 ± 13	142 ± 58	3.5	0.6 ± 0.3	-37
F01341/ESO G11	71 ± 20	110 ± 28	1.5	0.7 ± 0.3	-24
F01341/ESO G12	142 ± 25	114 ± 10	1.1	1.3 ± 0.3	-49
F06035-7102	19 ± 13	139 ± 25	16.2	0.1 ± 0.1	-28
F06076-2139 S	38 ± 35	91 ± 44	2.5	0.4 ± 0.4	-243
F06076-2139 N	7 ± 11	208 ± 8	1.7	0.03 ± 0.05	-100
F06206-6315	42 ± 38	198 ± 46	6.6	0.2 ± 0.2	-229
F06259-4780 S	—	—	—	—	—
F06259-4780 C	16 ± 15	111 ± 14	2.1	0.14 ± 0.14	63
F06259-4780 N	87 ± 34	133 ± 24	3.5	0.7 ± 0.4	76
08424-3130 S	22 ± 17	109 ± 12	0.5	0.7 ± 0.1	31
08424-3130 N	69 ± 64	128 ± 26	0.3	0.2 ± 0.6	-130
F08520-6850 E	—	—	—	—	—
F08520-6850 W	52 ± 40	130 ± 10	3.7	0.5 ± 0.3	-151
F09437+0317 S	—	—	—	—	—
F09437+0317 N	77 ± 53	106 ± 60	1.3	0.8 ± 0.6	-70
12043-3140 S	203 ± 145	144 ± 26	4.5	1.4 ± 1.0	-42
12043-3140 N	—	—	—	—	—
F12596-1529	145 ± 49	166 ± 14	0.9	0.9 ± 0.3	0
F14544-4255 E	189 ± 89	48 ± 62	0.6	3.9 ± 5.4	26
F14544-4255 W	175 ± 36	241 ± 46	1.5	0.7 ± 0.2	-52
F18093-5744 C	47 ± 24	105 ± 22	1.5	0.5 ± 0.3	-52
F18093-5744 N	34 ± 20	96 ± 15	0.8	0.4 ± 0.2	39
F18093-5744 S	68 ± 66	153 ± 34	0.6	0.4 ± 0.5	-85
F22491-1808	22 ± 22	117 ± 15	9.7	0.2 ± 0.2	-5
F23128-5919	435 ± 63	274 ± 85	54.7	1.6 ± 0.5	-32
F04315-0840	260 ± 54	211 ± 41	8.6	1.2 ± 0.4	-167
F05189-2524	59 ± 40	269 ± 28	14.5	0.2 ± 0.2	-400
08355-4944	63 ± 14	127 ± 10	7.9	0.5 ± 0.1	-19
09022-3615	35 ± 28	216 ± 17	11.9	0.16 ± 0.13	23
F10038-3338	82 ± 89	123 ± 44	2.5	0.7 ± 0.8	-100
F10257-4339	144 ± 38	106 ± 17	5.2	1.4 ± 0.4	-2
12116-5615	50 ± 20	154 ± 25	2.4	0.32 ± 0.14	-55
F13001-2339	137 ± 109	144 ± 38	1.6	1.0 ± 0.8	-24
F17138-1017	4 ± 3	83 ± 8	0.3	0.05 ± 0.04	65
F21130-4446	30 ± 34	113 ± 8	8.0	0.3 ± 0.3	-198
F21453-3511	113 ± 89	266 ± 43	1.3	0.4 ± 0.3	-129

**Notes.** Derived H $\alpha$  kinematic quantities for the broad component. Horizontal lines distinguish class 0, 1, and 2 (from top to bottom, respectively). Column (1): IRAS name. Column (2): velocity amplitude. Column (3): mean velocity dispersion. Column (4): area covered by the broad component. Column (5): dynamical ratio between the velocity amplitude (Col. 2) and the mean velocity dispersion (Col. 3). Column (6): velocity offset, computed as the difference between the mean velocity of the broad and the narrow components. Negative values represent blueshifted values while positive ones are redshifted.

#### 4.4. (U)LIRGs dynamical masses

##### 4.4.1. Derivation of dynamical mass

Dynamical mass determinations, which include the stellar, gas, and dark matter contributions, are relevant in the context of

(U)LIRGs for several reasons. First, these objects have large amounts of gas and, therefore, the stellar mass gives only a partial estimate to their total mass (i.e., [Downes & Solomon 1998](#); [Combes et al. 2011](#)). Second, in order to infer the stellar masses, the SED modeling is difficult due to the presence of several

stellar populations (Rodríguez Zaurín et al. 2010), large amounts of dust (e.g., da Cunha et al. 2010), and the complex structure of the extinction (García-Marín et al. 2009; Piqueras López et al. 2013). Therefore, stellar mass measurements not only have their own uncertainties, but intrinsically represent a lower limit to the mass of these systems.

Colina et al. 2005 have found that the warm gas kinematics in ULIRGs is in general coupled to that of the stellar component; therefore, it can be used as tracer of the gravitational potential. The kinematic properties of the ionized gas obtained from our IFS velocity maps are used in the following to estimate the dynamical mass,  $M_{\text{dyn}}$ .

As shown in previous sections, our sample contains systems with a wide range of kinematic properties, from regular rotating disk to merging systems. Hence, for deriving dynamical mass estimates we have used different approximations, distinguishing systems dominated by random motions from those with a large rotation component.

For spherical, bound, and dynamically relaxed systems with random motion, the dynamical mass can be estimated via the virial theorem as

$$M_{\text{dyn,vir}} = \frac{K R_{\text{hm}} \sigma^2}{G}, \quad (1)$$

where  $R_{\text{hm}}$  is the half-mass radius,  $\sigma$  is the mean velocity dispersion, the factor  $K$  takes into account the effects of structure on dynamics, and  $G$  is the gravitational constant (i.e.,  $4.3 \times 10^{-3} \text{ pc } M_{\odot}^{-1} (\text{km s}^{-1})^2$ ).  $R_{\text{hm}}$  cannot be obtained directly and is estimated by measuring the half-light radius,  $R_{\text{eff}}$ , which encloses half luminosity (see Sect. 4.4.2). Taylor et al. (2010) have recently studied the differential effects of nonhomology in the dynamical mass determinations based on this formula. In particular, they analyzed the dependence of the  $K$  factor on the galaxy structure, parametrized by the Sérsic index  $n$ , assuming a spherical mass distribution that is dynamically isotropic and non-rotating, and which, in projection, follows a Sérsic (1963, 1968) surface density profile. According to their expression, the  $K$  factor ranges between 7.4 ( $n = 1$ , exponential profile) and 4.7 ( $n = 4$ , de Vaucouleurs) and gives an idea of the differential effects due to nonhomology. We have considered a mean value of  $K = 6$ , which is also close to the one found by other authors<sup>11</sup> (e.g., Cappellari et al. 2006). Since this formula is only valid for non-rotating systems, we have applied it to galaxies with kinematics compatible with slow rotation (i.e.,  $v_{\text{shear}}^*/\sigma < 2$ , where the  $v_{\text{shear}}^*$  corresponds to the  $v_{\text{shear}}$  value corrected by inclination  $i$ ) and complex kinematic (CK) similar to those found by Colina et al. (2005) in ULIRGs.

For the rest of the systems showing a significant rotation component, we have derived the dynamical mass from the circular velocity, obtaining the mass enclosed within a given radius. In particular, we consider the total  $M_{\text{dyn}} = 2 M_{1/2}$ , where  $M_{1/2}$  is the dynamical mass within  $r_{1/2}$ , the radius that contains the three-dimensional half-light volume<sup>12</sup>. Thus, for an oblate spheroid (Williams et al. 2010),

$$M_{1/2} \approx \frac{v_c^2 R_{\text{eff}}}{G}, \quad (2)$$

<sup>11</sup> We note that the value of  $K = 6$  corresponds to  $m = 1.4$  in Eq. (1) given in Colina et al. (2005), who used  $m = 1.75$ , and therefore, the masses derived here are  $\sim 20\%$  lower than those derived with their formula.

<sup>12</sup> This radius is related to the effective radius by the relation  $r_{1/2} \approx 1.33 \times R_{\text{eff}}$ , for a wide range of radial profiles (e.g., Wolf et al. 2010).

where  $v_c$  is the circular velocity at  $r_{1/2}$ . To infer the circular velocity we have considered both the rotation and dispersion motions. In particular, we included the “asymmetric drift” term, which represents an extra component due to the dispersion of the gas around the disk of the galaxy, following the prescriptions by Epinat et al. (2009) and Williams et al. (2010). Assuming a disk scale length,  $h = \frac{r_{1/2}}{\sqrt{2 \ln 2}}$  (Epinat et al. 2009):

$$M_{\text{dyn}} \approx \frac{2 R_{\text{eff}} (v_{\text{rot}}^2 + 1.35 \sigma^2)}{G}, \quad (3)$$

where  $v_{\text{rot}}$  and  $\sigma$  are the rotation and dispersion velocities and are taken here as the inclination-corrected  $v_{\text{shear}}^*$ , and  $\sigma_{\text{mean}}$ , respectively.

Mass determination can be affected by large uncertainties. In addition to those related to the implicit assumptions of the above expressions, the observed parameters  $R_{\text{eff}}$ ,  $v_{\text{shear}}$ , and  $\sigma_{\text{mean}}$  have their own uncertainties. The use of different tracers (e.g., IR-continuum, H $\alpha$ ) may lead to discrepancies (see Sect. 4.4.2 for further details). Rotation velocities for individual objects can be significantly affected by the inclination correction, which therefore has an important impact on the  $M_{\text{dyn}}$  determination due to its quadratic dependence on  $v_{\text{shear}}^*$  in Eq. (3). For a relatively small number of objects (i.e., 8/51) we applied an average inclination correction following Law et al. 2009. Those have a relatively large uncertainty in  $i$ , but we apply Eq. (3) instead of Eq. (1) only for four. As for  $\sigma_{\text{mean}}$ , the fact that we are considering the values corresponding to the narrow component (Sect. 3.1) minimizes possible effects due to radial motions like outflows, which are generally associated with the broad component. We therefore estimate that the present masses should be corrected on average within a factor of  $\sim 3$ .

#### 4.4.2. Effective radii of (U)LIRGs

We derived the effective radii using near-IR continuum images (i.e.,  $H$ - and  $K$ -bands), which trace the bulk of the galaxy stellar component (see Appendix B). This spectral range also has the advantage of reducing the effects of the reddening, which can be significant in (U)LIRGs (i.e., García-Marín et al. 2009; Piqueras López et al. 2013). Specifically, we based our determinations on the 2MASS and HST imaging, which cover a wide FoV and have high angular resolution, respectively (see details in Appendix B). The mean  $R_{\text{eff}}$  for the (U)LIRGs sample is  $(2.6 \pm 1.3) \text{ kpc}$ . For the ULIRG subsample, we obtain a mean  $R_{\text{eff}}$  of  $(3.3 \pm 0.5) \text{ kpc}$ , which is in excellent agreement with the value of  $(3.48 \pm 1.39) \text{ kpc}$  obtained by Veilleux et al. (2002) using ground-based  $K$ -band imaging for most of the 118 ULIRGs of the IRAS 1 Jy sample.

Veilleux et al. (2002) also obtained  $R$ -band-based effective radii, which are on average 38 percent larger than in the  $K$ -band (i.e.,  $R_{\text{eff}}^R = 4.80 \pm 1.37 \text{ kpc}$ ). This difference can be attributed to the difference in extinction between the two bands, since after inspecting the original images (i.e., Kim et al. 2002) it is clear that the  $K$ -band images are considerably shallower than the  $R$  ones. Therefore, one should expect systematic differences lower than 40 percent when comparing visible and near IR continuum-based radii for these objects.

The sizes of the (U)LIRGs are compared with those of other local samples in Fig. 5 (left panel). On average, (U)LIRGs have smaller radii than local spirals, though the intrinsic scatter is rather large in both samples. In the present sample of (U)LIRGs, objects with radii as large as 7–20 kpc, such as those in the GHASP survey (i.e., derived in the B-band), are not seen. The E/SOs cover a range in size (measured using the H-band) larger

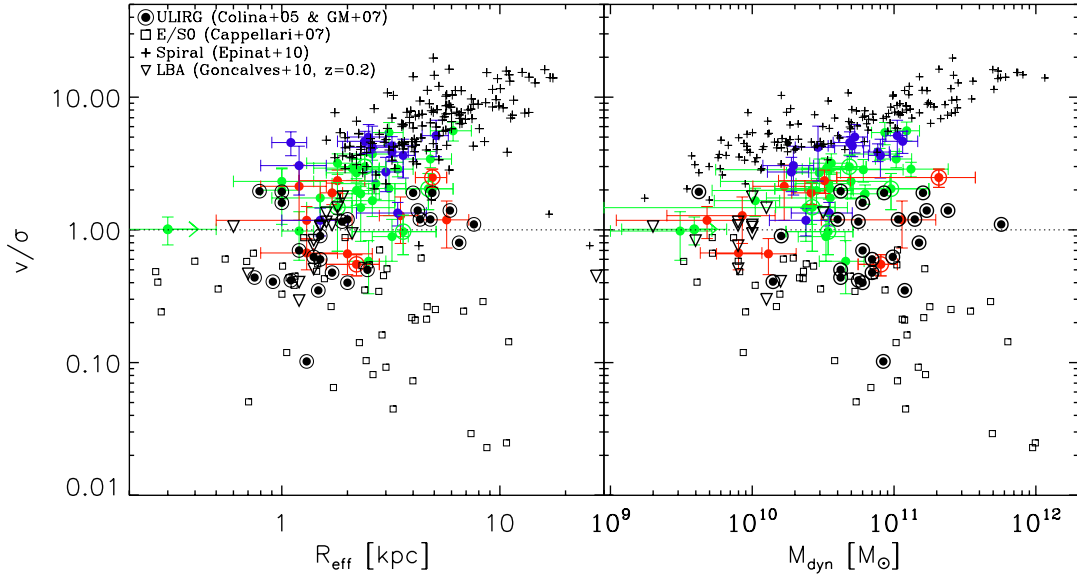


**Fig. 5.** Observed (i.e., not inclination corrected)  $v/\sigma$  ratio as a function of the effective radius  $R_{\text{eff}}$  (left panel) and dynamical mass  $M_{\text{dyn}}$  (right panel) is shown (see text). The colors used are the same as in the previous figures (i.e., blue for isolated disks, green for interacting galaxies and red for mergers). We identify ULIRGs with a second circle around the dots. The other samples are represented as follows: the nearby isolated spiral galaxies from the GHASP survey (see [Epinat et al. 2010](#)) are represented with cross symbols. Local ellipticals and lenticular objects, drawn from [Cappellari et al. \(2007\)](#), are shown with empty squares. LBAs, drawn from [Gonçalves et al. \(2010\)](#), are represented with empty downward triangles, with values derived using the Pa- $\alpha$  line. For these three samples, the effective radii  $R_{\text{eff}}$ , dynamical ratios  $v/\sigma$ , and dynamical masses  $M_{\text{dyn}}$  have been derived as explained in the caption of Table 3. We finally add the ULIRG systems studied in [Colina et al. \(2005\)](#) and those studied in [García-Marín et al. \(2007\)](#) (i.e., empty circle surrounding the black solid dot). In general, [Colina et al. \(2005\)](#) derived their effective radius from the  $H$ -band measured using  $F160W$  Near Infrared Camera and Multi-Object Spectrometer (NICMOS/HST) images (only for two sources were the  $F814W$  WFPC2/HST images used instead). In [García-Marín et al. \(2007\)](#) the effective radius considered is the one derived from the  $I$ -band (i.e.,  $F814W$ ) images. For both of the samples, their  $v/\sigma$  ratio is obtained considering the half peak-to-peak velocity difference, and the central velocity dispersion  $\sigma_c$ , applying one Gaussian component fitting to the  $H\alpha$  emission line data. Their dynamical masses are derived using a constant of  $K = 7.5$  (see footnote 9 for further details) and the central velocity dispersion  $\sigma_c$  ([Colina et al. 2005](#)).

than the (U)LIRGs, with a significant number of sources with  $R_{\text{eff}}$  smaller than 0.5 kpc and larger than 7 kpc. The ULIRG sample observed with INTEGRAL/WHT (i.e., [Colina et al. 2005](#); [García-Marín et al. 2009](#)) covers similar sizes as those of the present sample, with somewhat larger scatter. The derived LBA radii using Pa $\alpha$  emission are on average smaller by a factor of 0.7 than (U)LIRG radii. We note that  $H\alpha$  sizes are also somewhat smaller than IR-continuum-based determinations (i.e., [Arribas et al. 2012](#)).

#### 4.4.3. (U)LIRGs dynamical masses, and mass ratios in interacting systems

The dynamical mass estimates for the whole (U)LIRG sample range from  $\sim 5 \times 10^9 M_{\odot}$  to  $2 \times 10^{11} M_{\odot}$ , with a mean (median) value of  $(4.8 \pm 0.6) \times 10^{10} M_{\odot}$  ( $3.3 \times 10^{10} M_{\odot}$ ), confirming that (U)LIRGs are intermediate mass systems like previously suggested (i.e., [Tacconi et al. 2002](#); [Colina et al. 2005](#); though [Rothberg & Fischer 2010](#) and [Rothberg et al. 2013](#) find that (U)LIRGs masses are consistent with those of the most massive elliptical galaxies). In terms of  $m_{\star}$  (i.e.,  $m_{\star} = 1.4 \times 10^{11} M_{\odot}$ ; see [Cole et al. 2001](#)), these values correspond to a mean value of  $(0.35 \pm 0.04) m_{\star}$  and median of  $0.24 m_{\star}$ . The range of mass covered by the present (U)LIRGs overlaps with those of galaxies in the GHASP and SAURON, although these surveys also include galaxies with masses of  $\sim 7 m_{\star}$  (i.e.,  $\sim 10^{12} M_{\odot}$ ), which are not seen in our sample of (U)LIRGs.

The ULIRGs are more massive than LIRGs by, on average, a factor of about 2 (see Table 2). The present mean value for ULIRGs of  $(0.51 \pm 0.19) m_{\star}$  is between those obtained by [Colina et al. \(2005\) \(i.e.,  \$0.4 m\_{\star}\$ \) and \[Tacconi et al. \\(2002\\) \\(i.e.,  \\$0.86 m\\_{\star}\\$ \\). If the present sample of ULIRGs is combined with\]\(#\)](#)

those of [Colina et al. \(2005\)](#) and [García-Marín et al. \(2007\)](#) a mean and median mass values of  $(0.5 \pm 0.06) m_{\star}$  and  $0.3 m_{\star}$  are, respectively, derived. These are also in good agreement with those found in [Dasyra et al. \(2006b\)](#), where ULIRGs show dynamical masses between sub- and  $\sim m_{\star}$ .

The different morphological/kinematical classes do not show a clear trend with  $M_{\text{dyn}}$  (Table 2). The mean  $M_{\text{dyn}}$  for classes 0, 1, and 2 define a weak decreasing sequence, with relatively low statistical significance. Under the assumption that class 2 objects are made by the merger of two class 0 (or individuals classified as 1), one should expect masses for the mergers that are larger (by a factor 2) than those of individual pre-coalescence galaxies, contrary to what is found. To analyze this topic further, we selected the individual galaxies of ten pre-coalescence multiple systems (i.e., 19 LIRGs), and derived a mean dynamical mass and the respective mass ratio between each merging galaxy pair<sup>13</sup>. The mean dynamical mass derived for these sources is  $(0.33 \pm 0.05) m_{\star}$ : it seems too high when compared with the mean mass for the post-coalescence mergers (i.e.,  $M_{\text{dyn}} = 0.34 \pm 0.14 m_{\star}$ ). However, we point out the limited statistical significance of this result, especially taking into account that two objects (i.e., IRAS F09437+0317 N and IRAS F14544-4255 E) deviate about 3 standard deviation from rest. If these are excluded, a typical mass of  $(0.28 \pm 0.04) m_{\star}$  is obtained for pre-coalescence galaxies, a value that is still high if compared with that derived for class 2 objects. This can be explained as due to our  $L_{\text{IR}}$  selection: a low-mass system may exceed a

<sup>13</sup> For triple systems we consider the ratio between the two more massive sources. The dynamical mass estimation for the northern galaxy of the system F07027-6011 was not possible due to the presence of an AGN.



given infrared luminosity threshold only in the most intense starburst phase, while a higher mass system may pass this threshold even in a more quiescent phase. Since we select sources with  $L_{\text{IR}} > 10^{11} L_{\odot}$ , the fraction of large mass systems in the less active phases (e.g., type 0) is expected to be larger than in the most active ones (e.g., type 2).

A large fraction of the pre-coalescence systems (seven out of ten) have a mass ratio  $\leq 2.4$ , with a mean value of  $2.0 \pm 0.4$ , while the other three have ratios of 3, 4.3, and 20 (i.e., IRAS F06259-4780, IRAS F14544-4255, and IRAS F12043-3140<sup>14</sup>, respectively). These results are in good agreement with the findings by Dasyra et al. (2006a), who found that the majority of ULIRGs are triggered by almost equal-mass major mergers of 1.5:1 average ratio, which indicates that ULIRGs are mainly the products of almost equal mass mergers (i.e., sub- $m_{\star}$  galaxies; e.g., Tacconi et al. 2002; Colina et al. 2005; Dasyra et al. 2006b).

#### 4.4.4. Low- $z$ (U)LIRGs versus Lyman break analogs

While low- $z$  (U)LIRGs represent extreme IR-luminous, dusty starbursts in our nearby universe, other type of galaxies, the UV-luminous (i.e., LBA, Heckman et al. 2005), represent the class of (almost) extinction-free starbursts, showing SFRs similar to those of some local LIRGs (see Table 3). Both low- $z$  IR and UV-bright galaxies are also considered local analogs of SFGs at cosmological distances, SMGs, and LBGs, respectively. So, it is important to establish a direct comparison of the overall kinematics and dynamical mass estimates of both samples based on IFS. Mean kinematic properties and dynamical masses for both samples are given in Tables 2 and 3, respectively. The corresponding values for local spirals and ellipticals based on IFS are also given for comparison.

On average, IR-luminous galaxies are much more massive than the UV-luminous galaxies with LIRGs and ULIRGs about five and ten times more massive than LBAs, respectively. Differences also clearly exist between (U)LIRGs and LBAs in their kinematics. The observed mean dynamical ratio ( $v/\sigma$ ) for all (U)LIRGs is 2.5 larger than for LBAs, indicating that in general IR-luminous galaxies appear to be more rotation-supported than the UV-luminous galaxies. This is particularly true when only (U)LIRGs classified as isolated (class 0) are considered, while interacting (class 1) and merging (class 2) galaxies have, respectively, a ratio of  $2.3 \pm 0.2$  and  $1.3 \pm 0.2$ , with the latter being much closer to that derived for LBAs (i.e.,  $0.95 \pm 0.11$ ). Detailed HST imaging of LBAs detected faint tidal features and companions around all LBAs imaged (i.e., Overzier et al. 2008), suggesting that UV-bright starbursts are the product of an interaction or merger. Looking independently at the kinematic tracers (i.e., velocity amplitude and velocity dispersion), there is a clear trend among (U)LIRGs such that the amplitude of the velocity field decreases from isolated to interacting and merging systems while the velocity dispersion increases. The LBAs have a mean velocity dispersion (i.e.,  $71 \pm 6 \text{ km s}^{-1}$ ) much higher than that of isolated (U)LIRGs (i.e.,  $44 \pm 4 \text{ km s}^{-1}$ ); however they are similar to that of interacting (i.e.,  $67 \pm 3 \text{ km s}^{-1}$ ) and mergers (i.e.,  $80 \pm 11 \text{ km s}^{-1}$ ). These velocity dispersions are factors of 3 to 4 larger than those of normal spirals ( $24 \pm 0.5 \text{ km s}^{-1}$ , see Epinat et al. 2010), and indicate that the starburst and the interaction/merging process play a dominant role in establishing the

kinematic properties of the gas, likely due to combined effect of stellar winds and tidal forces.

So, independent of the overall mass of the system and of whether it is dusty (i.e., class 1 and 2 (U)LIRG) or not (i.e., LBA), the kinematics of low- $z$  starburst galaxies is dominated by the star formation and the tidal forces, and produces dynamically hot systems characterized by an average  $\sigma \sim 70\text{--}80 \text{ km s}^{-1}$  and  $v/\sigma \sim 1\text{--}2$ .

## 5. Summary and conclusions

Using the VIMOS IFS on the VLT, we have obtained spatially resolved kinematics (i.e., velocity fields and velocity dispersion maps) of 38 local ( $z < 0.1$ ) LIRGs and ULIRGs (51 individual sources). The sample includes sources with different morphological types (i.e., spirals, interacting systems, merger remnants) and is therefore well suited to study the kinematic properties of the (U)LIRG population showing different dynamical phases. A large fraction of the sample galaxies (31/38) covers the relatively less studied LIRG luminosity range, which fills the gap between the ULIRGs and the population of star-forming galaxies at large. This sample has been supplemented by a sample of low- $z$  ULIRGs with their own available IFS (i.e., INTEGRAL/WHT data).

The main results of the present study can be summarized as follows:

1. The  $H\alpha$  emission line profile is well fitted with one or two Gaussians per emission line in most of the spectra, which have allowed us to identify two kinematically distinct components in the systems. One of these components (i.e., “systemic” or “narrow” component) is found over the whole line-emitting region of the system is characterized by spatially resolved mean velocity dispersions of  $\sigma_{\text{mean}} \approx 30\text{--}160 \text{ km s}^{-1}$ . The second component (“broad” component) is found in the inner (spatially resolved) regions of most of LIRGs and ULIRGs. It is characterized by relatively large line widths  $\sigma_{\text{mean}} \sim 320 \text{ km s}^{-1}$ , and its central velocity is blueshifted with respect to the systemic component for most of the objects with values up to  $\sim 400 \text{ km s}^{-1}$ . The largest extensions and extreme kinematic properties of the broad component are observed in interacting and merging systems. This component likely traces nuclear outflows.
2. The systemic component traces the overall velocity field and shows a large variety of kinematic 2D structures, from very regular velocity patterns typical of pure RD (29%) to kinematically PD (47%), and highly disrupted and CK (24%). Thus, most of the objects (76%) are dominated by rotation. This fraction is larger than previously found in samples of ULIRGs. In fact, we found that the importance of rotation anti-correlates with the infrared luminosity, with a higher fraction of objects with complex kinematics among ULIRGs than in LIRGs (respectively, 6/7 vs. 6/42).
3. We find a clear correlation between the different phases of the merging process and the mean kinematic properties inferred from the velocity maps. In particular, isolated disks, interacting galaxies, and merging systems define a sequence of increasing mean velocity dispersion and decreasing velocity field amplitude, which is characterized by intrinsic average dynamical ratios ( $v^*/\sigma$ ) of 4.7, 3.0, and 1.8, respectively. We also find that the  $\sigma_c/\sigma_{\text{mean}}$  vs.  $\sigma_{\text{mean}}$  plane is an excellent discriminator between disks and interacting/merging systems, with disks showing higher  $\sigma_c/\sigma_{\text{mean}}$  and lower  $\sigma_{\text{mean}}$  values by factors of 1.5 to 2, on average.

<sup>14</sup> Although the relatively high dynamical mass ratio derived for the system IRAS F12043-3140 would suggest that the northern source might be considered as a satellite-galaxy of the southern one, the relative stellar distribution (i.e., continuum map) suggests that the northern system is almost face-on and the mass ratio may be smaller.

4. In terms of dynamical support ( $v/\sigma$ ), the sample covers the gap between local spirals and E/SOs. The LIRGs classified as isolated disks partially overlap with the values of local spirals, with similar velocity amplitudes but larger mean velocity dispersions  $\sigma_{\text{mean}}$  (44 vs. 24 km s<sup>-1</sup>), implying a larger turbulence and thicker disks. Interacting systems and mergers have values closer to those of low-velocity dispersion E/SOs, though with higher velocity amplitudes.
5. The dynamical mass estimates for the present (U)LIRG sample range from  $\sim 0.04$  to  $1.4 m_{\star}$ , with ULIRGs ( $\sim 0.5 \pm 0.2 m_{\star}$ ) more massive than LIRGs by, on average, a factor of about 2. The mass ratio of individual pre-coalescence galaxies are  $< 2.5$  for most of the systems, confirming that most (U)LIRG mergers involve sub- $m_{\star}$  galaxies of similar mass.
6. The subclass of (U)LIRGs classified as mergers and the LBAs share similar kinematic properties, although the dynamical mass of LBAs is a factor 5 smaller, on average. This is a clear indication that, independent of the mass of the system and of whether it is dusty or dust-free, starburst winds and tidally induced forces produce dynamically hot systems characterized by  $\sigma \sim 70\text{--}80$  km s<sup>-1</sup> and  $v/\sigma \sim 1\text{--}2$ .

**Acknowledgements.** We thank the anonymous referee for useful comments and suggestions that helped to improve the quality and presentation of the paper. Thanks are also due to Javier Rodríguez-Zaurín and Mark Westmoquette for the useful discussions. This work was funded in part by the Marie Curie Initial Training Network ELIXIR of the European Commission under contract PITN-GA-2008-214227. This work has been supported by the Spanish Ministry of Science and Innovation (MICINN) under grant ESP2007-65475-C02-01. It is based on observations carried out at the European Southern Observatory, Paranal (Chile), Programs 076.B-0479(A), 078.B-0072(A), and 081.B-0108(A). This research made use of the NASA/IPAC Extragalactic Database, which is operated by the Jet Propulsion Laboratory, California Institute of Technology, under contract with the National Aeronautic and Space Administration.

## References

- Arribas, S., & Colina, L. 2003, *ApJ*, 591, 791
- Arribas, S., Colina, L., & Borne, K. D. 2000, *ApJ*, 545, 228
- Arribas, S., Colina, L., & Clements, D. 2001, *ApJ*, 560, 160
- Arribas, S., Bushouse, H., Lucas, R. A., Colina, L., & Borne, K. D. 2004, *AJ*, 127, 2522
- Arribas, S., Colina, L., Monreal-Ibero, A., et al. 2008, *A&A*, 479, 687
- Arribas, S., Colina, L., Alonso-Herrero, A., et al. 2012, *A&A*, 541, A20
- Bedregal, A. G., Colina, L., Alonso-Herrero, A., & Arribas, S. 2009, *ApJ*, 698, 1852
- Belloocchi, E., Arribas, S., & Colina, L. 2012, *A&A*, 542, A54
- Cappellari, M., Bacon, R., Bureau, M., et al. 2006, *MNRAS*, 366, 1126
- Cappellari, M., Emsellem, E., Bacon, R., et al. 2007, *MNRAS*, 379, 418
- Cole, S., Norberg, P., Baugh, C. M., et al. 2001, *MNRAS*, 326, 255
- Colina, L., Arribas, S., & Borne, K. D. 1999, *ApJ*, 527, L13
- Colina, L., Borne, K., Bushouse, H., et al. 2001, *ApJ*, 563, 546
- Colina, L., Arribas, S., & Clements, D. 2004, *ApJ*, 602, 181
- Colina, L., Arribas, S., & Monreal-Ibero, A. 2005, *ApJ*, 621, 725
- Combes, F., García-Burillo, S., Braine, J., et al. 2011, *A&A*, 528, A124
- da Cunha, E., Charmandaris, V., Díaz-Santos, T., et al. 2010, *A&A*, 523, A78
- Dasyra, K. M., Tacconi, L. J., Davies, R. I., et al. 2006a, *ApJ*, 638, 745
- Dasyra, K. M., Tacconi, L. J., Davies, R. I., et al. 2006b, *ApJ*, 651, 835
- Davies, R., Förster Schreiber, N. M., Cresci, G., et al. 2011, *ApJ*, 741, 69
- Downes, D., & Solomon, P. M. 1998, *ApJ*, 507, 615
- Elbaz, D., Hwang, H. S., Magnelli, B., et al. 2010, *A&A*, 518, L29
- Elbaz, D., Dickinson, M., Hwang, H. S., et al. 2011, *A&A*, 533, A119
- Epinat, B., Contini, T., Le Fèvre, O., et al. 2009, *A&A*, 504, 789
- Epinat, B., Amram, P., Balkowski, C., & Marcelin, M. 2010, *MNRAS*, 401, 2113
- Epinat, B., Tasca, L., Amram, P., et al. 2012, *A&A*, 539, A92
- Flores, H., Hammer, F., Puech, M., Amram, P., & Balkowski, C. 2006, *A&A*, 455, 107
- Förster Schreiber, N. M., Genzel, R., Bouché, N., et al. 2009, *ApJ*, 706, 1364
- García-Marín, M., Colina, L., Arribas, S., Alonso-Herrero, A., & Mediavilla, E. 2006, *ApJ*, 650, 850
- García-Marín, M., Colina, L., & Arribas, S. 2007, Ph.D. Thesis, Universidad Autónoma de Madrid, Spain
- García-Marín, M., Colina, L., Arribas, S., & Monreal-Ibero, A. 2009, *A&A*, 505, 1319
- Genzel, R., Tacconi, L. J., Rigopoulou, D., Lutz, D., & Tecza, M. 2001, *ApJ*, 563, 527
- Gonçalves, T. S., Basu-Zych, A., Overzier, R., et al. 2010, *ApJ*, 724, 1373
- Heckman, T. M., Armus, L., & Miley, G. K. 1990, *ApJS*, 74, 833
- Heckman, T. M., Hoopes, C. G., Seibert, M., et al. 2005, *ApJ*, 619, L35
- Hinz, J. L., & Rieke, G. H. 2006, *ApJ*, 646, 872
- James, P. A., Shane, N. S., Beckman, J. E., et al. 2004, *A&A*, 414, 23
- Kennicutt, Jr., R. C. 1998, *ApJ*, 498, 541
- Kennicutt, Jr., R. C., Tamblyn, P., & Congdon, C. E. 1994, *ApJ*, 435, 22
- Kim, D.-C., Veilleux, S., & Sanders, D. B. 2002, *ApJS*, 143, 277
- Krajnović, D., Cappellari, M., de Zeeuw, P. T., & Copin, Y. 2006, *MNRAS*, 366, 787
- Kroupa, P. 2008, in *Pathways Through an Eclectic Universe*, eds. J. H. Knapen, T. J. Mahoney, & A. Vazdekis, ASP Conf. Ser., 390, 3
- Lagache, G., Puget, J.-L., & Dole, H. 2005, *ARA&A*, 43, 727
- Law, D. R., Steidel, C. C., Erb, D. K., et al. 2007, *ApJ*, 669, 929
- Law, D. R., Steidel, C. C., Erb, D. K., et al. 2009, *ApJ*, 697, 2057
- Le Fèvre, O., Saisse, M., Mancini, D., et al. 2003, in *SPIE Conf. Ser.* 4841, eds. M. Iye, & A. F. M. Moorwood, 1670
- Le Floc'h, E., Papovich, C., Dole, H., et al. 2005, *ApJ*, 632, 169
- Lipari, S., Terlevich, R., Díaz, R. J., et al. 2003, *MNRAS*, 340, 289
- Maíz-Apellániz, J. 2004, *PASP*, 116, 859
- Monreal-Ibero, A., Arribas, S., & Colina, L. 2006, *ApJ*, 637, 138
- Monreal-Ibero, A., Arribas, S., Colina, L., et al. 2010, *A&A*, 517, A28
- Nordon, R., Lutz, D., Shao, L., et al. 2010, *A&A*, 518, L24
- Nordon, R., Lutz, D., Genzel, R., et al. 2012, *ApJ*, 745, 182
- Overzier, R. A., Heckman, T. M., Kauffmann, G., et al. 2008, *ApJ*, 677, 37
- Papovich, C., Rudnick, G., Le Floc'h, E., et al. 2007, *ApJ*, 668, 45
- Peng, C. Y., Ho, L. C., Impey, C. D., & Rix, H.-W. 2010, *AJ*, 139, 2097
- Pérez-González, P. G., Rieke, G. H., Egami, E., et al. 2005, *ApJ*, 630, 82
- Pérez-González, P. G., Rieke, G. H., Villar, V., et al. 2008, *ApJ*, 675, 234
- Piqueras López, J., Davies, R., Colina, L., & Orban de Xivry, G. 2012, *ApJ*, 752, 47
- Piqueras López, J., Colina, L., Arribas, S., & Alonso-Herrero, A. 2013, *A&A*, 553, A85
- Pope, A., Scott, D., Dickinson, M., et al. 2006, *MNRAS*, 370, 1185
- Puech, M., Hammer, F., Lehnert, M. D., & Flores, H. 2007, *A&A*, 466, 83
- Rodríguez Zaurín, J., Tadhunter, C. N., & González Delgado, R. M. 2010, *MNRAS*, 403, 1317
- Rodríguez-Zaurín, J., Arribas, S., Monreal-Ibero, A., et al. 2011, *A&A*, 527, A60
- Rothberg, B., & Fischer, J. 2010, *ApJ*, 712, 318
- Rothberg, B., Fischer, J., Rodríguez, M., & Sanders, D. B. 2013, *ApJ*, 767, 72
- Rupke, D. S. N., & Veilleux, S. 2013, *ApJ*, 768, 75
- Salpeter, E. E. 1955, *ApJ*, 121, 161
- Sanders, D. B., & Mirabel, I. F. 1996, *ARA&A*, 34, 749
- Sanders, D. B., Mazzarella, J. M., Kim, D.-C., Surace, J. A., & Soifer, B. T. 2003, *AJ*, 126, 1607
- Scoville, N. Z., Evans, A. S., Thompson, R., et al. 2000, *AJ*, 119, 991
- Shapiro, K. L., Genzel, R., Förster Schreiber, N. M., et al. 2008, *ApJ*, 682, 231
- Shapiro, K. L., Genzel, R., Quataert, E., et al. 2009, *ApJ*, 701, 955
- Shapiro, K. L., Falcón-Barroso, J., van de Ven, G., et al. 2010, *MNRAS*, 402, 2140
- Skrutskie, M. F., Cutri, R. M., Stiening, R., et al. 2006, *AJ*, 131, 1163
- Swinbank, A. M., Sobral, D., Smail, I., et al. 2012, *MNRAS*, 426, 935
- Tacconi, L. J., Genzel, R., Lutz, D., et al. 2002, *ApJ*, 580, 73
- Takagi, T., Ohya, Y., Goto, T., et al. 2010, *A&A*, 514, A5
- Taylor, E. N., Franx, M., Brinchmann, J., van der Wel, A., & van Dokkum, P. G. 2010, *ApJ*, 722, 1
- Tecza, M., Genzel, R., Tacconi, L. J., et al. 2000, *ApJ*, 537, 178
- U, V., Sanders, D. B., Mazzarella, J. M., et al. 2012, *ApJS*, 203, 9
- Veilleux, S., Kim, D.-C., & Sanders, D. B. 2002, *ApJS*, 143, 315
- Westmoquette, M. S., Clements, D. L., Bendo, G. J., & Khan, S. A. 2012, *MNRAS*, 424, A16
- Williams, M. J., Bureau, M., & Cappellari, M. 2010, *MNRAS*, 409, 1330
- Wolf, J., Martínez, G. D., Bullock, J. S., et al. 2010, *MNRAS*, 406, 1220
- Wright, E. L. 2006, *PASP*, 118, 1711
- Wu, H., Cao, C., Hao, C.-N., et al. 2005, *ApJ*, 632, L79
- Yun, M. S., Reddy, N. A., & Condon, J. J. 2001, *ApJ*, 554, 803

## Appendix A: Kinematic maps

In this Appendix we present the  $H\alpha$  flux, velocity field, and the velocity dispersion maps of the different kinematic components for the galaxies of the sample. When available, the HST image is also included. The spatial offsets between the peaks of the continuum and the  $H\alpha$  flux emission are shown in Table A.1.

### IRAS F01159–4443

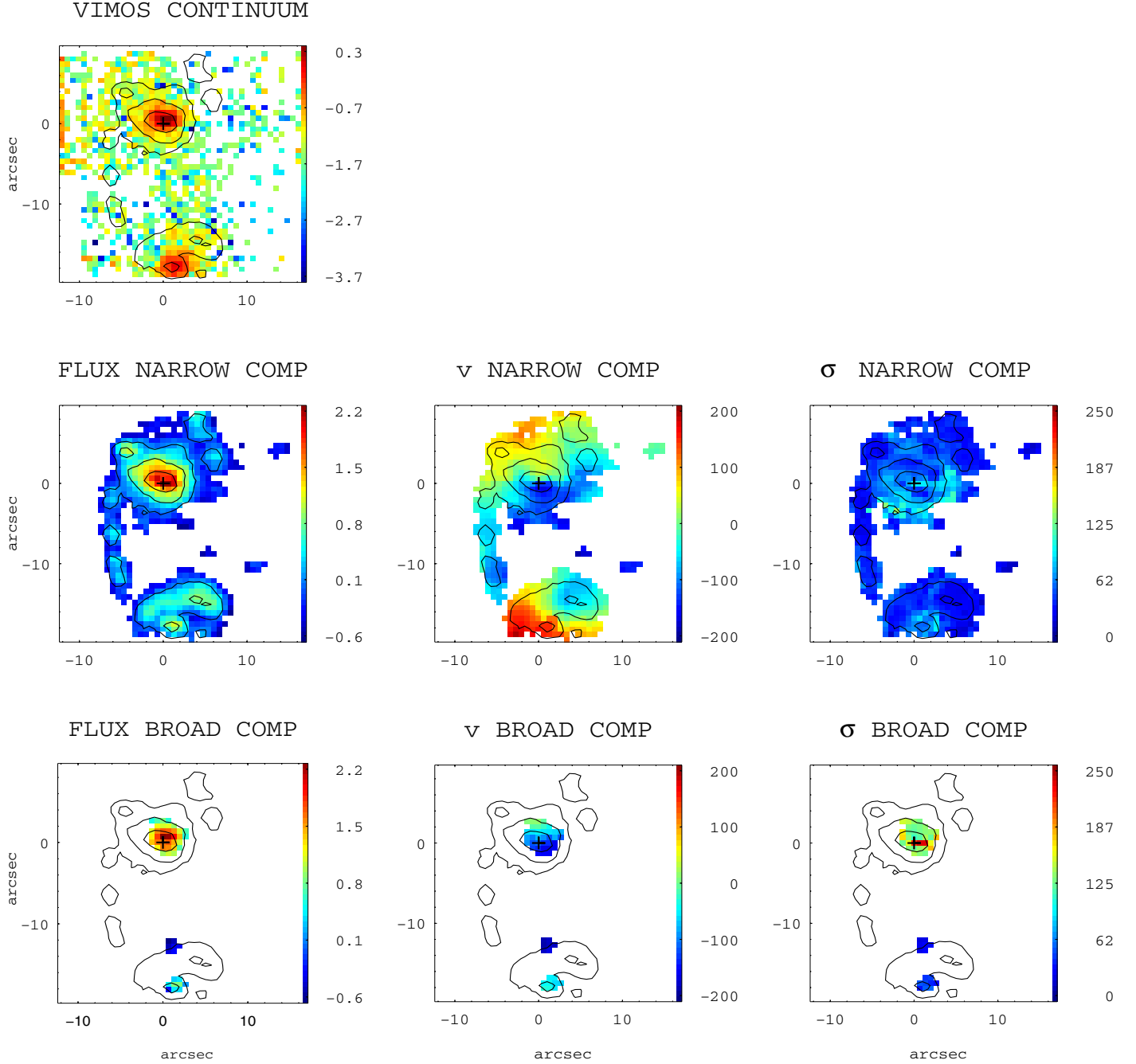


**Fig. A.1.** *Top panel:* VIMOS continuum (6390–6490) Å image within the rest-frame wavelength range. When available, the HST continuum image is also shown. *Middle panel:* the  $H\alpha$  flux intensity, velocity field,  $v$  (km s<sup>−1</sup>), and velocity dispersion,  $\sigma$  (km s<sup>−1</sup>), for the narrow component. *Bottom panel:* similar maps for the broad component. The flux intensity maps are represented in logarithmic scale (applying a factor of  $-13$ ) in units of erg s<sup>−1</sup> cm<sup>−2</sup> for the  $H\alpha$  flux maps and erg s<sup>−1</sup> cm<sup>−2</sup> Å<sup>−1</sup> for the continuum map. The center (0, 0) is identified with the  $H\alpha$  flux intensity peak and the iso-contours of the  $H\alpha$  flux map are overplotted. North is at the top and East to the left in all the panels.

IRAS F01159-4443 (ESO 244-G012): this is an interacting pair with a nuclear separation  $\sim 8.4$  kpc, where the northern galaxy shows the brightest nuclear emission in both the  $H\alpha$  and continuum maps. The two galaxies show regular velocity fields in the narrow component. The scale is 0.462 kpc/".



## IRAS F01341-3735 (ESO 297-G11)

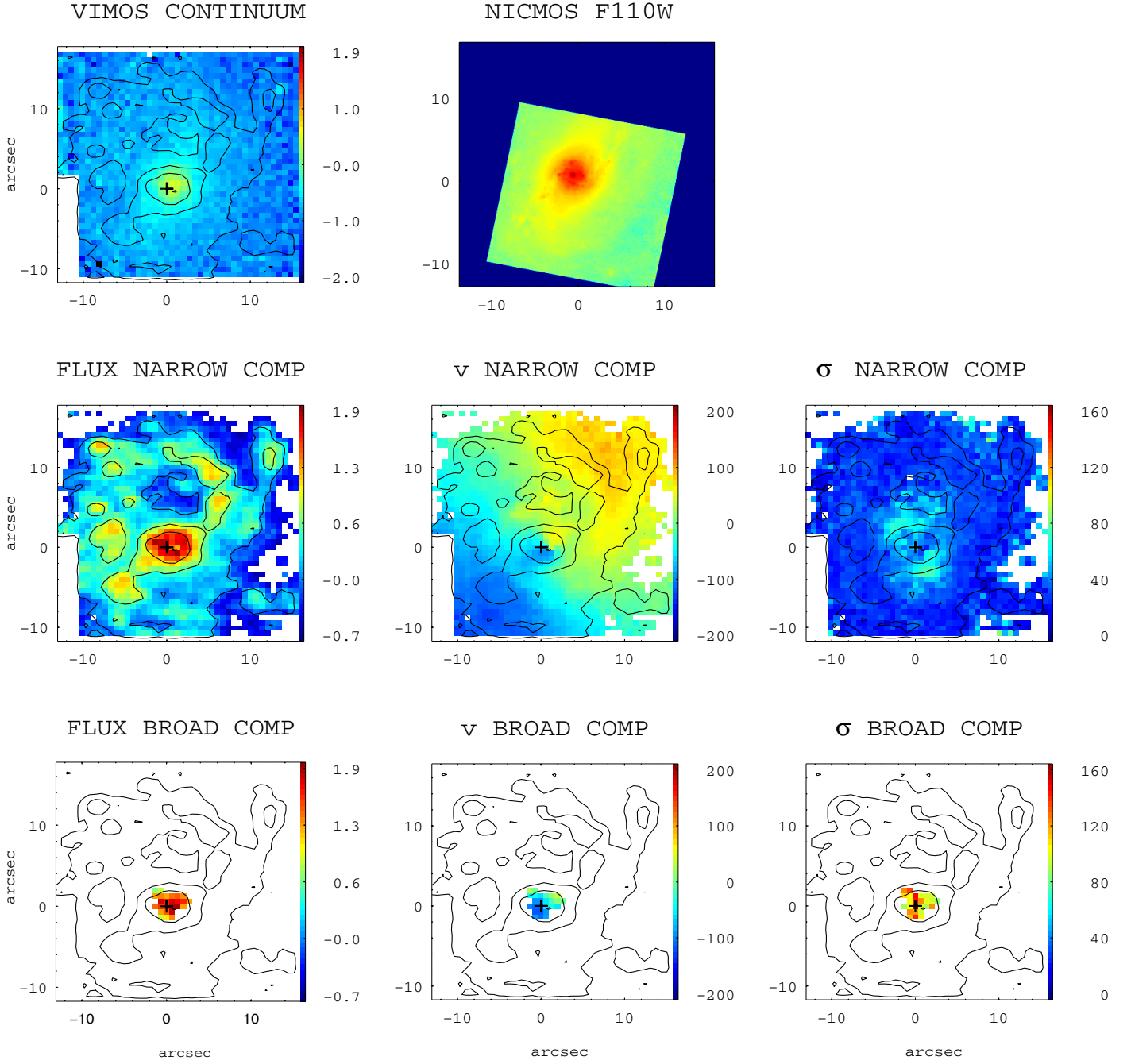


**Fig. A.2.** (General comments about the panels as in Fig. A.1.) IRAS F01341-3735 (ESO 297-G011/G012): this system is composed of two galaxies (i.e., northern, southern) separated by  $\sim 25$  kpc, implying the need of two VIMOS pointings. The present maps correspond to the northern galaxy, which shows a regular velocity field. The velocity dispersion map has two symmetric local maxima of  $\sim 70$  km s $^{-1}$  around the nucleus, which are well fitted using one Gaussian model. These regions have low H $\alpha$  surface brightness and are associated with high excitation and high  $\sigma$ , as reported by [Monreal-Ibero et al. \(2010\)](#). In the innermost regions (i.e.,  $\sim 1.5$  kpc $^2$ ), the H $\alpha$ -[NII] emission lines need a secondary broad component. The spatial scale is of 0.352 kpc $''$ .

## IRAS F01341-3735 (ESO 297-G12)

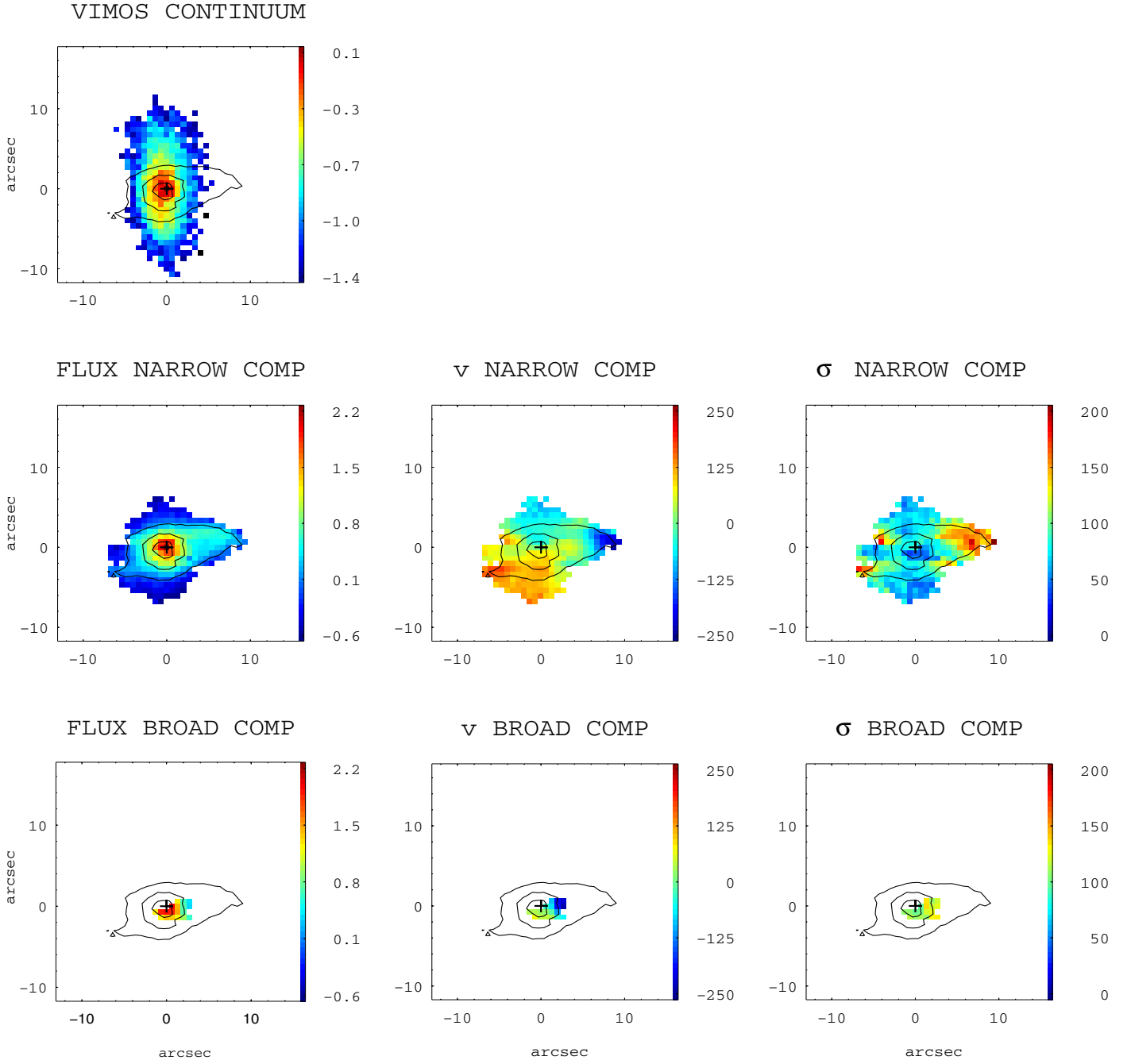


**Fig. A.3.** (General comments about the panels as in Fig. A.1.) ESO 297-G012: this is the southern galaxy of the system IRAS F01341-3735. The  $H\alpha$  emission is oriented perpendicular to the major stellar axis as traced by the continuum image. Although a rotation component is visible in the velocity field along the major photometrical axis, its structure, as well as that of the velocity dispersion map, is irregular. In an inner region ( $\sim 1 \text{ kpc}^2$ ), the spectra have been fitted with two components, with the broad component blueshifted by  $\sim 50 \text{ km s}^{-1}$ . The scale is  $0.352 \text{ kpc}''$ .

## IRAS F04315-0840

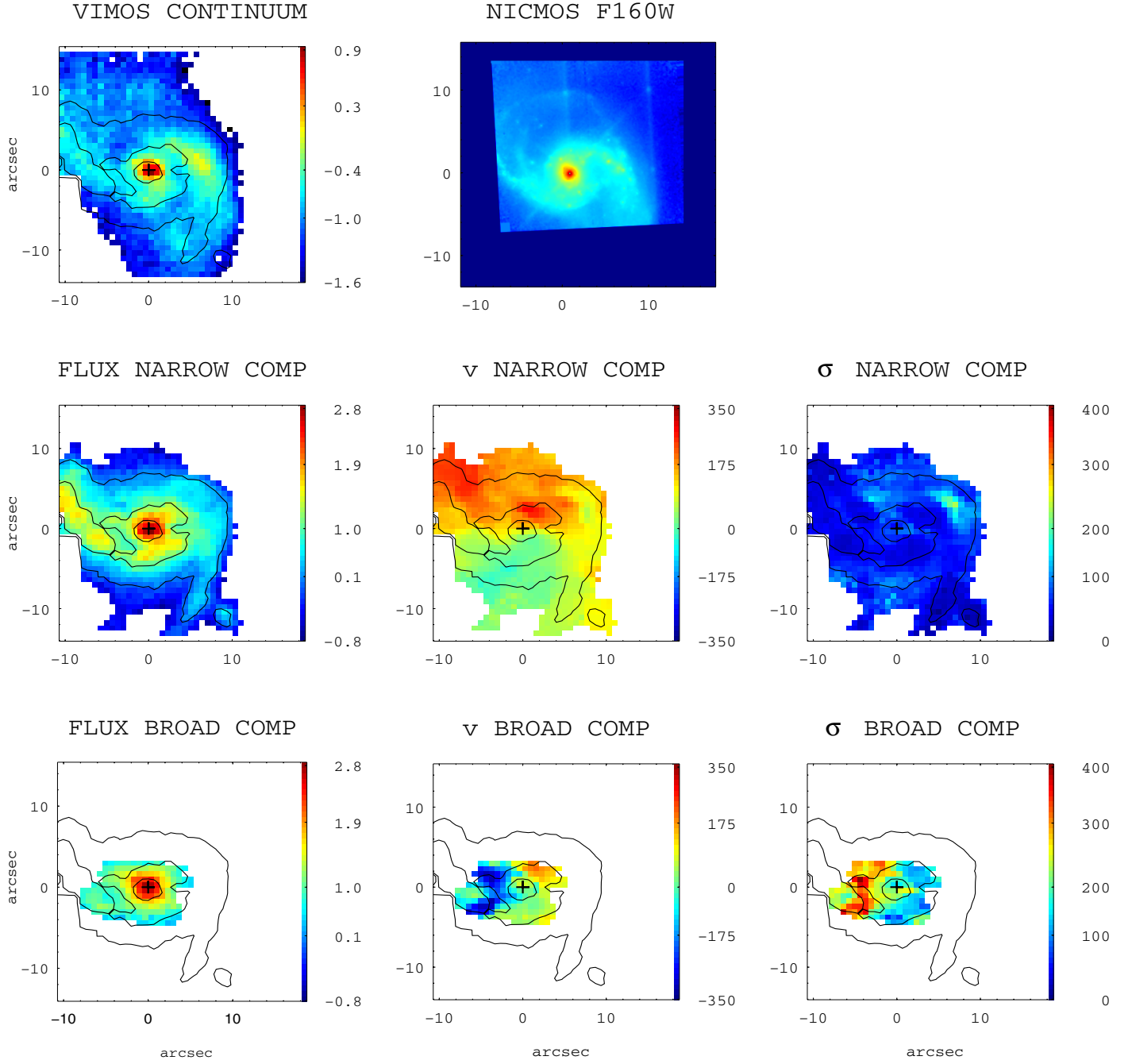


**Fig. A.4.** (General comments about the panels as in Fig. A.1.) IRAS F04315-0840 (NGC 1614): this is a well-studied, post-coalescence late merger, with a bright, spiral structure of a length scale of few kpc. The velocity field of the narrow component is somewhat distorted and chaotic with an amplitude of  $324 \text{ km s}^{-1}$ . Its velocity dispersion map shows an offset peak of  $\sim 220 \text{ km s}^{-1}$  at around 2.4 kpc from the nucleus in the western arm. The spectra in the inner regions are complex, and a secondary broad component covers a relatively large area of about  $8.6 \text{ kpc}^2$ . The projection of the kinematic major axes of the narrow (main) and broad components differs by  $\sim 90^\circ$ . The blueshifted region of the velocity field of the broad component has the largest velocity dispersion (i.e.,  $\sim 400 \text{ km s}^{-1}$ ). All this supports the hypothesis of a dusty outflow, where the receding components (which are behind the disk) are obscured, making the whole profile relatively narrow with respect to the approaching component. This object has been analyzed in [Bellocchi et al. \(2012\)](#). The spatial scale is  $0.325 \text{ kpc}''$ .



## IRAS F05189-2524

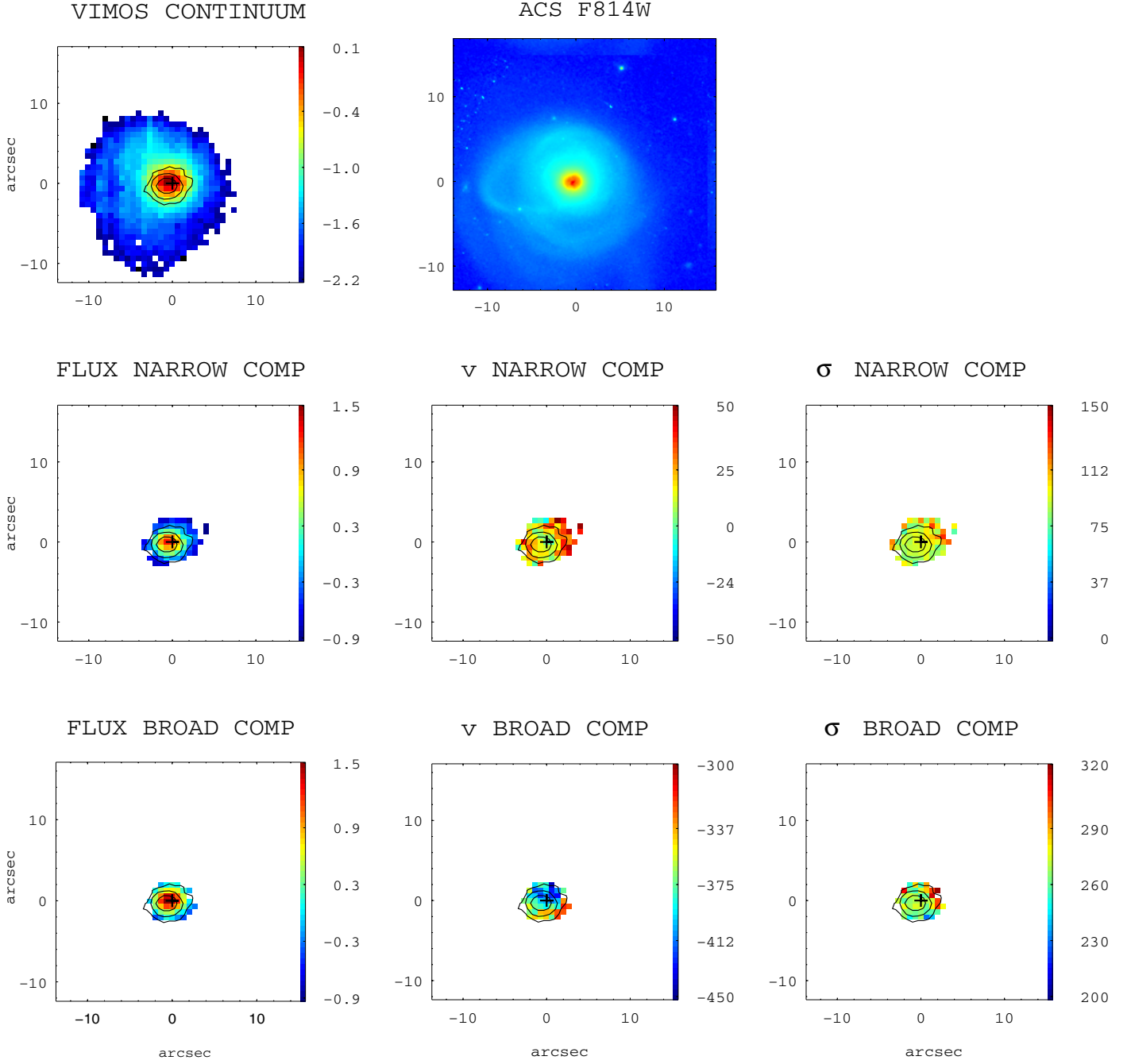


**Fig. A.5.** (General comments about the panels as in Fig. A.1.) IRAS F05189-2524: this galaxy shows a compact  $H\alpha$  emission, both in the narrow and broad components. Their velocity fields and velocity dispersion maps do not show regular patterns. The broad component is blueshifted up to  $\sim 400 \text{ km s}^{-1}$  with respect to the narrow one and is dominant in terms of flux in the innermost spaxels. The scale is of  $0.839 \text{ kpc}''$ .

## IRAS F06035-7102

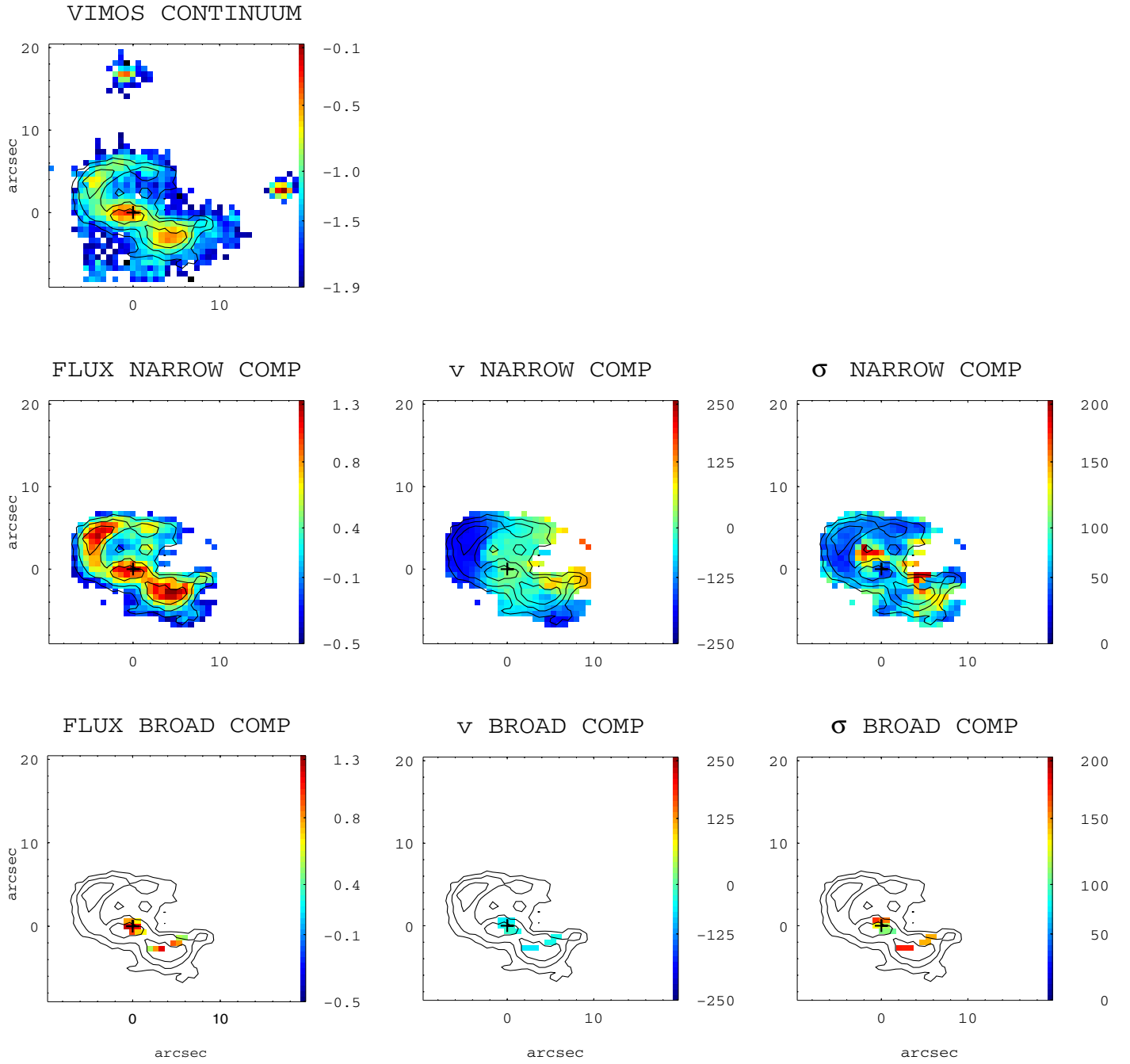


**Fig. A.6.** (General comments about the panels as in Fig. A.1.) IRAS F06035-7102: this system consists of two pre-coalescence galaxies with a nuclear separation of  $\sim 8$  kpc. The velocity dispersion map of the narrow component clearly shows an irregular pattern, in which the two local maxima correspond to low  $H\alpha$  surface brightness regions. The spatial scale is  $1.5 \text{ kpc}''$ .

## IRAS F06076-2139

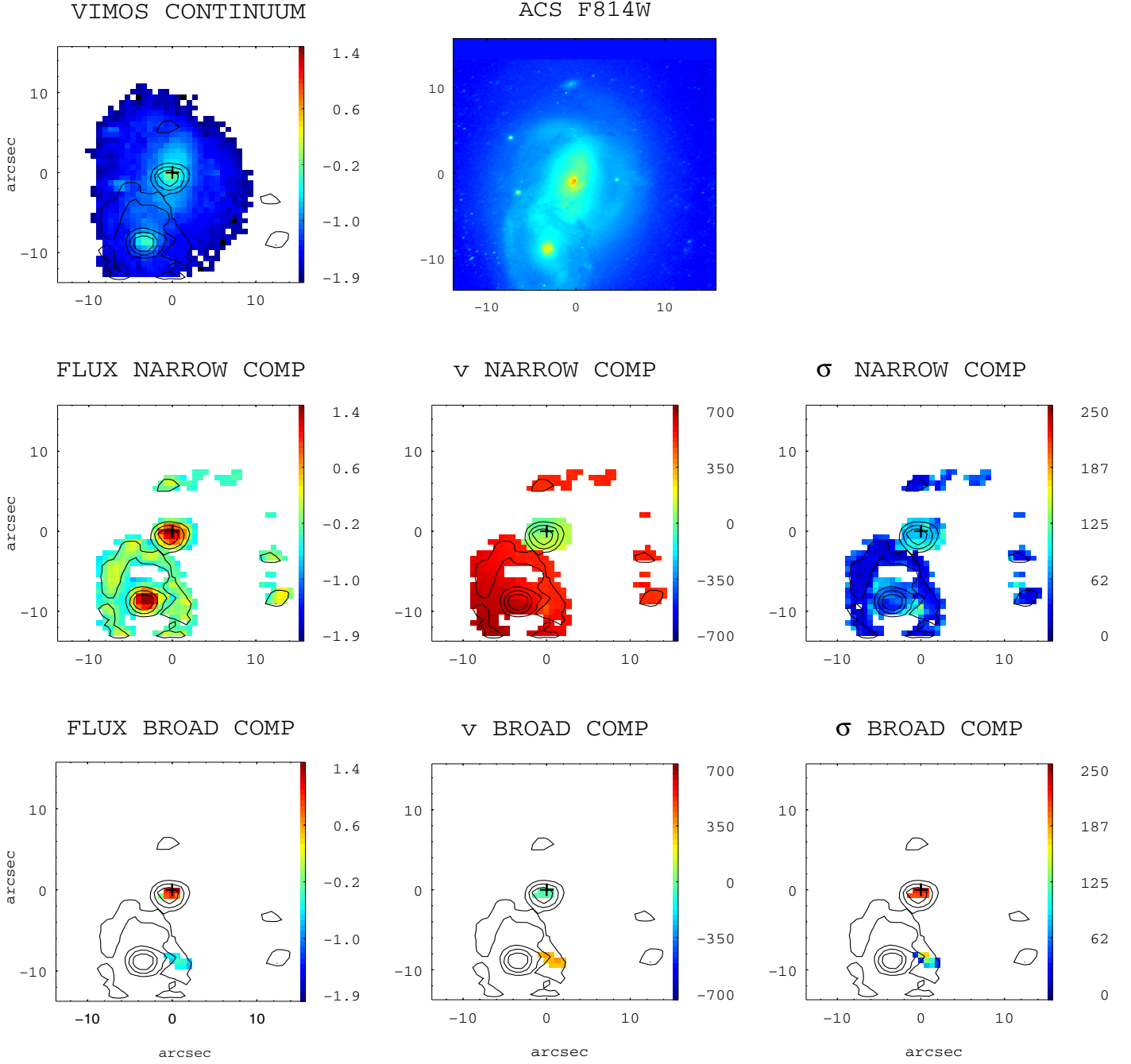


**Fig. A.7.** (General comments about the panels as in Fig. A.1.) IRAS F06076-2139: this system consists of two galaxies in interaction with a rather complex morphology. The  $H\alpha$  image shows a rather different structure than that shown by the VIMOS continuum and the HST-ACS image. The southern galaxy is characterized by a ring and a tidal tail-like structures extending towards the west and northwest part from the nucleus. The faint broad component found in a small region of the ring in the southern object is likely due to the superposition of the emission of the two galaxies along the line-of-sight. This system was already studied in [Arribas et al. \(2008\)](#). The scale is 0.743 kpc''.



## IRAS F06206-6315

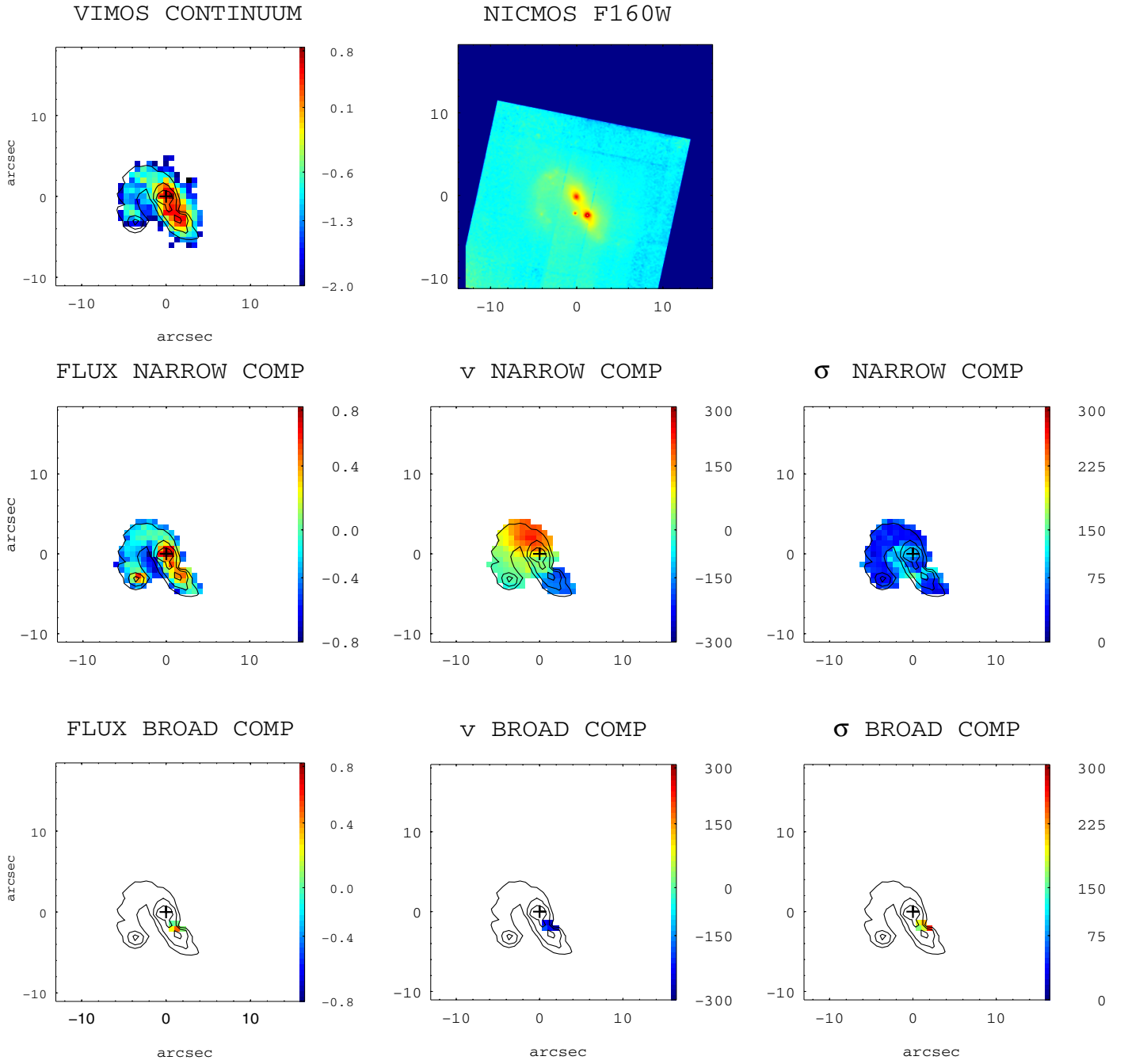


**Fig. A.8.** (General comments about the panels as in Fig. A.1.) IRAS F06206-6315: this system has a double nuclei separated by  $\sim 4$  kpc, as clearly seen in the the Near Infrared Camera and Multi-Object Spectrometer (NICMOS/HST) image. There is a tidal tail starting in the north and bending towards the southeast, which contains a local peak of  $H\alpha$  emission (i.e., a possible tidal dwarf galaxy candidate). The brightest nucleus seems to be in positional agreement with the kinematic center. The velocity field is regular, and most of the spectra are well fitted using one component. The scale is of  $1.72$  kpc''.

## IRAS F06259-4708 (North)

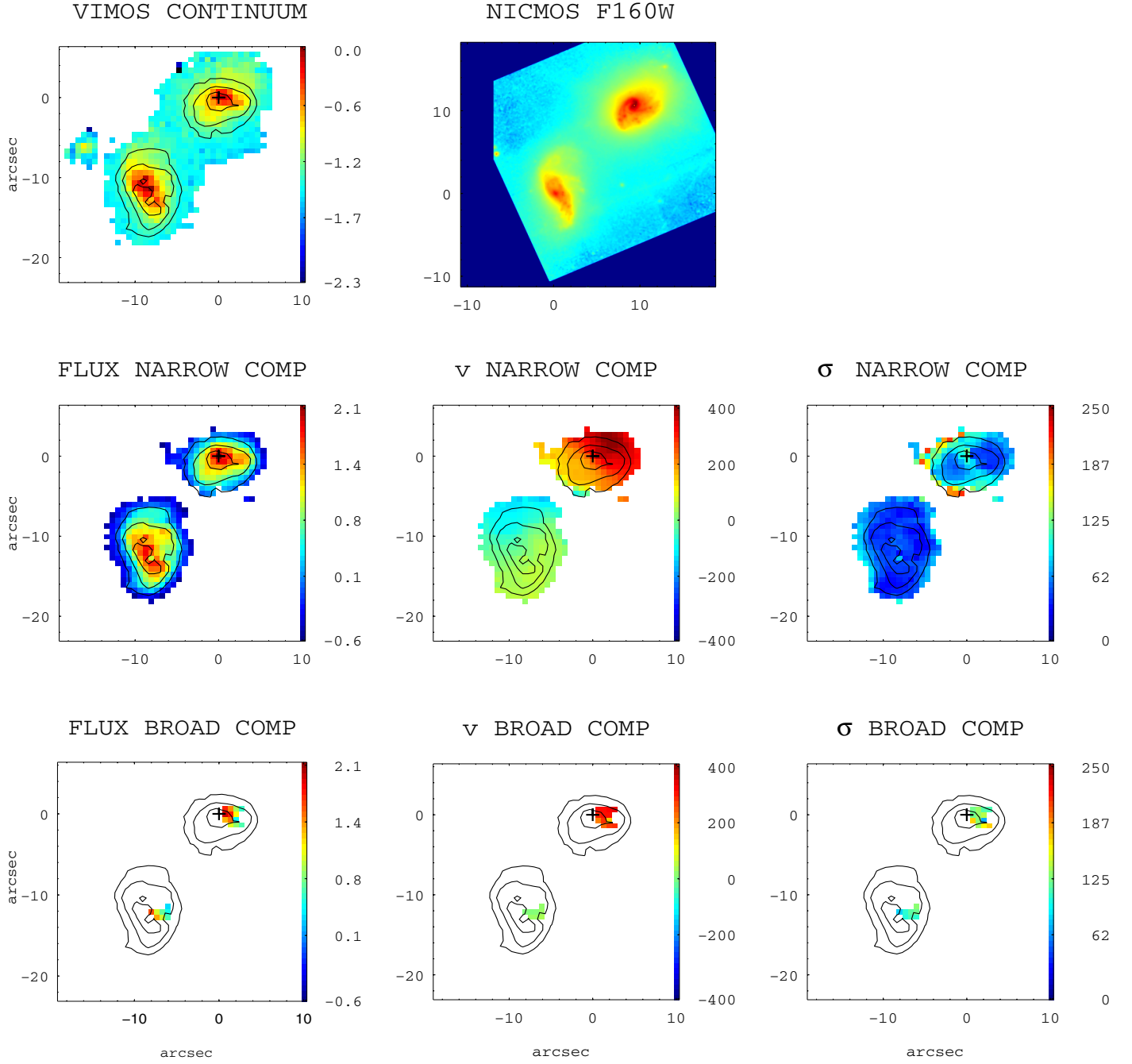


**Fig. A.9.** (General comments about the panels as in Fig. A.1.) IRAS F06259-4708 (ESO 255-IG007): two VIMOS pointings were used during the observation of this triple system. The two brightest galaxies, the northern and the central ones, are separated by a distance of  $\sim 11$  kpc, while the third one is located at  $\sim 13$  kpc to the south from the central galaxy (see next panel). The present panels correspond to the northern and central galaxies, which show a regular velocity field pattern. The scale is of  $0.769$  kpc $''$ .

## IRAS F06259–4708 (South)

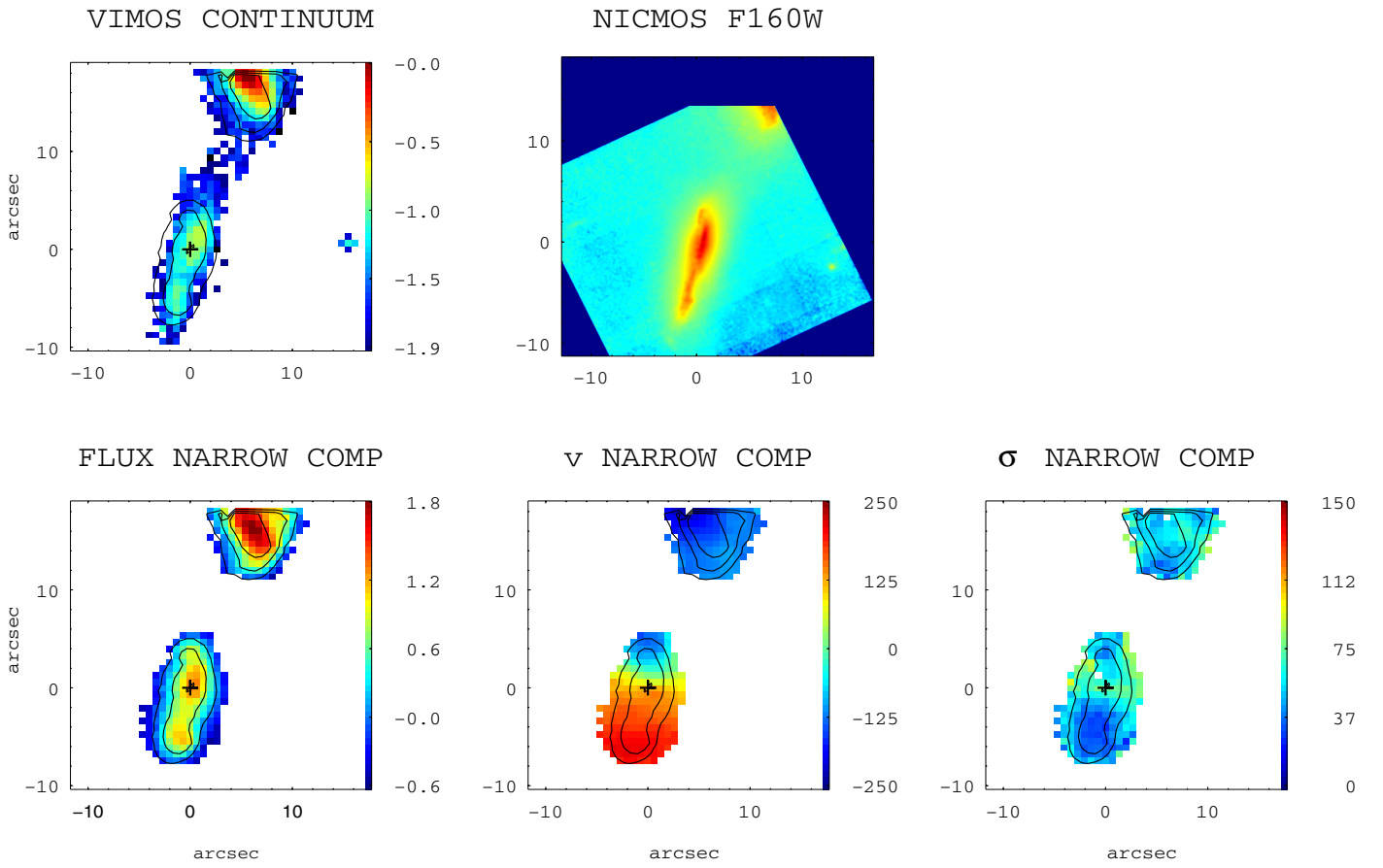


**Fig. A.10.** (General comments about the panels as in Fig. A.1.) ESO 255-IG007: this is the southern galaxy of the system IRAS F06259-4708. It has a regular velocity field and the velocity dispersion map. One single Gaussian component is adequate to fit the  $H\alpha$ -[NII] emission lines of this galaxy. The scale is  $0.769 \text{ kpc}''$ .



## IRAS F06295-1735

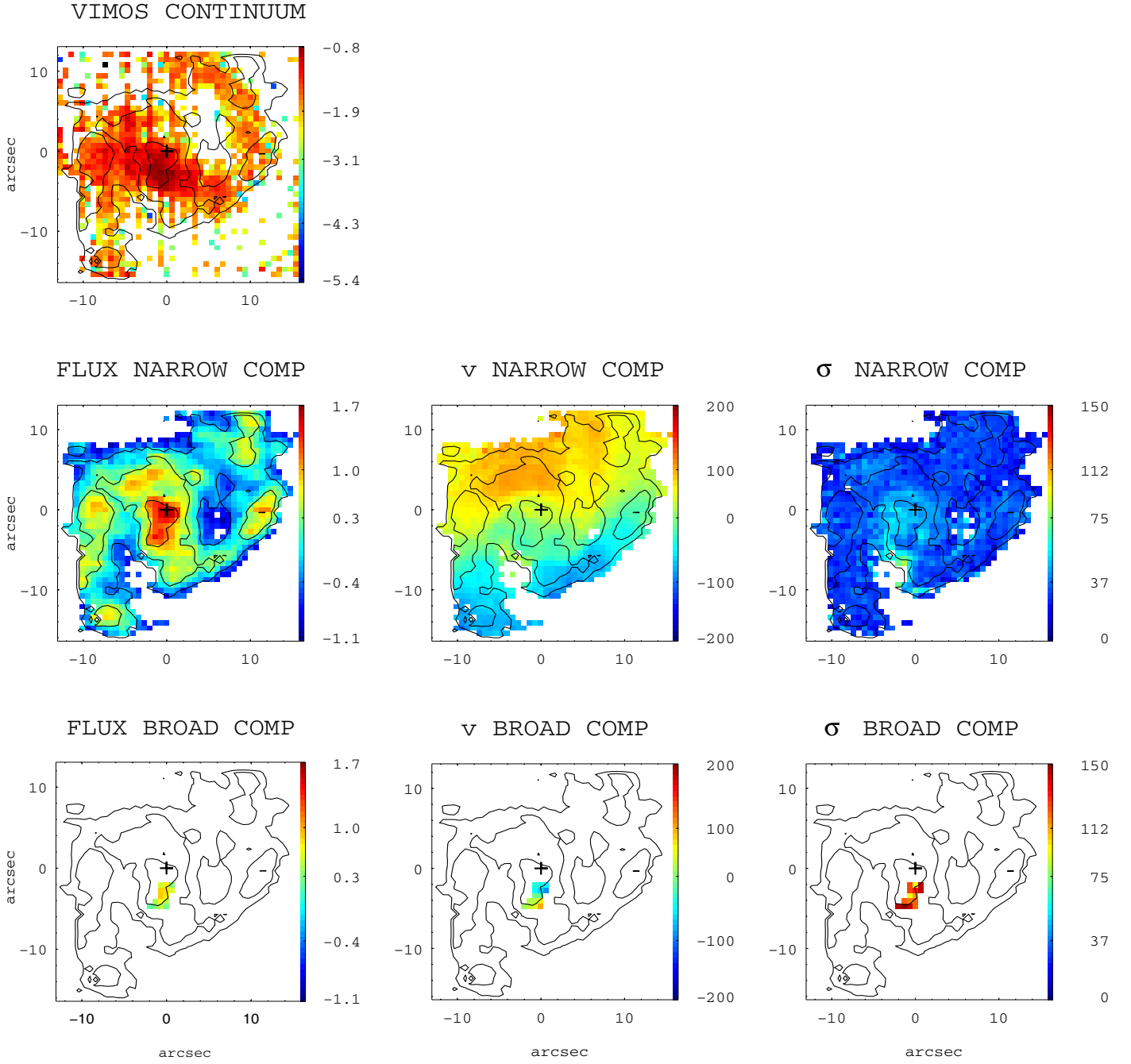


**Fig. A.11.** (General comments about the panels as in Fig. A.1.) IRAS F06295-1735 (ESO 557-G002): the continuum image of this barred spiral shows vertical strips, which were not possible to remove during the reduction process (see [Rodríguez-Zaurín et al. 2011](#)). However, the  $H\alpha$  maps are not affected by this problem. Interestingly, neither the arms nor the bar in the  $H\alpha$  image coincide with those in the continuum image. The velocity field shows a regular structure, while its velocity dispersion map reaches the highest values (i.e.,  $\sigma \sim 70\text{--}80\text{ km s}^{-1}$ ) at about 2 kpc to the south of the nucleus, in a region of relatively low emission. The scale is of  $0.431\text{ kpc}''$ .

## IRAS F06592-6313

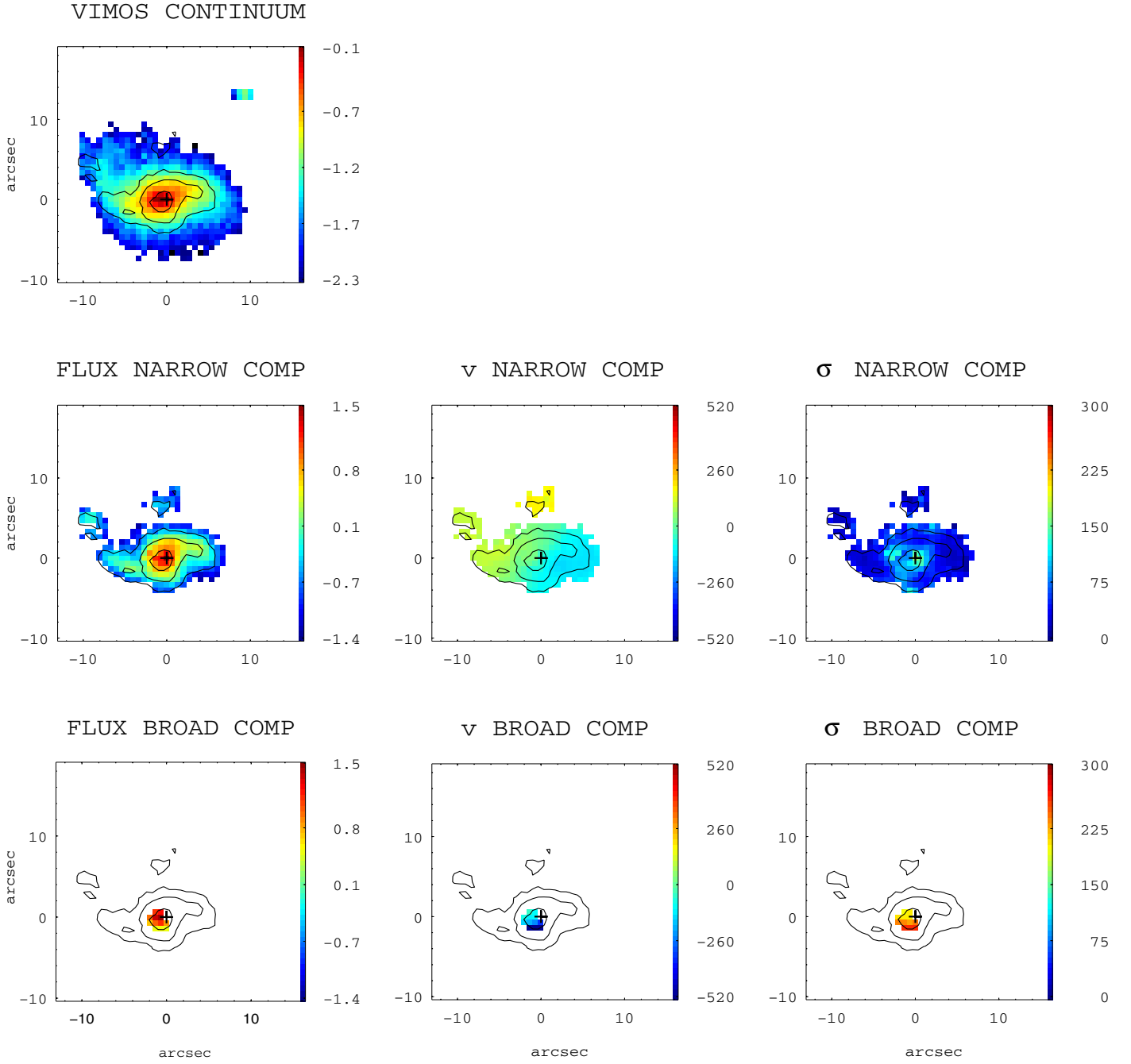


**Fig. A.12.** (General comments about the panels as in Fig. A.1.) IRAS 06592-6313: this spiral galaxy shows a minor kinematic axis not aligned with the corresponding photometric one. Its velocity field shows a regular pattern with an amplitude of  $160 \text{ km s}^{-1}$ , while the velocity dispersion map shows some structure around the nucleus. A broad component blueshifted up to  $\sim 300 \text{ km s}^{-1}$  has been found in the inner regions. The scale is of  $0.464 \text{ kpc''}$ .

## IRAS F07027-6011 (North)

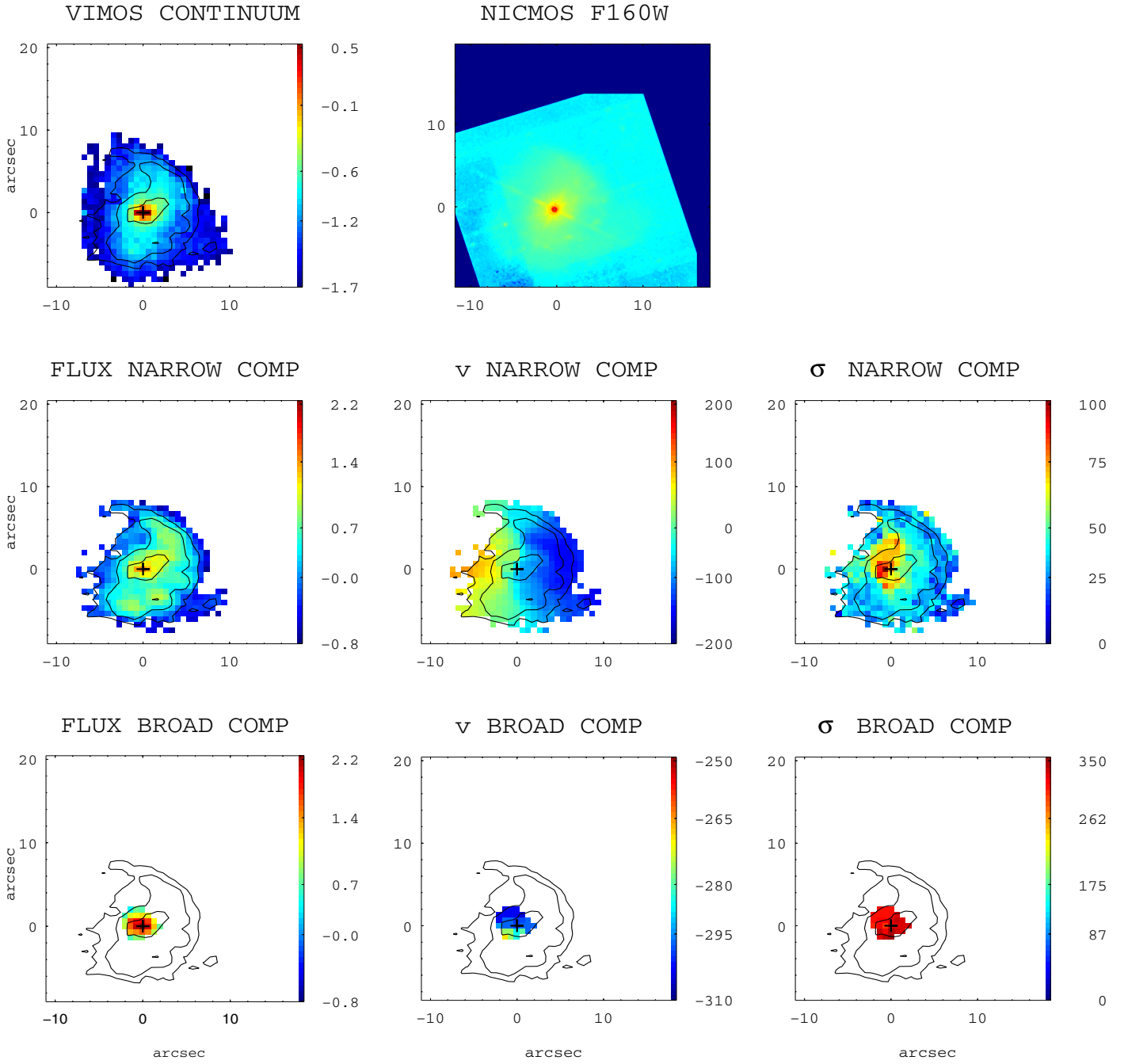


**Fig. A.13.** (General comments about the panels as in Fig. A.1.) IRAS F07027-6011 (AM 0702-601): this system consists of two galaxies separated by  $\sim 54$  kpc. The present maps correspond to the northern galaxy. This object has a regular velocity field, while the velocity dispersion map shows a local maximum offset by  $\sim 0.4$  kpc with respect to the nucleus (or  $H\alpha$  flux peak). The secondary component found in the inner part shows a  $\sigma_{\text{mean}}$  of about  $320 \text{ km s}^{-1}$ , which can be explained by the fact that this galaxy possibly hosts an AGN (see [Arribas et al. 2012](#)). The spatial scale is of  $0.626 \text{ kpc}''$ .



## IRAS F07027-6011 (South)

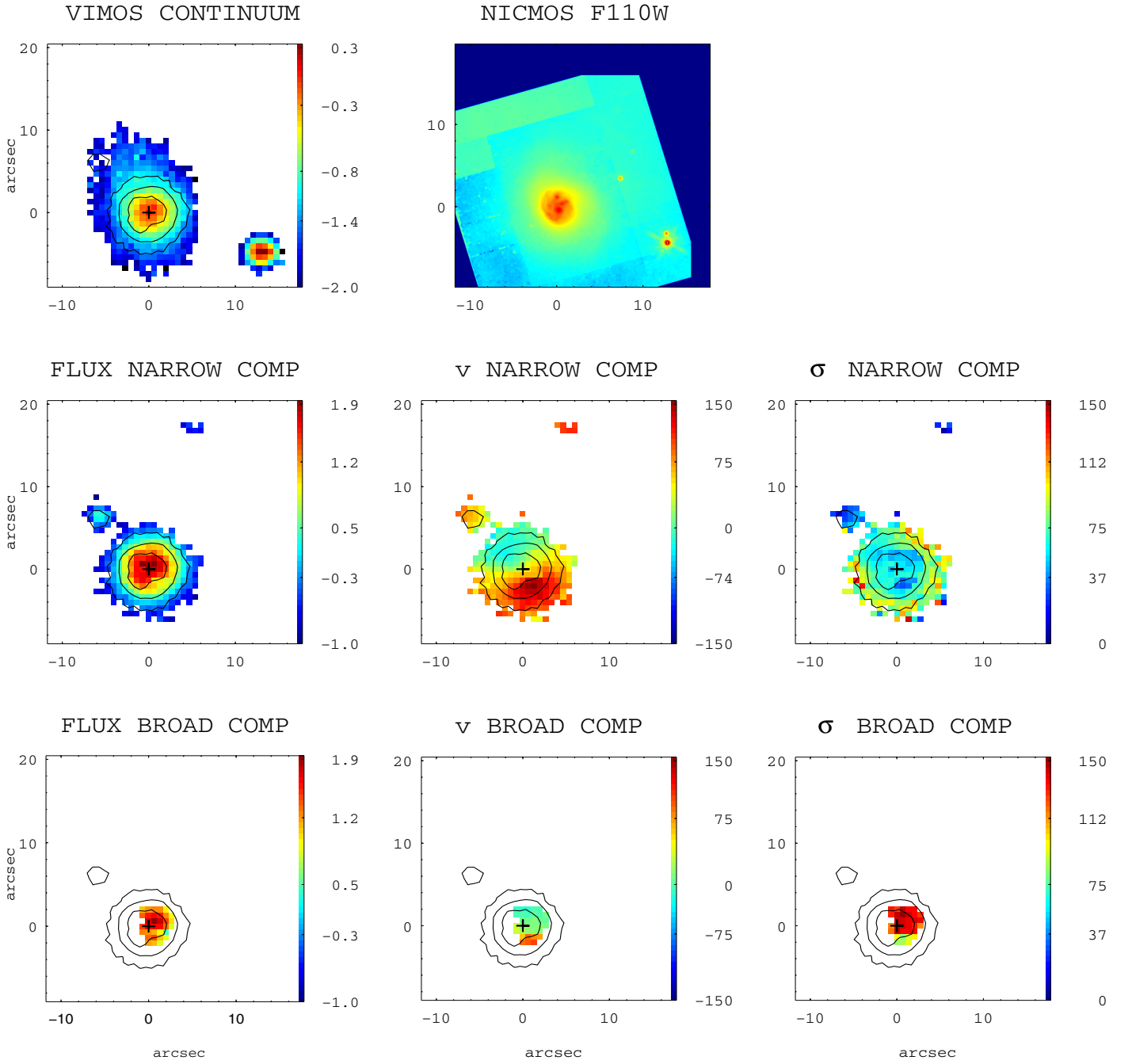


**Fig. A.14.** (General comments about the panels as in Fig. A.1.) IRAS F07027-6011 (AM 0702-601): these maps correspond to the southern galaxy of the system. The velocity field of the narrow component is rather regular. In the velocity dispersion map a local maximum is found in correspondence of the nucleus (or H $\alpha$  peak). The spatial scale is of 0.626 kpc''.

## IRAS F07160-6215

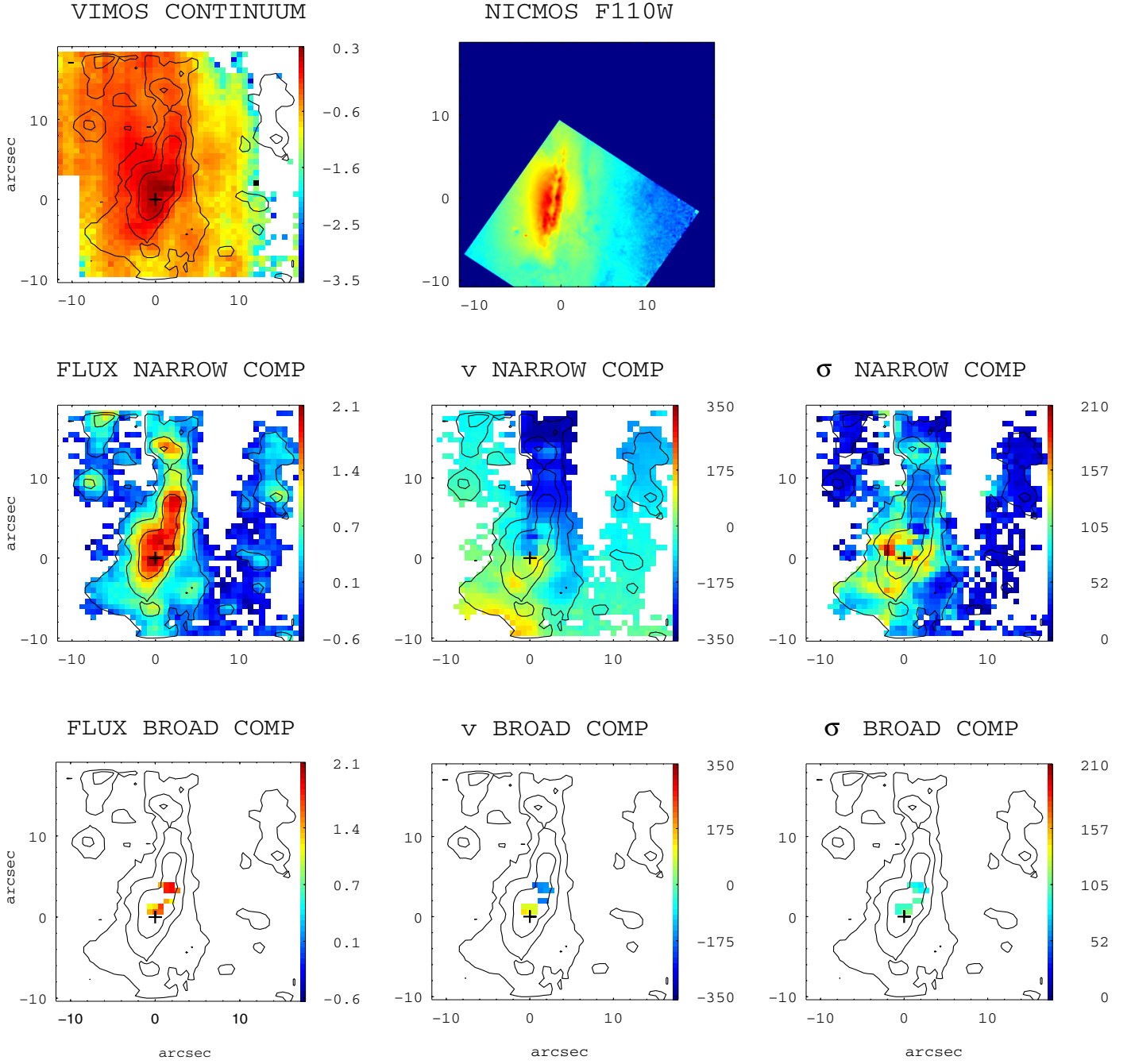


**Fig. A.15.** (General comments about the panels as in Fig. A.1.) IRAS F07160-6215 (NGC 2369): this is an edge-on dusty galaxy, whose structure could strongly affect the pattern of its velocity field and velocity dispersion map. Indeed, the velocity field has a clear rotation component with some irregularities, and the velocity dispersion map shows distorted inner ( $\sim 1$  kpc) regions, with values ranging between 120 and 200  $\text{km s}^{-1}$ , where a broad component has been considered to properly fit the spectra. The scale is 0.221 kpc $''$ .

## IRAS 08355-4944

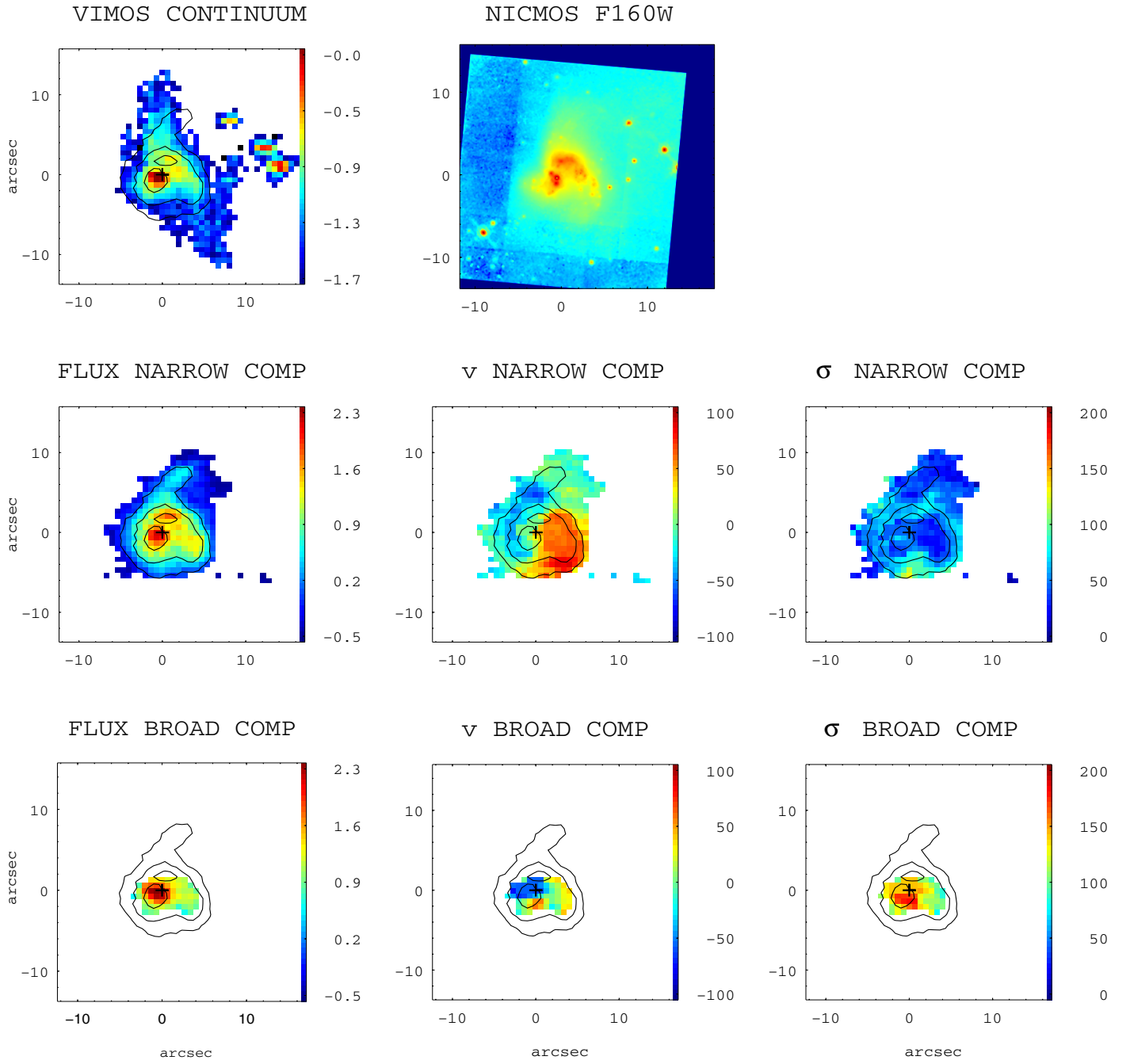


**Fig. A.16.** (General comments about the panels as in Fig. A.1.) IRAS 08355-4944: this galaxy is morphologically classified as a post-coalescence merger. It has a quite regular velocity pattern and a relatively disturbed structure in the velocity dispersion map. Most of the spectra in the inner region have been fitted applying 2-Gaussian fit. The spatial scale is 0.521 kpc''.

## IRAS 08424-3130

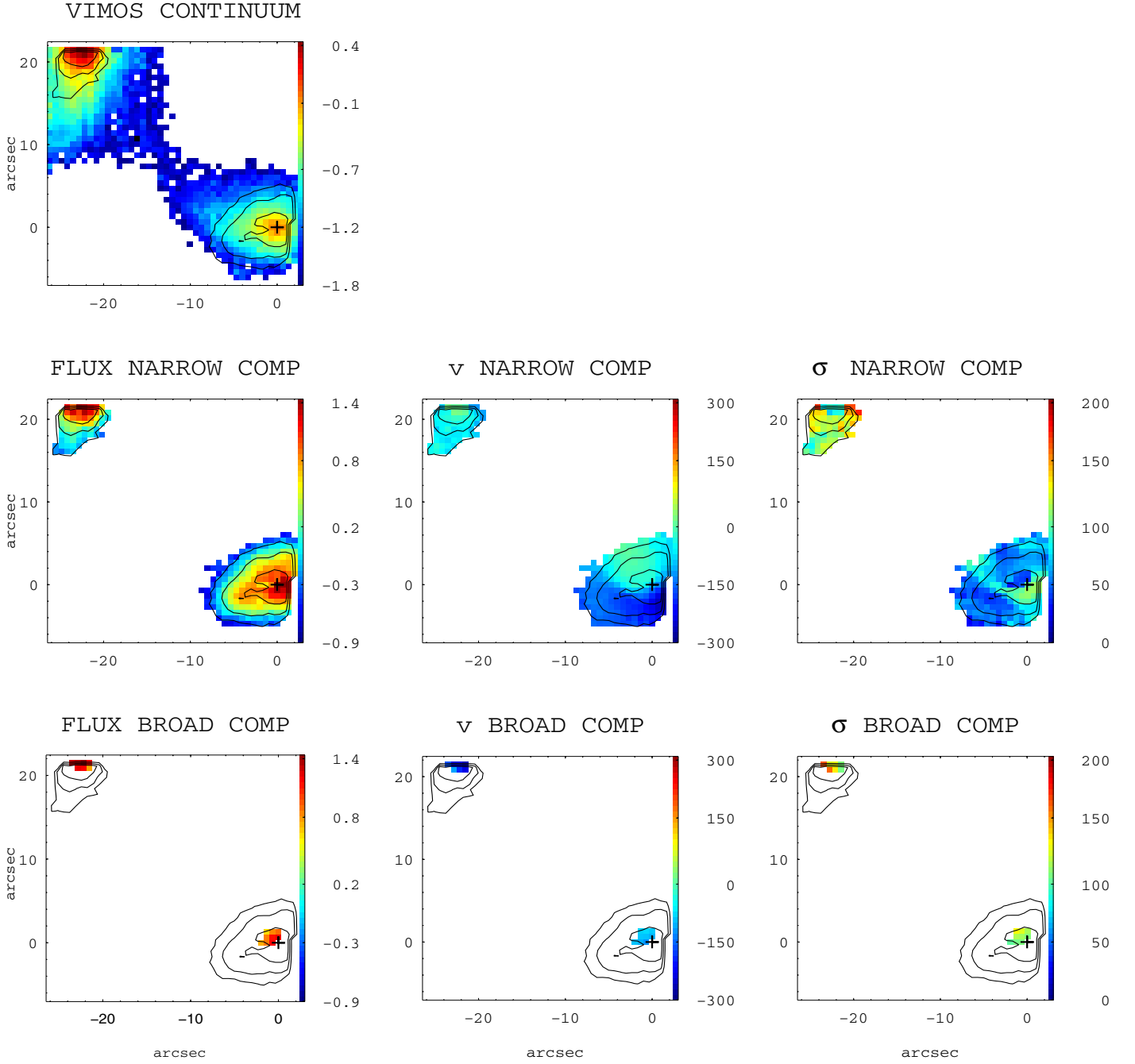


**Fig. A.17.** (General comments about the panels as in Fig. A.1.) IRAS 08424-3130 (ESO 432-IG006): the Digital Sky Survey (DSS) image shows a pair of spiral galaxies (nuclear separation of  $\sim 9$  kpc) in interaction. Only part of the nuclear region of both galaxies is covered by our VIMOS FoV. The area covered by the  $H\alpha$  emission line for the northern galaxy is very small, so that its kinematical classification was not possible. The southern object reveals a relatively regular velocity field with an amplitude of  $133 \text{ km s}^{-1}$  and an almost centrally peaked velocity dispersion map. The spatial scale is  $0.329 \text{ kpc}''$ .



## IRAS F08520-6850

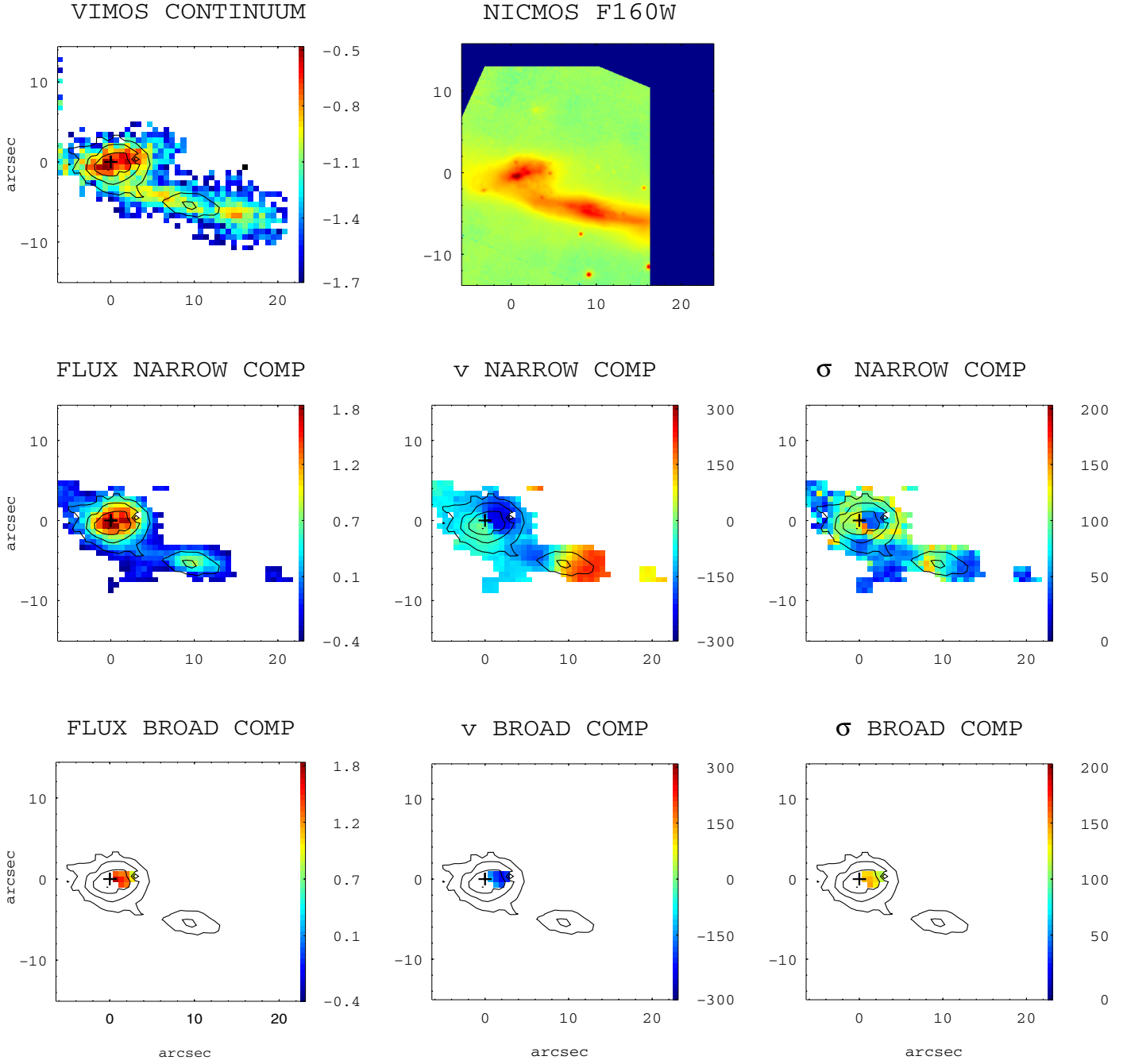


**Fig. A.18.** (General comments about the panels as in Fig. A.1.) IRAS F08520-6850 (ESO 60-IG016): this system is composed of two disk galaxies in interaction with a nuclear separation of 10 kpc. The  $H\alpha$  flux peak and the kinematic center of the eastern source are in positional agreement. The velocity fields of the respective galaxies are regular. The spatial scale is 0.909 kpc''.

## IRAS 09022-3615

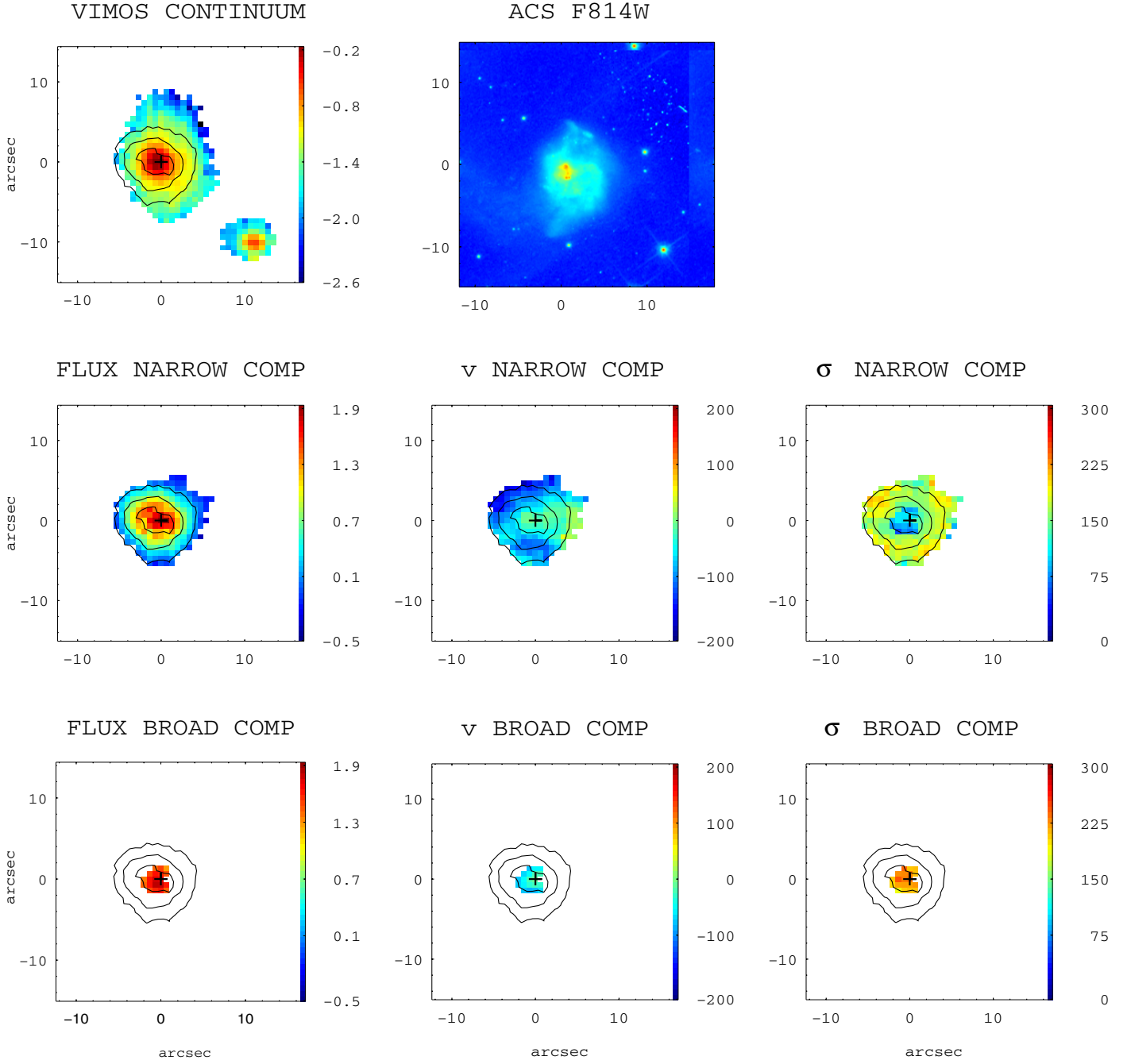


**Fig. A.19.** (General comments about the panels as in Fig. A.1.) IRAS F09022-3615: the velocity field is quite distorted and irregular with poorly defined kinematic axes. The ring of high-velocity dispersion around the nucleus has several local peaks. A broad component is present in the inner parts. The spatial scale is of 1.153 kpc $''$ .

## IRAS F09437+0317 (IC 564)

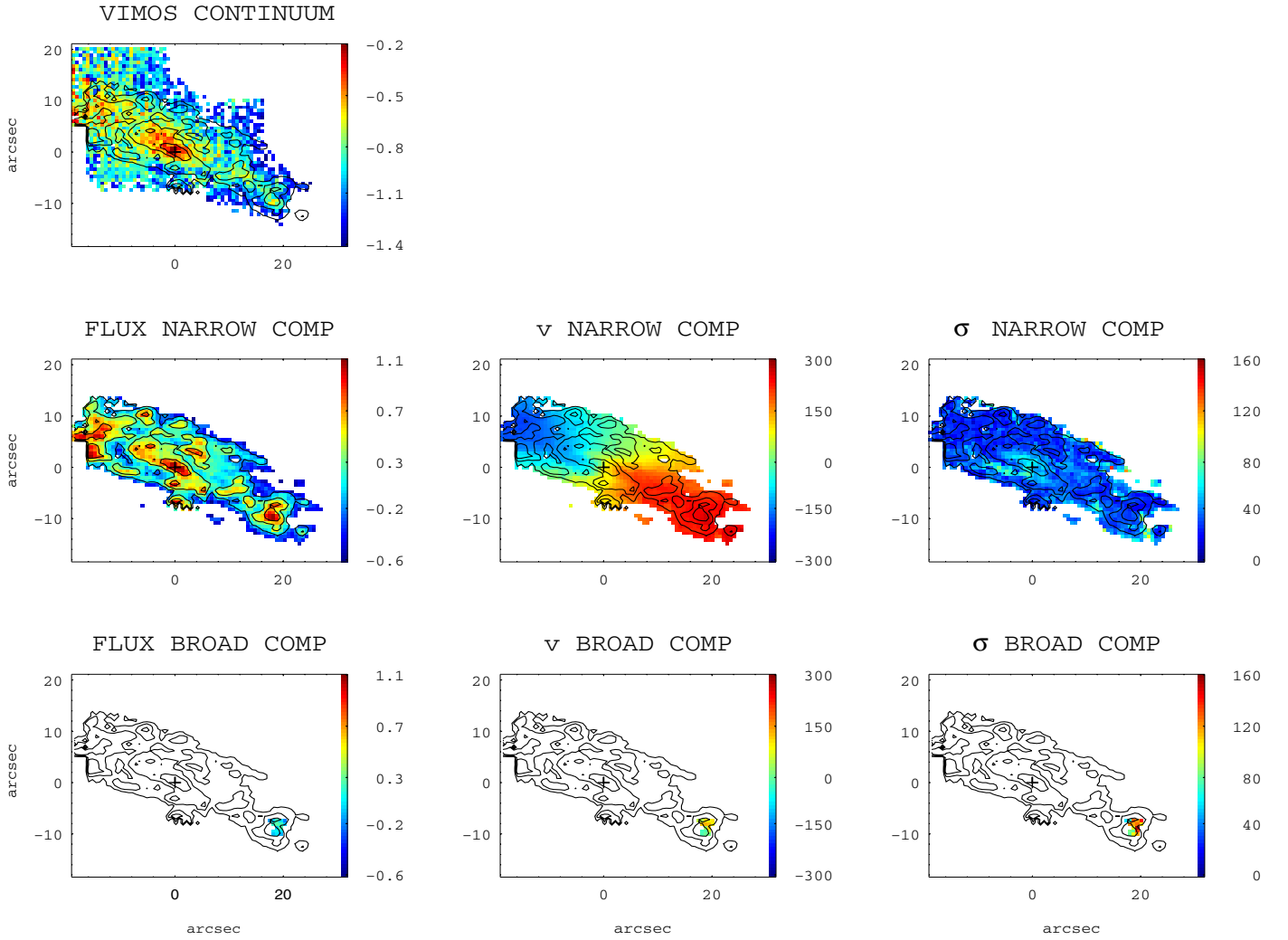


**Fig. A.20.** (General comments about the panels as in Fig. A.1.) IRAS F09437+0317 (IC 564/IC 563): this system is formed by two galaxies (north: IC 564/ south: IC 563) with a nuclear separation of about 39 kpc. Three VIMOS pointings were carried out for observing this system. For the northern galaxy (IC 564), two pointings sample the northeast (NE) and the southwest (SW) parts of the galaxy (see Fig.1 Paper III); both of them have been used to derived the mean kinematic values (Table 4). These panels (i.e.,  $\sim 50'' \times 40''$ ) were generated by combining the NE and NW pointings. A faint broad component was found in correspondence of an offset  $H\alpha$  peak in the SW direction, possibly due to the presence of a star-forming region. The velocity field is regular, and the kinematic center seems to be in positional agreement with the continuum and  $H\alpha$  flux peaks. The spatial scale is  $0.415 \text{ kpc}''$ .

## IRAS F09437+0317 (IC 563)

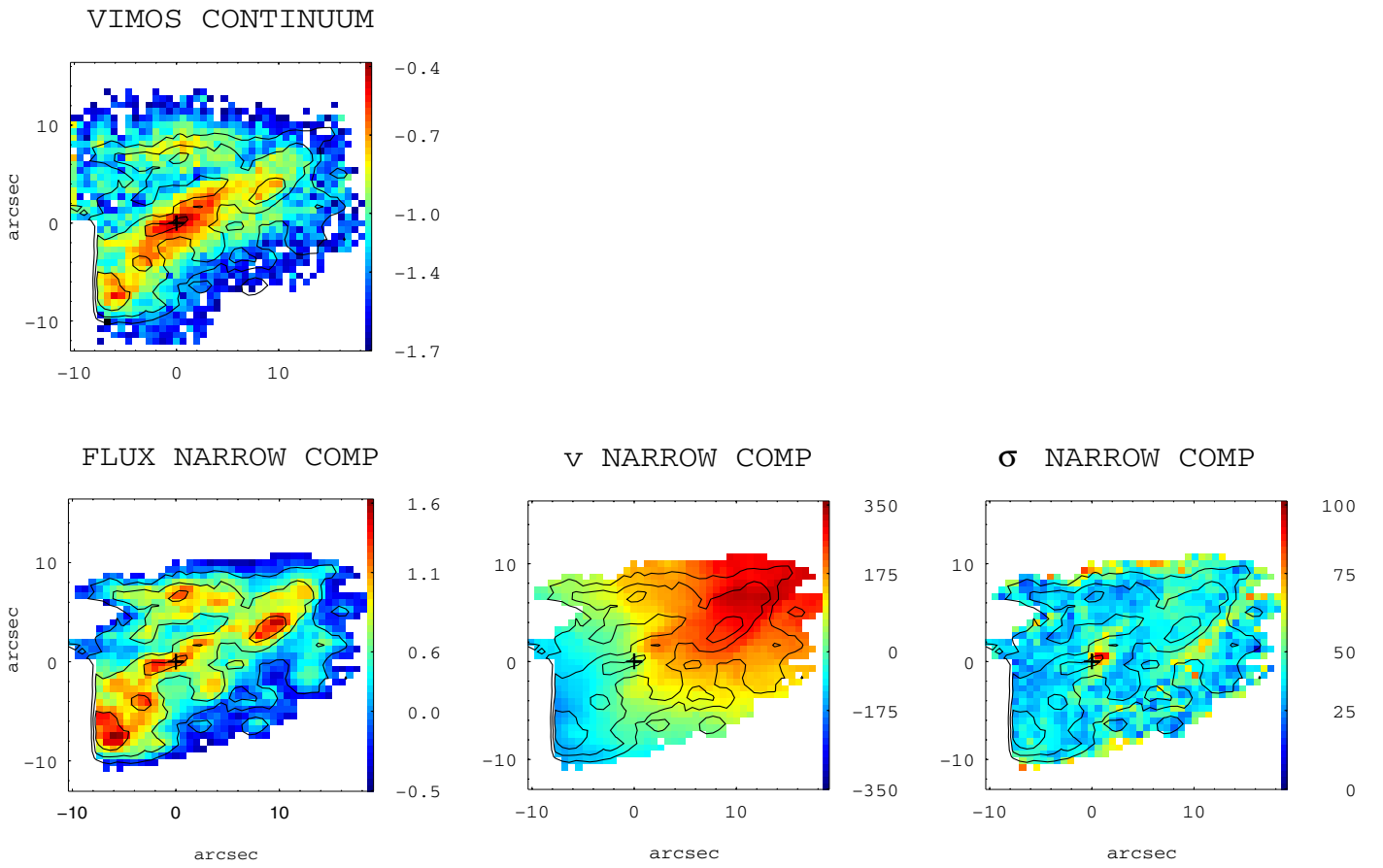


**Fig. A.21.** (General comments about the panels as in Fig. A.1.) IRAS F09437+0317 (IC 563): this object shows a very regular velocity field and a centrally peaked velocity dispersion map. The VIMOS continuum image is considered the center of the image since the  $H\alpha$  peak is offset due to a knot of star formation and does not properly define the center. The spatial scale is  $0.415 \text{ kpc}''$ .



## IRAS F10015-0614

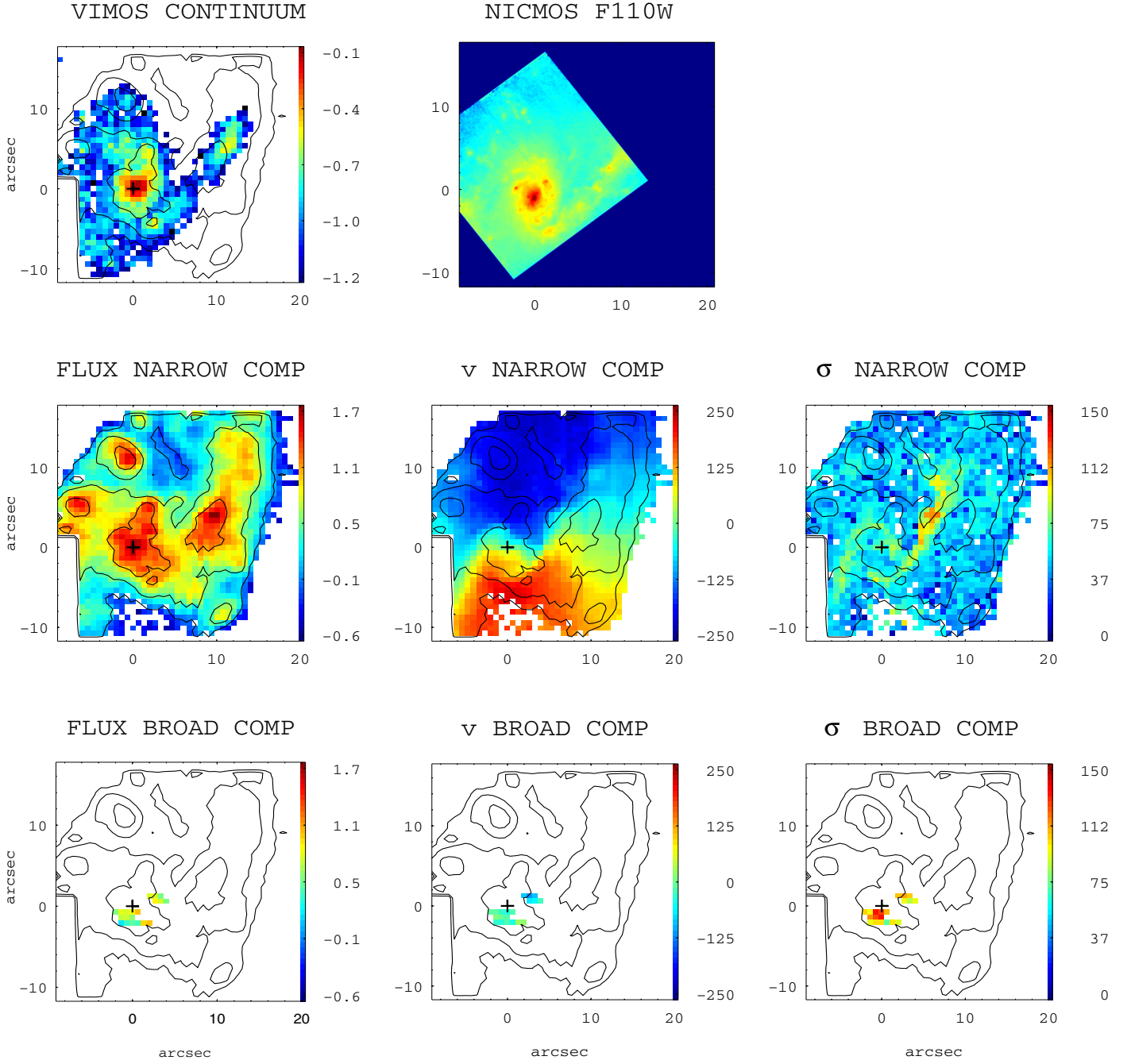


**Fig. A.22.** (General comments about the panels as in Fig. A.1.) IRAS F10015-0614 (NGC 3110): this galaxy shows two well-defined spiral arms in NICMOS/HST image. The velocity field and the velocity dispersion maps reproduce the spiral structure of this galaxy. Broad-profile spectra are found in regions of low- $H\alpha$  surface brightness round the nucleus. The spatial scale is  $0.343 \text{ kpc}''$ .

## IRAS F10038-3338

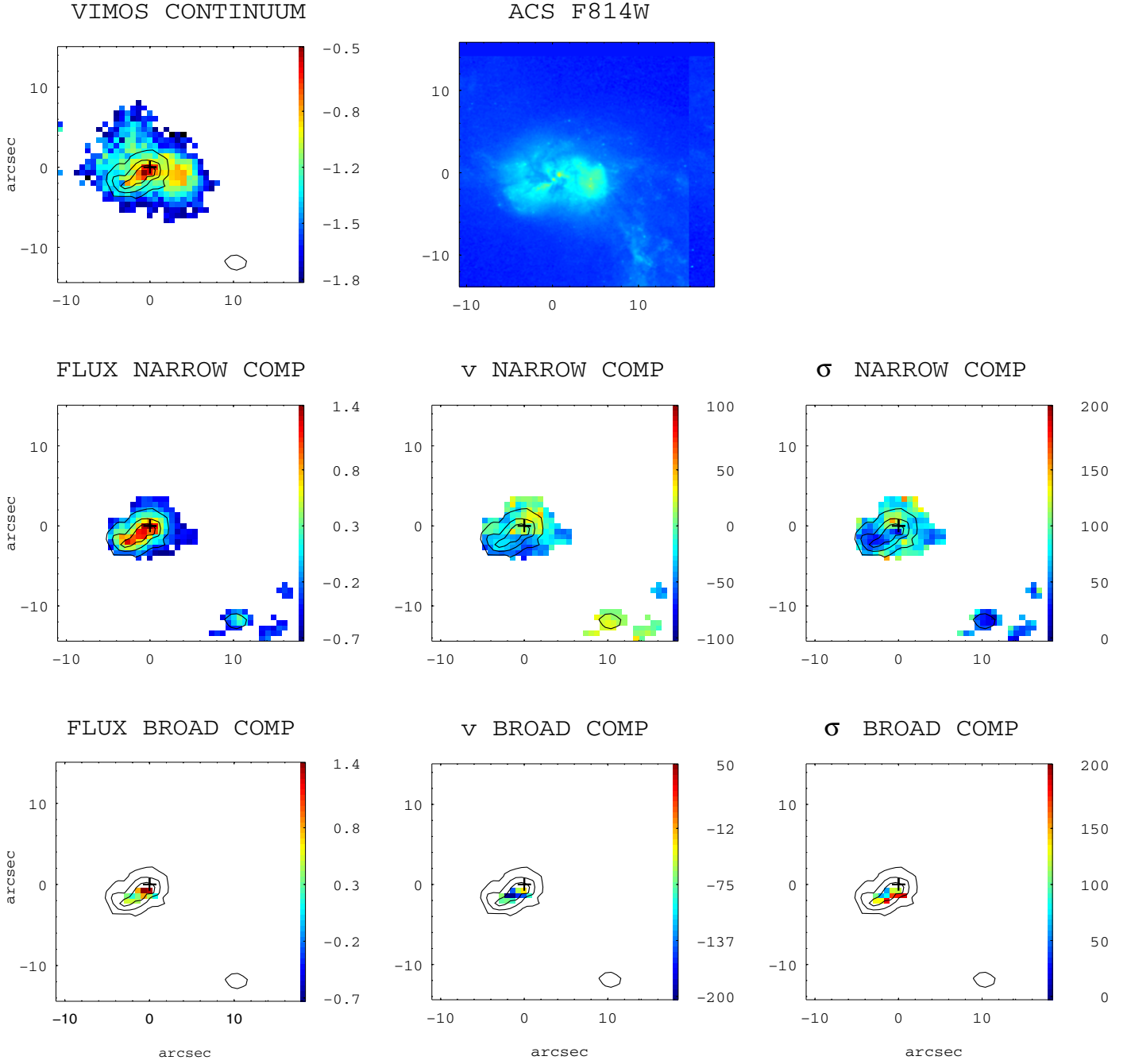


**Fig. A.23.** (General comments about the panels as in Fig. A.1.) IRAS F10038-3338 (IC 2545): the VIMOS continuum image shows two nuclei separated by  $\sim 3$  kpc. The  $H\alpha$  peak corresponds to the eastern nucleus. The velocity field and velocity dispersion maps are quite disturbed. The broad component is blueshifted by  $100 \text{ km s}^{-1}$ . The scale is of  $0.679 \text{ kpc}''$ .

## IRAS F10257-4339

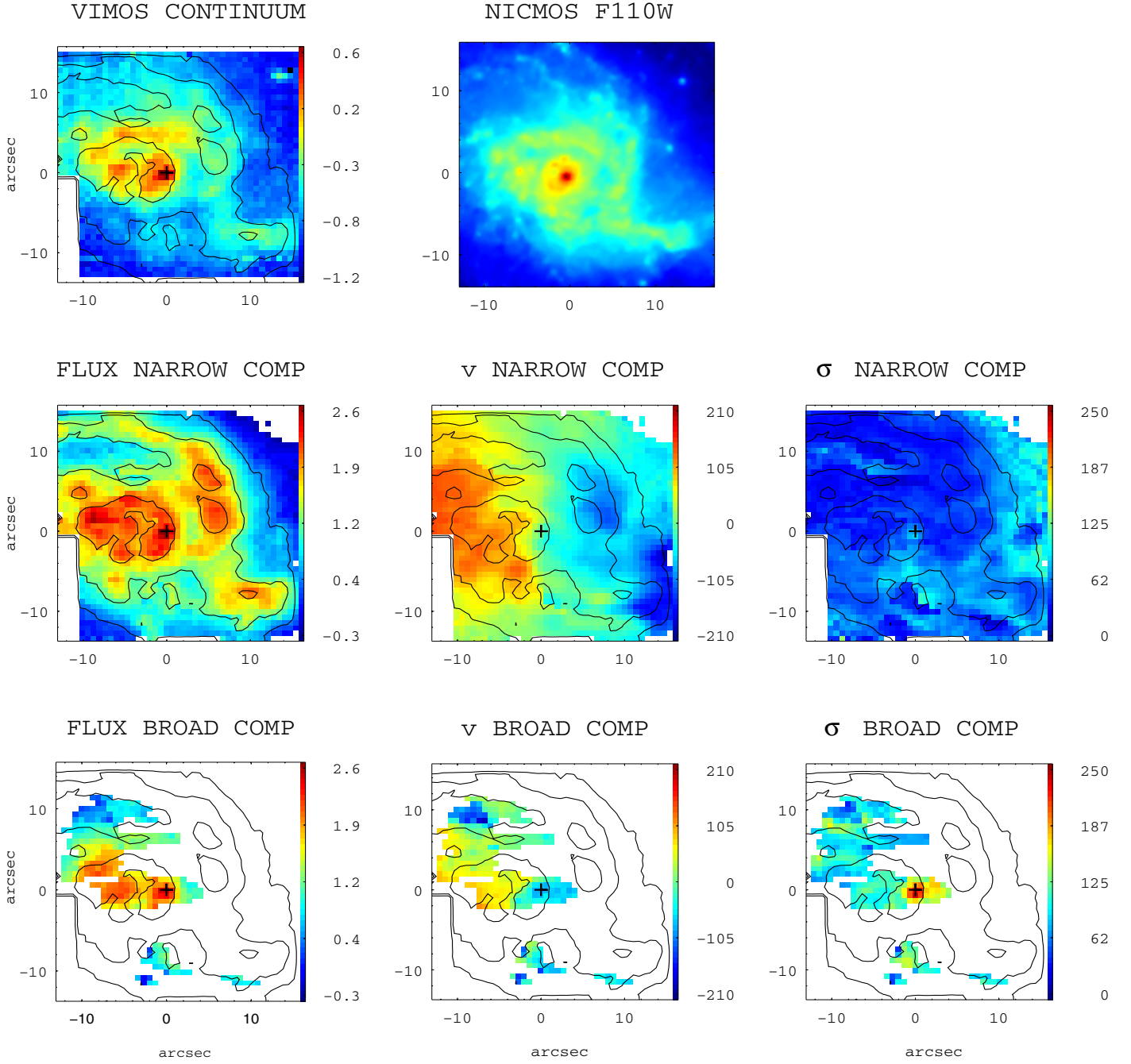


**Fig. A.24.** (General comments about the panels as in Fig. A.1.) IRAS F10257-4338 (NGC 3256): this galaxy has a somewhat complex morphological structure. It shows a clumpy pattern in the  $H\alpha$  flux intensity map. The velocity field of the narrow component has the kinematic axes not well defined, though a rotation component with an amplitude of  $170 \text{ km s}^{-1}$  can be identified. The velocity dispersion map shows high values in regions where high ionized gas is found (see [Monreal-Ibero et al. 2010](#)). The broad component has been found in a quite large and irregular area. The scale is of  $0.192 \text{ kpc''}$ .

## IRAS F10409-4556

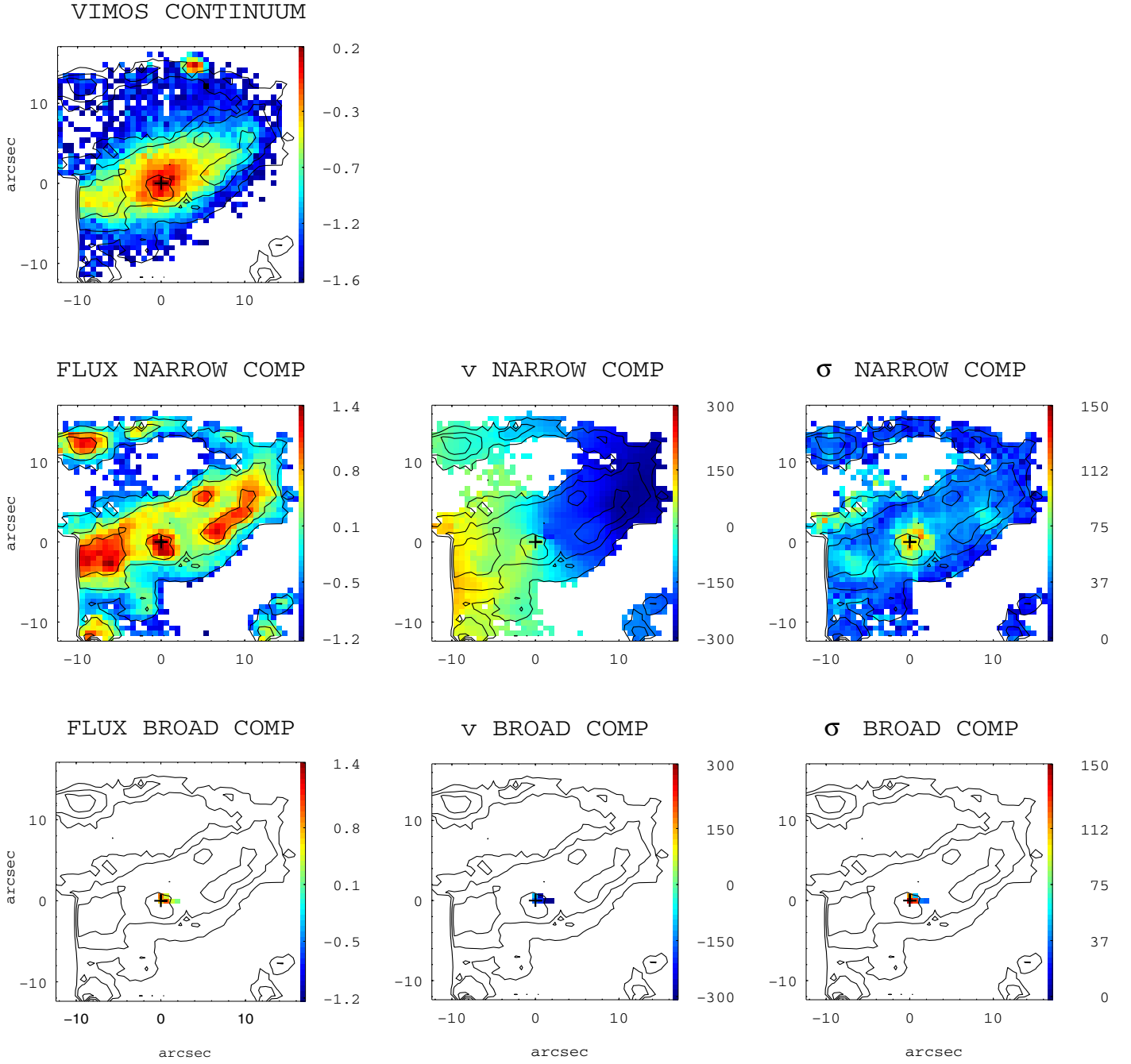


**Fig. A.25.** (General comments about the panels as in Fig. A.1.) IRAS F10409-4556 (ESO 264-G036): this is an isolated barred spiral galaxy morphologically classified as type 0 (i.e., *isolated disk*). Its velocity field is very regular and the velocity dispersion map is centrally peaked. The spatial scale is 0.425 kpc/".

## IRAS F10567-4310

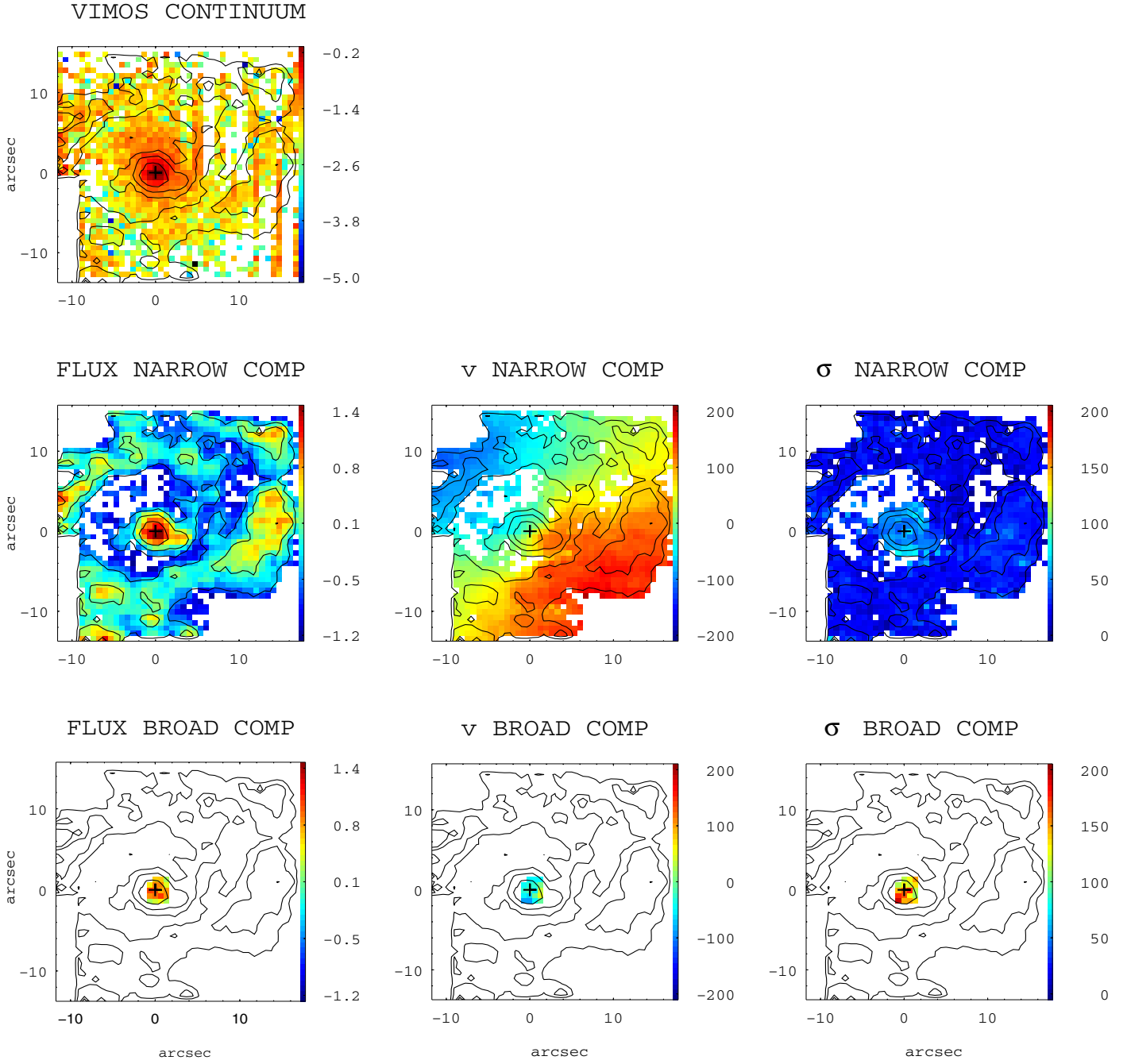


**Fig. A.26.** (General comments about the panels as in Fig. A.1.) IRAS F10567-4310 (ESO 264-G057): the continuum image shows vertical patterns, which were not possible to remove during the reduction process (see [Rodríguez-Zaurín et al. 2011](#)). However, the  $H\alpha$  maps are not affected by this problem. The narrow component shows a very regular velocity field and a centrally peaked velocity dispersion map. This object has been analyzed in [Bellocchi et al. \(2012\)](#). The scale is  $0.35 \text{ kpc}''$ .



## IRAS F11255-4120

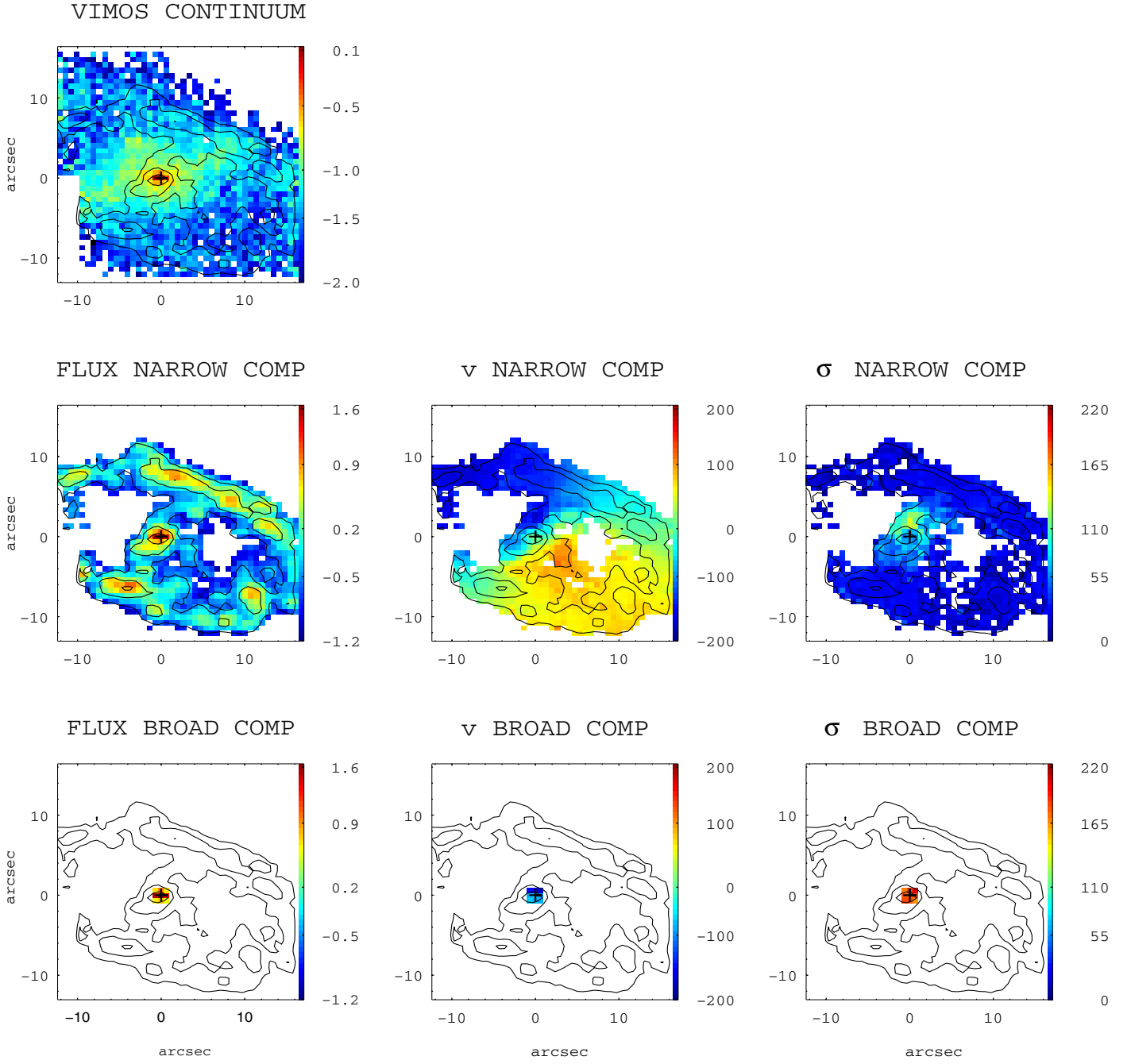


**Fig. A.27.** (General comments about the panels as in Fig. A.1.) IRAS F11255-4120 (ESO 319-G022): this is a barred spiral with a circumnuclear ring structure that is at  $\sim 4$  kpc from the nuclear region in the  $H\alpha$  image but not observed in the continuum images. Interestingly, the orientation of the bar seen in continuum emission ( $PA \sim 110^\circ$ ) is different from that of the ionized gas emission ( $PA \sim 150^\circ$ ). The projected orientation of the rotation axis (minor kinematic axis) seems to be different by about  $30^\circ$  from that of the minor photometric axis (and the bar in the  $H\alpha$  flux intensity map) but is well aligned with the bar in the continuum. The kinematic center closely agrees with that of the  $H\alpha$  flux and the continuum peaks. The velocity field is very regular and the velocity dispersion map has an almost centrally peaked structure with a local maximum of  $120 \text{ km s}^{-1}$  in the bar structure. This object has been previously studied in [Bellocchi et al. \(2012\)](#). The scale is of  $0.333 \text{ kpc}''$ .

## IRAS F11506-3851

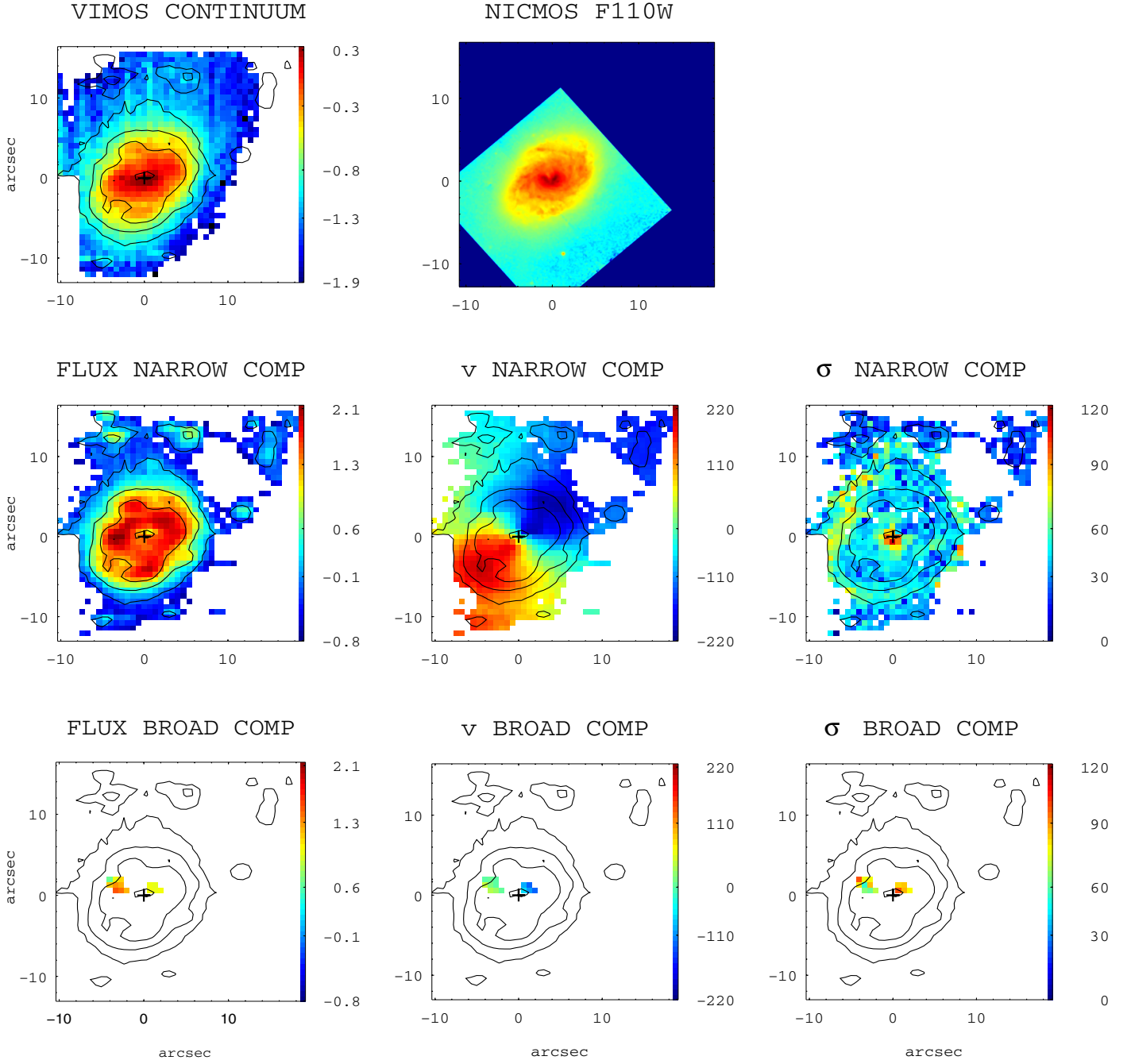


**Fig. A.28.** (General comments about the panels as in Fig. A.1.) IRAS F11506-3851 (ESO 320-G030): a circumnuclear ring structure is detected in the  $H\alpha$  image. The velocity field is extremely regular and the velocity dispersion map is centrally peaked (i.e.,  $\sigma_c = 81 \text{ km s}^{-1}$ ) with high values (i.e.,  $\sim 60 \text{ km s}^{-1}$ ) outwards the ring structure. The spatial scale is of  $0.221 \text{ kpc''}$ .

## IRAS F12043-3140

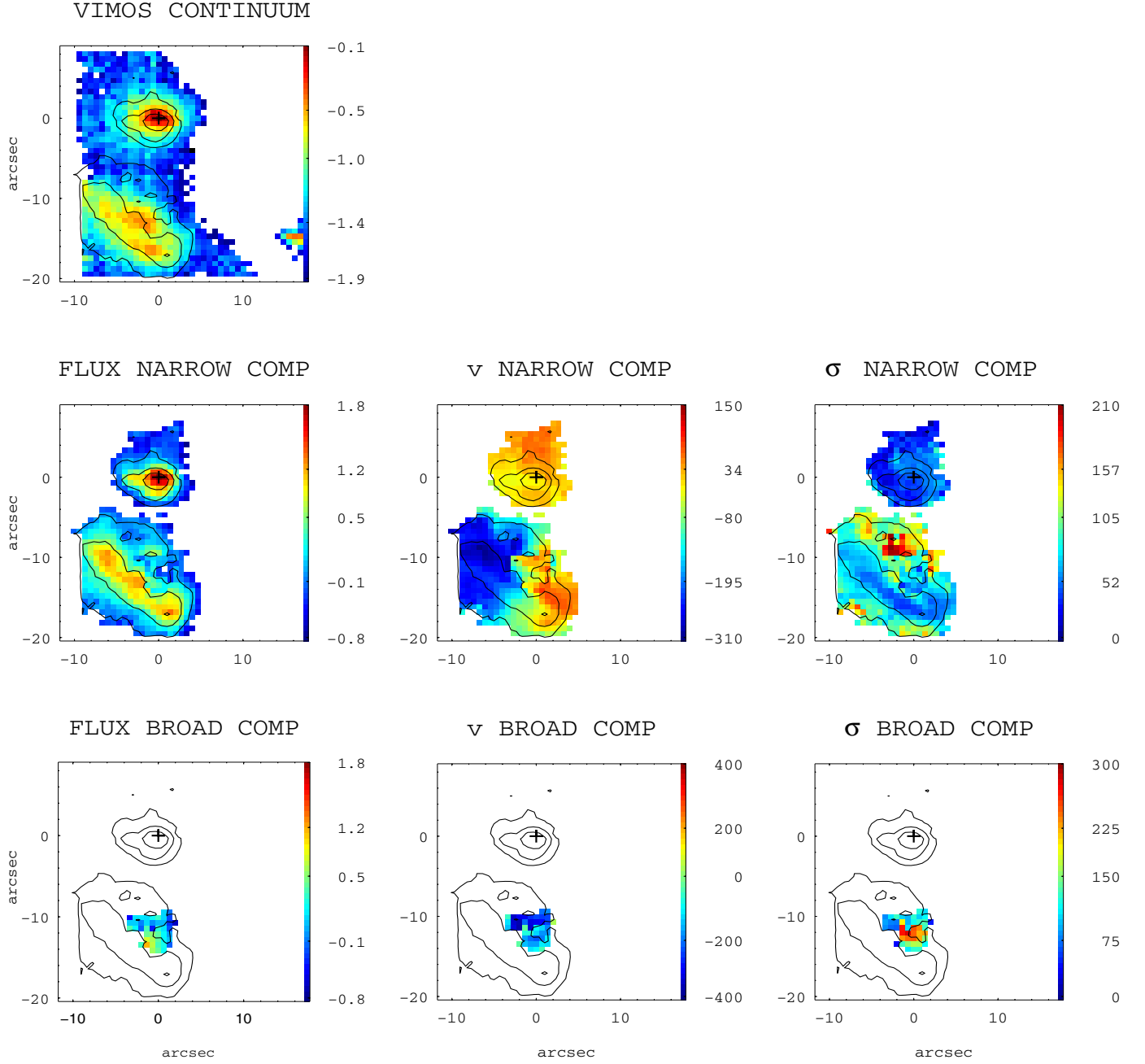


**Fig. A.29.** (General comments about the panels as in Fig. A.1.) IRAS 12043-3140 (ESO 440-IG058): this system consists of two galaxies with a nuclear separation of  $\sim 6$  kpc. The northern galaxy is compact, while the southern source presents several knots in the  $H\alpha$  map. The velocity field of the southern galaxy has two relatively well-defined approaching and receding parts, with the kinematic and photometric axes in relatively good agreement. Its velocity dispersion map reaches the highest values (i.e.,  $\sigma \sim 250 \text{ km s}^{-1}$ ) in the northern part, in correspondence of a local maximum of the  $H\alpha$  intensity map. Around that region, a secondary broad component has been found in some spectra. The stellar distribution (i.e., continuum map) of the northern galaxy suggests that it is almost face-on: this could possibly explain the derived relatively low velocity shear (i.e.,  $\sim 42 \text{ km s}^{-1}$ ). Its velocity field shows a somewhat irregular pattern. The scale is of  $0.468 \text{ kpc''}$ .

## IRAS F12115-4656

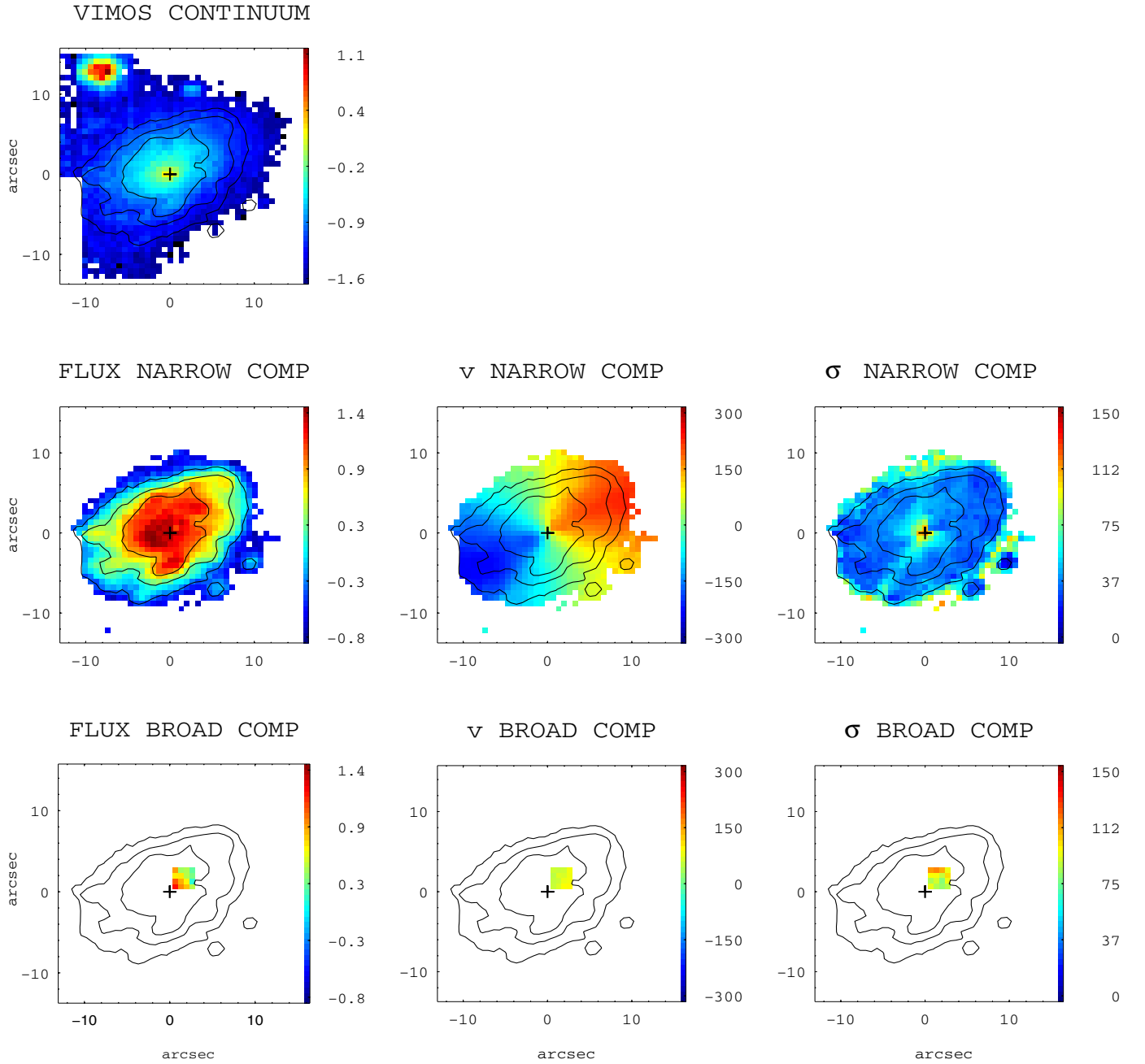


**Fig. A.30.** (General comments about the panels as in Fig. A.1.) IRAS 12115-4656 (ESO 267-G030): the  $H\alpha$  image shows a peak displaced by 0.8 kpc in the southwest direction with respect to the nucleus (continuum maximum). The kinematic center is in positional agreement with the nucleus. The velocity field and velocity dispersion map are those typical of a rotating *disk*-like object. At about  $\sim 3$  kpc northwest from the nucleus, the spectra show the presence of two kinematically distinct components. The scale is of 0.375 kpc $''$ .

## IRAS 12116-5615

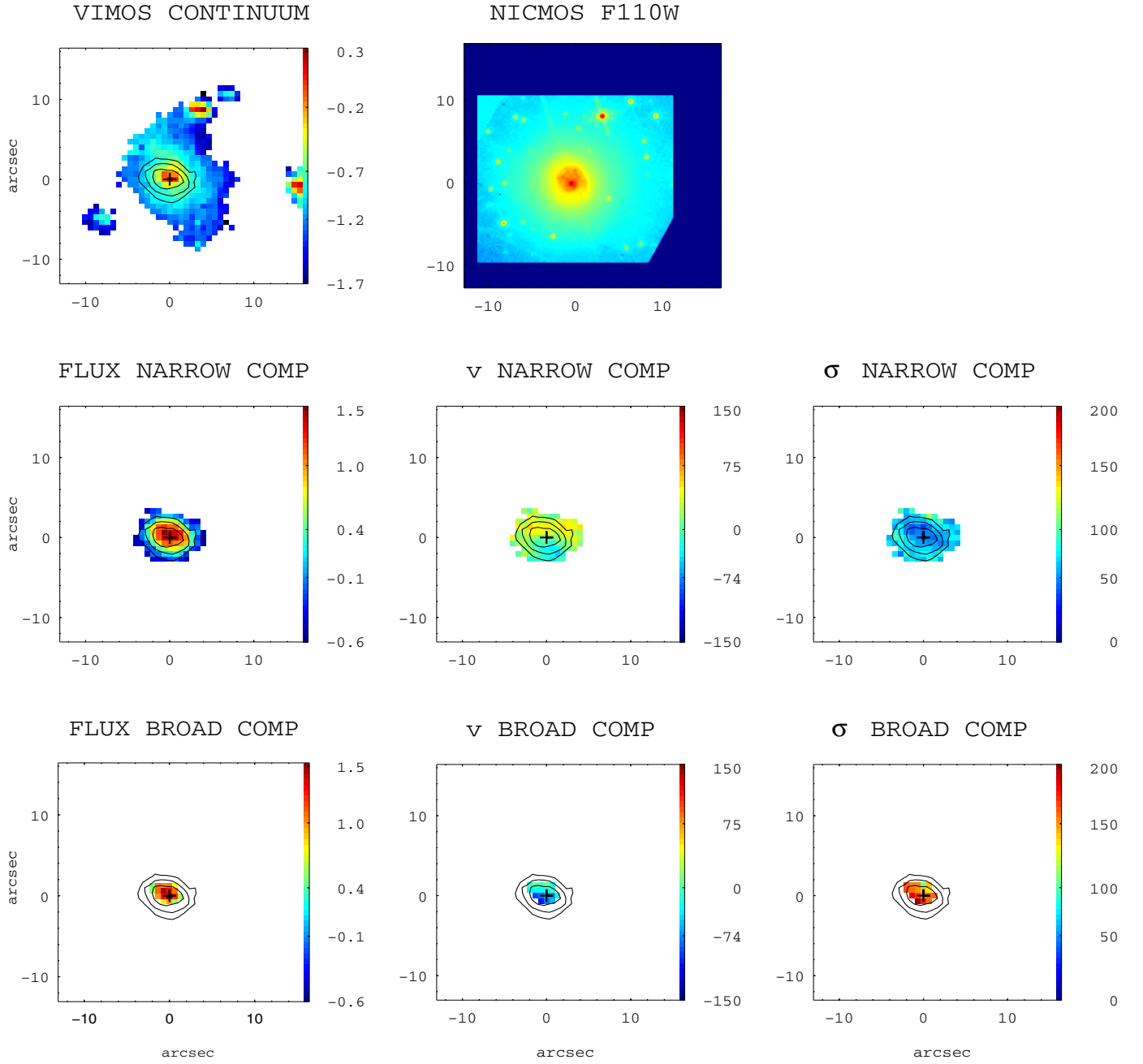


**Fig. A.31.** (General comments about the panels as in Fig. A.1.) IRAS 12116-5615: this is one of the few objects for which the morphological classification is uncertain (class 2 or 0). It shows a very compact H $\alpha$  emission. The H $\alpha$  velocity field has a typical rotation pattern, but the velocity dispersion map is not centrally peaked. The latter shows higher values in the outer parts, which also have high excitation and low-H $\alpha$  surface brightness (see Monreal-Ibero et al. 2010). The scale is of 0.545 kpc''.



## IRAS F12596-1529

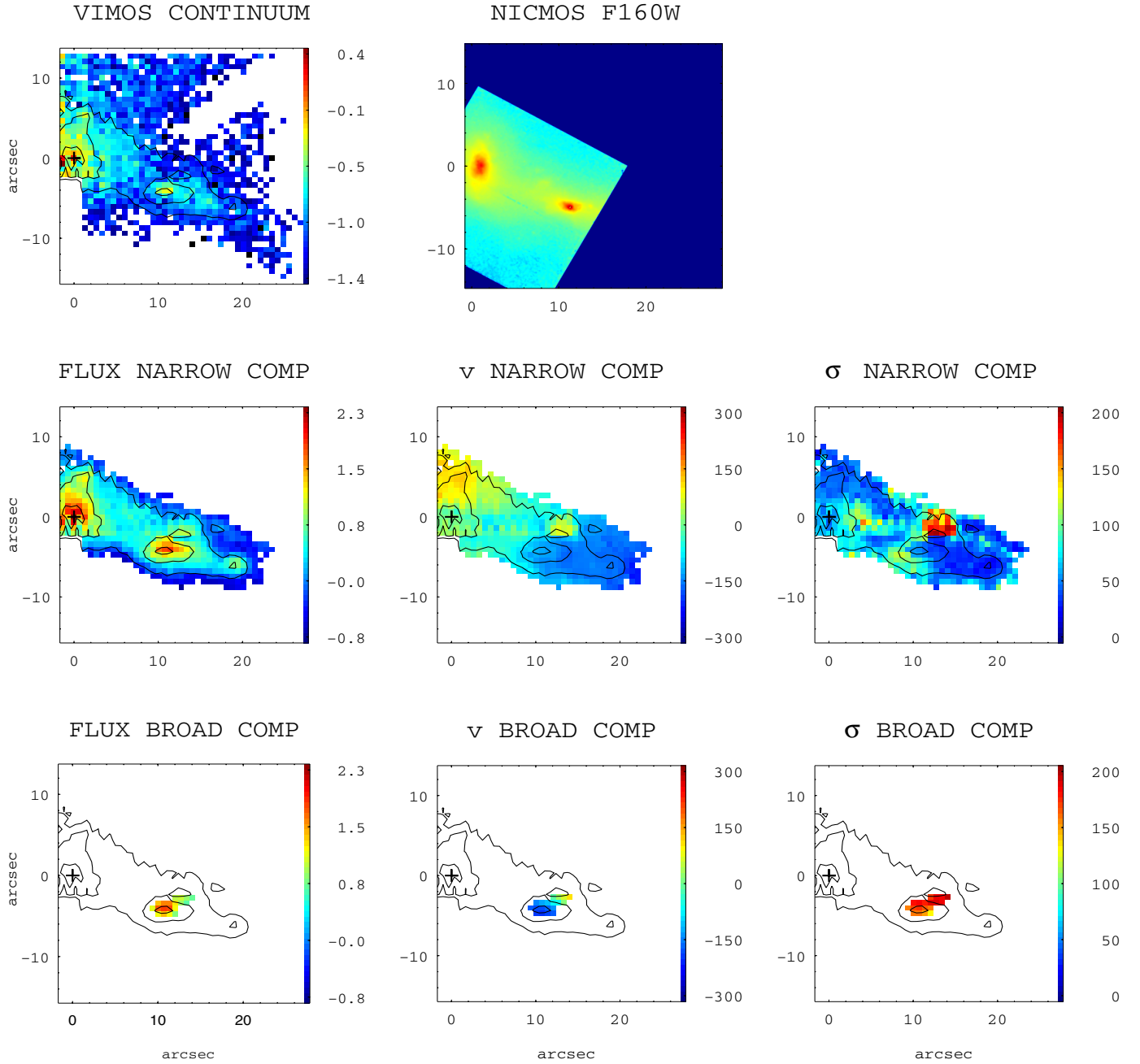


**Fig. A.32.** (General comments about the panels as in Fig. A.1.) IRAS 12596-1529 (MGC-02-33-098): this system is interacting with MCG-02-33-099, at  $\sim 37$  kpc in the southeast direction. The HST image clearly shows two distinct galaxies in interaction, still visible in the VIMOS  $H\alpha$  flux intensity map, where the nuclei are separated by  $\sim 5$  kpc. For this system it was not possible to reliably separate the contribution of each object. The two galaxies have been considered as a whole systems, deriving the mean kinematic values reported in Table 4. However, the velocity field shows a quite regular pattern. The velocity dispersion map does not have a well-defined structure with a maximum of  $\sim 200$  km s $^{-1}$  in the northern part of the western galaxy: in this region low- $H\alpha$  surface brightness spectra are well fitted using one component and for this reason show a broader profile. However, no kinematic classification can be inferred from the whole system. The spatial scale is of 0.324 kpc''.

## IRAS F13001-2339

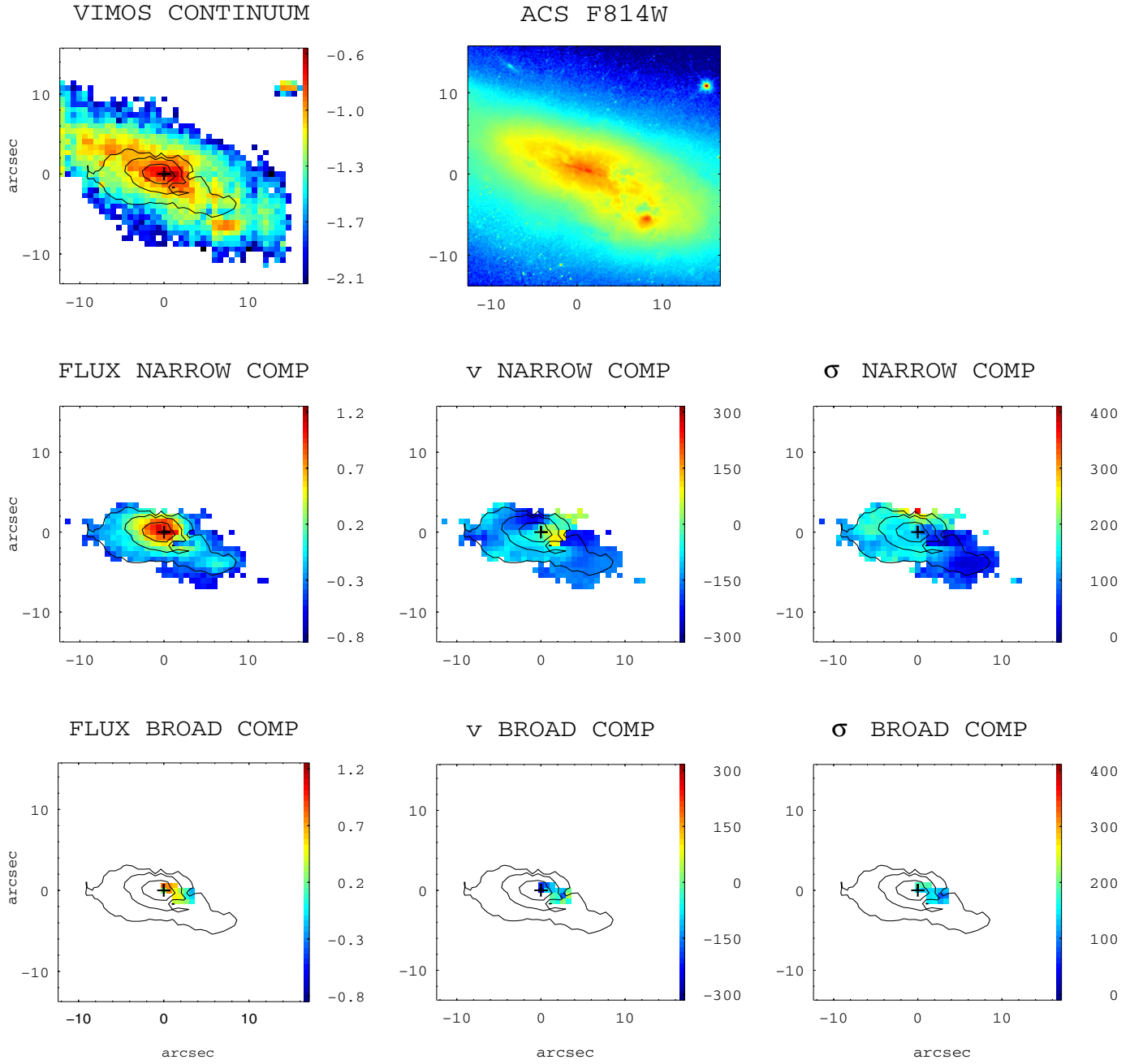


**Fig. A.33.** (General comments about the panels as in Fig. A.1.) IRAS F13001-2339 (ESO 507-G070): the velocity field and velocity dispersion map have an irregular pattern. Some of the spectra in the northern region show a broad profile and relatively high excitation (see [Monreal-Ibero et al. 2010](#)). Its scale is of  $0.439 \text{ kpc}''$ .

## IRAS F13229-2934

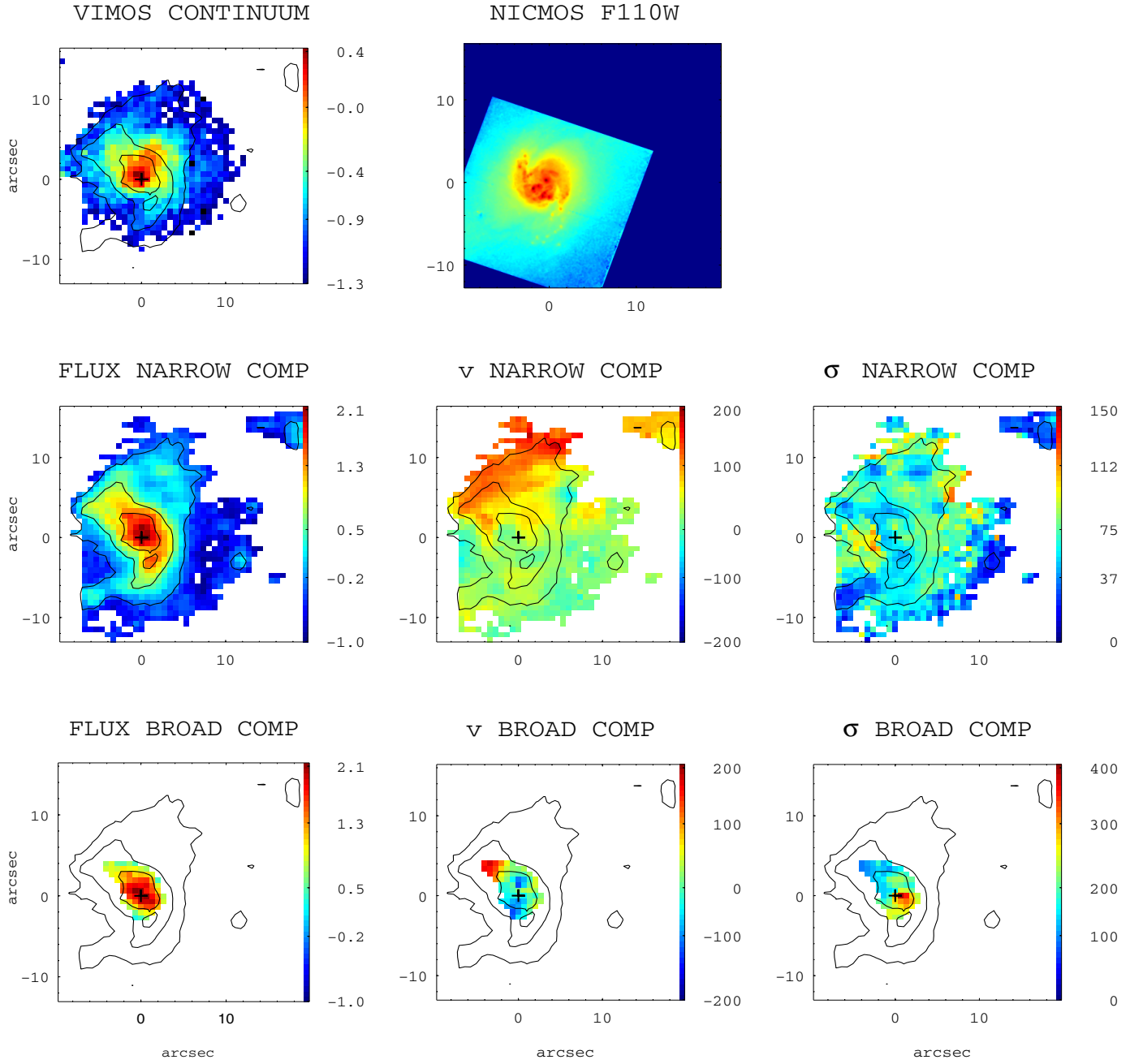


**Fig. A.34.** (General comments about the panels as in Fig. A.1.) IRAS F13229-2934 (NGC 5135): the morphology of the ionized gas emission is substantially different from that of the continuum. Moreover, the photometric major axis of the continuum image seems to be perpendicular with respect to that of the H $\alpha$  flux intensity in the inner regions. The spatial scale is 0.28 kpc/".

## IRAS F14544-4255 (East)

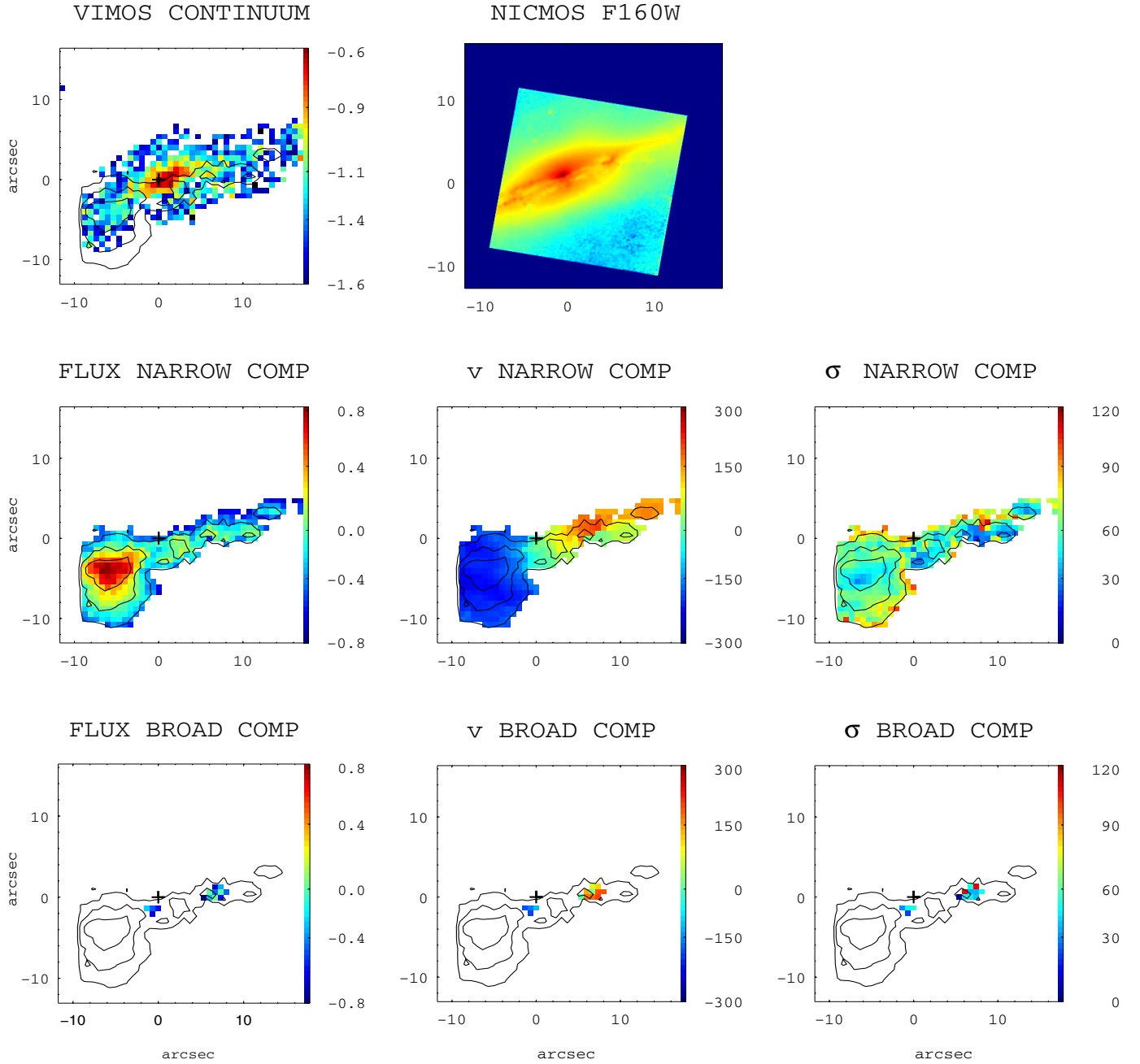


**Fig. A.35.** (General comments about the panels as in Fig. A.1.) IRAS F14544-4255 (IC 4518): this system is formed by two galaxies with a nuclear separation  $\sim 12$  kpc, which were observed separately using two VIMOS pointings. The present panels correspond to the eastern source. This galaxy has a faint tail extended towards the northwest, as seen in the DSS image (see Paper III). The  $H\alpha$  image reveals a very strong knot of star formation towards the southeast of the nucleus ( $\sim 2.5$  kpc): for this reason, the VIMOS continuum peak is used to identify the center (0,0) of the images. The velocity field is rather regular, although some deviations of pure rotation pattern are seen towards the west, probably due to the projection of star-forming knots with peculiar velocity. Its velocity dispersion map has a relatively constant value of  $\sigma_{\text{mean}} \sim 60 \text{ km s}^{-1}$  in almost the whole FoV. The broad component found in a few spectra has velocity dispersion values similar to those of the narrow component. The spatial scale is of  $0.32 \text{ kpc''}$ .

## IRAS F14544-4255 (West)

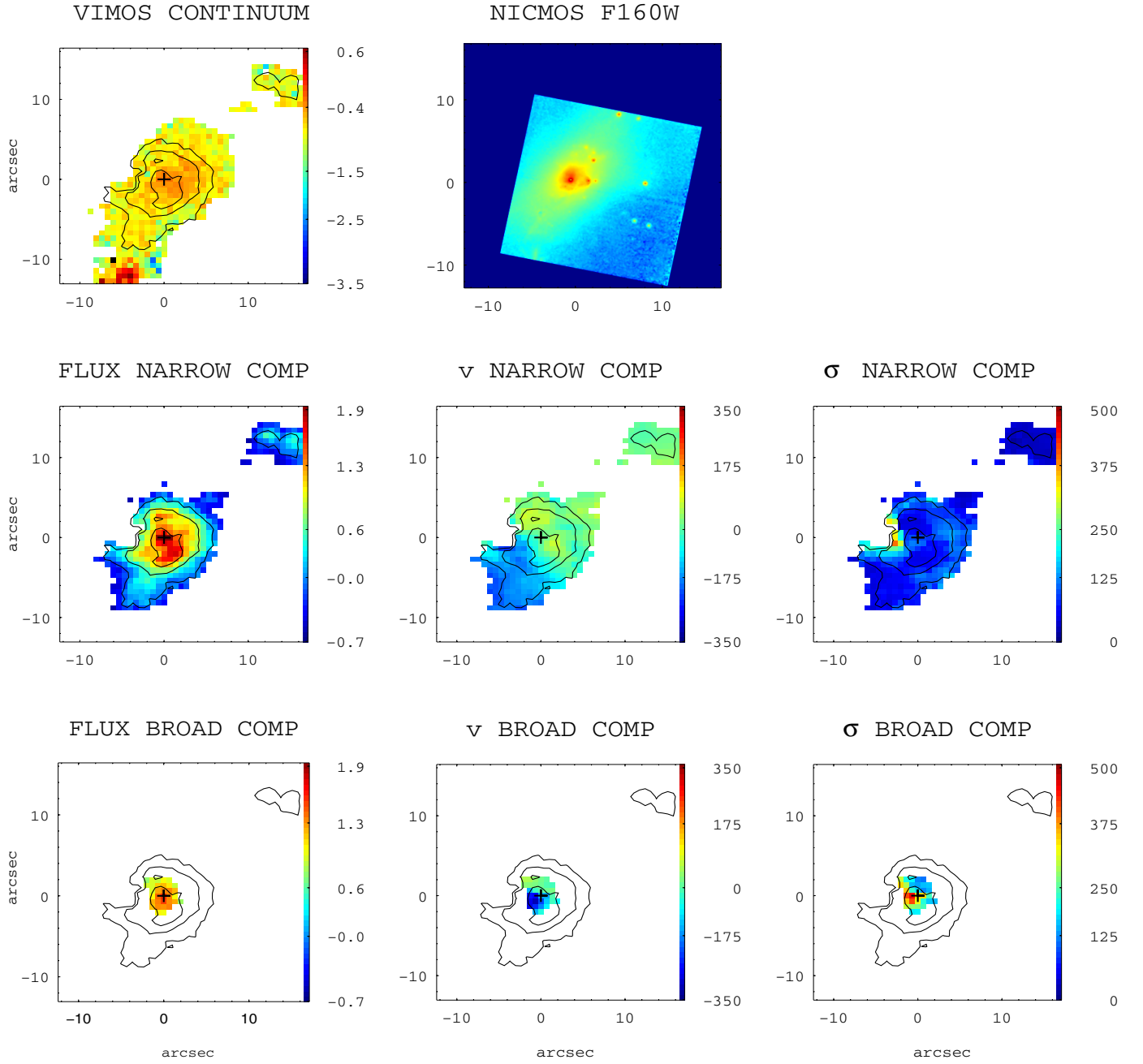


**Fig. A.36.** (General comments about the panels as in Fig. A.1.) IRAS F14544-4255 (IC 4518): this is the western source of the system. It is more compact than the eastern one, although some extended emission is also observed towards the northwest likely associated with two star-forming knots. The velocity field has some irregularities (i.e., two maxima in the redshifted part), although a weak rotation pattern is visible. The velocity dispersion map shows a maximum of  $300 \text{ km s}^{-1}$  on the eastern part of this galaxy at 0.9 kpc from the  $\text{H}\alpha$  flux peak. The high values of the velocity dispersion of the narrow component correspond to low- $\text{H}\alpha$  surface brightness spectra. The spectra showing a secondary broad component in this object are quite complex. The spatial scale is  $0.32 \text{ kpc}''$ .



## IRAS F17138-1017

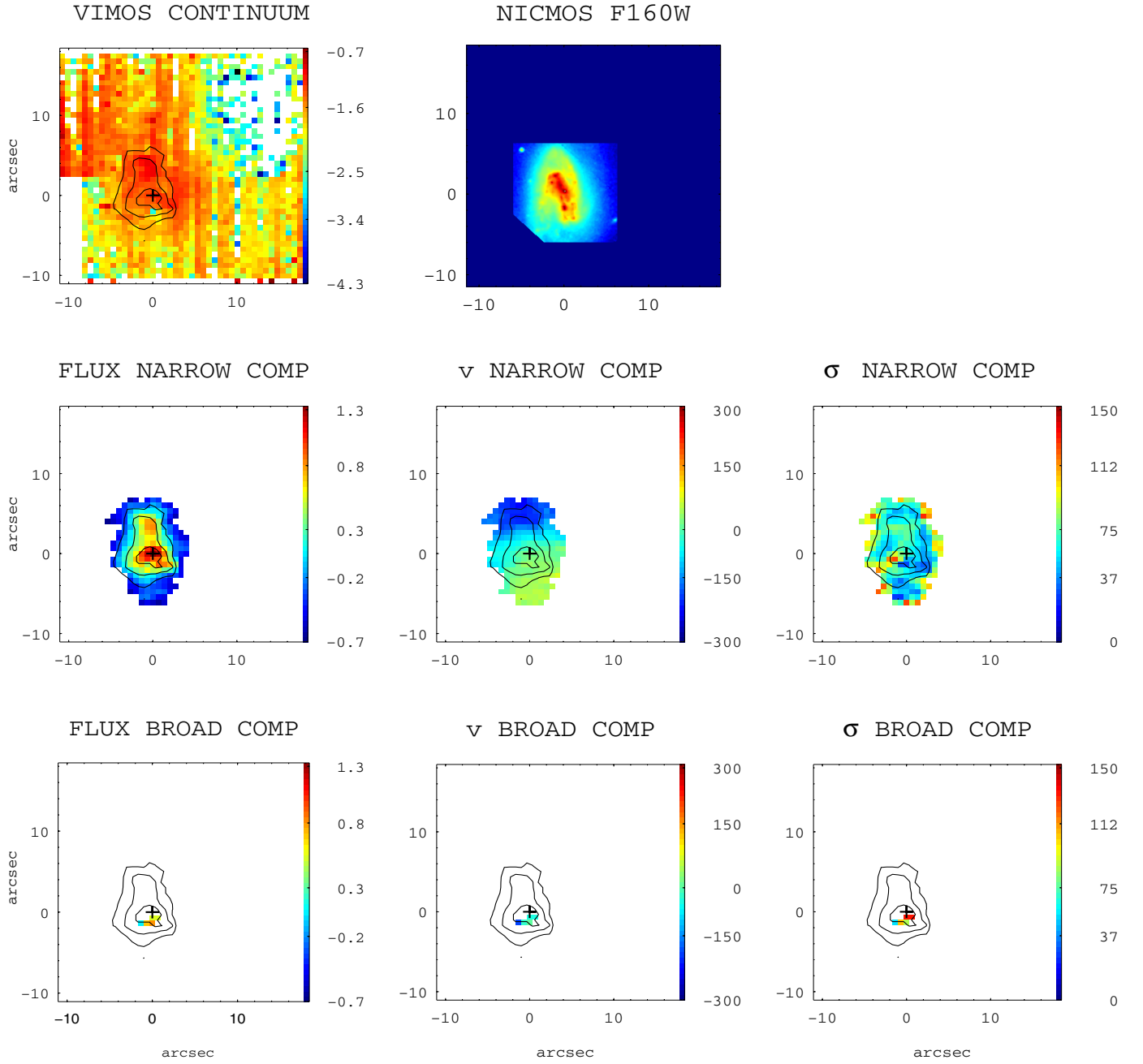


**Fig. A.37.** (General comments about the panels as in Fig. A.1.) IRAS F17138-1017: the velocity field is regular, while the velocity dispersion map has no defined pattern. The continuum image shows vertical patterns that could not be removed during the reduction process (see Rodríguez-Zaurín et al. 2011). However, the H $\alpha$  maps (flux intensity and velocity field) are not affected by this problem. The spatial scale is 0.352 kpc''.

## IRAS F18093-5744 N (IC 4687)

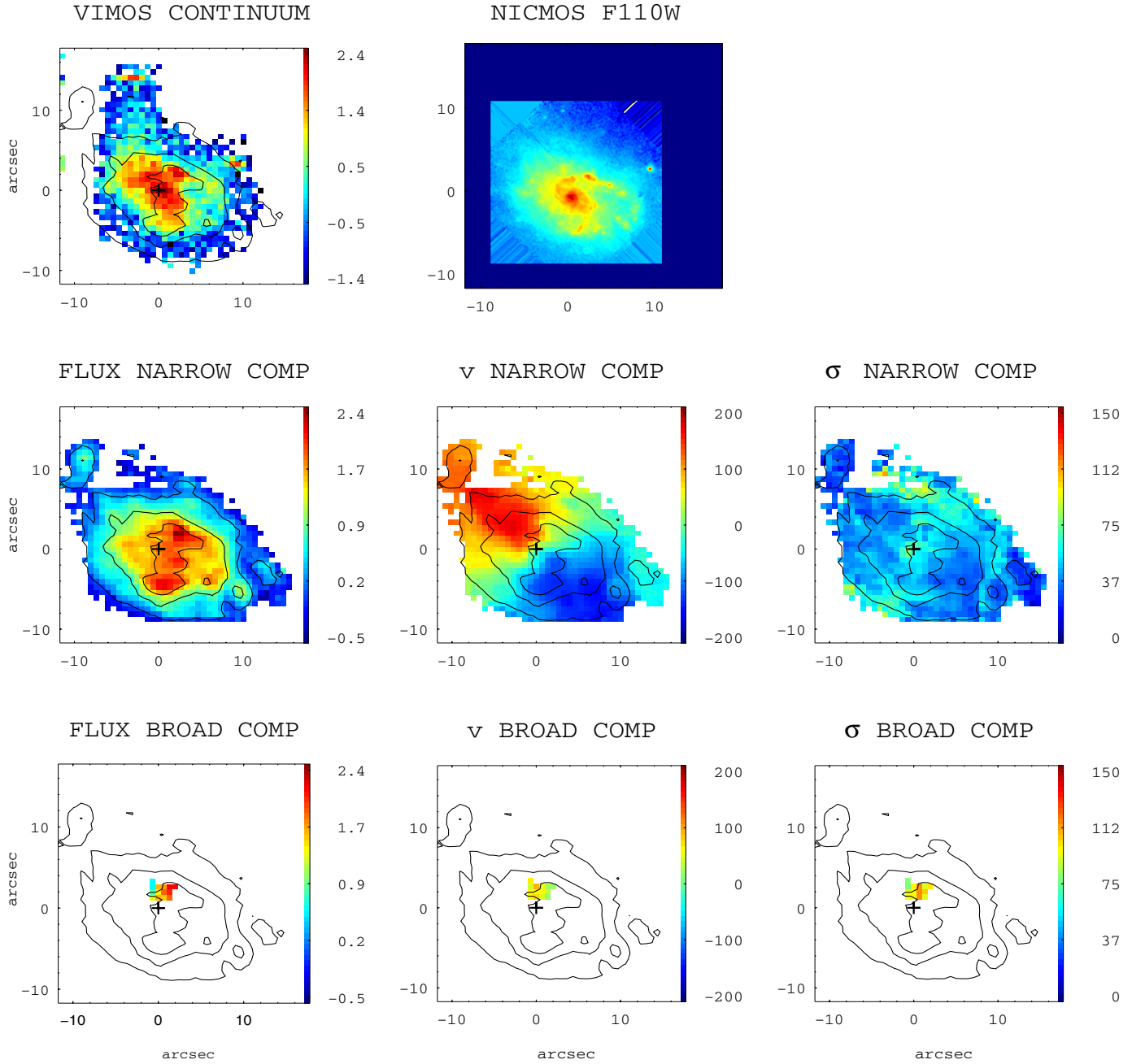


**Fig. A.38.** (General comments about the panels as in Fig. A.1.) IRAS F18093-5744: the whole system consists of three galaxies in interaction, which have been observed separately. The nuclear separations between the northern (IC 4687) and the central galaxy (IC 4686) and between the central and the southern galaxy (IC 4689) are  $\sim 10$  kpc and  $\sim 20$  kpc, respectively. The HST (F110W) image shows a spiral-like morphology for IC 4687, with several knots and concentrations in the nuclear region. IC 4687 shows a velocity field dominated by rotation, with the kinematic center well defined and coincident with the nucleus (continuum maximum). On the other hand, the velocity dispersion map shows an almost centrally peaked map, with higher values in the outer parts of the galaxy, corresponding to ionized regions (see [Monreal-Ibero et al. 2010](#)). The scale is  $0.353 \text{ kpc}''$ .

## IRAS F18093-5744 C (IC 4686)

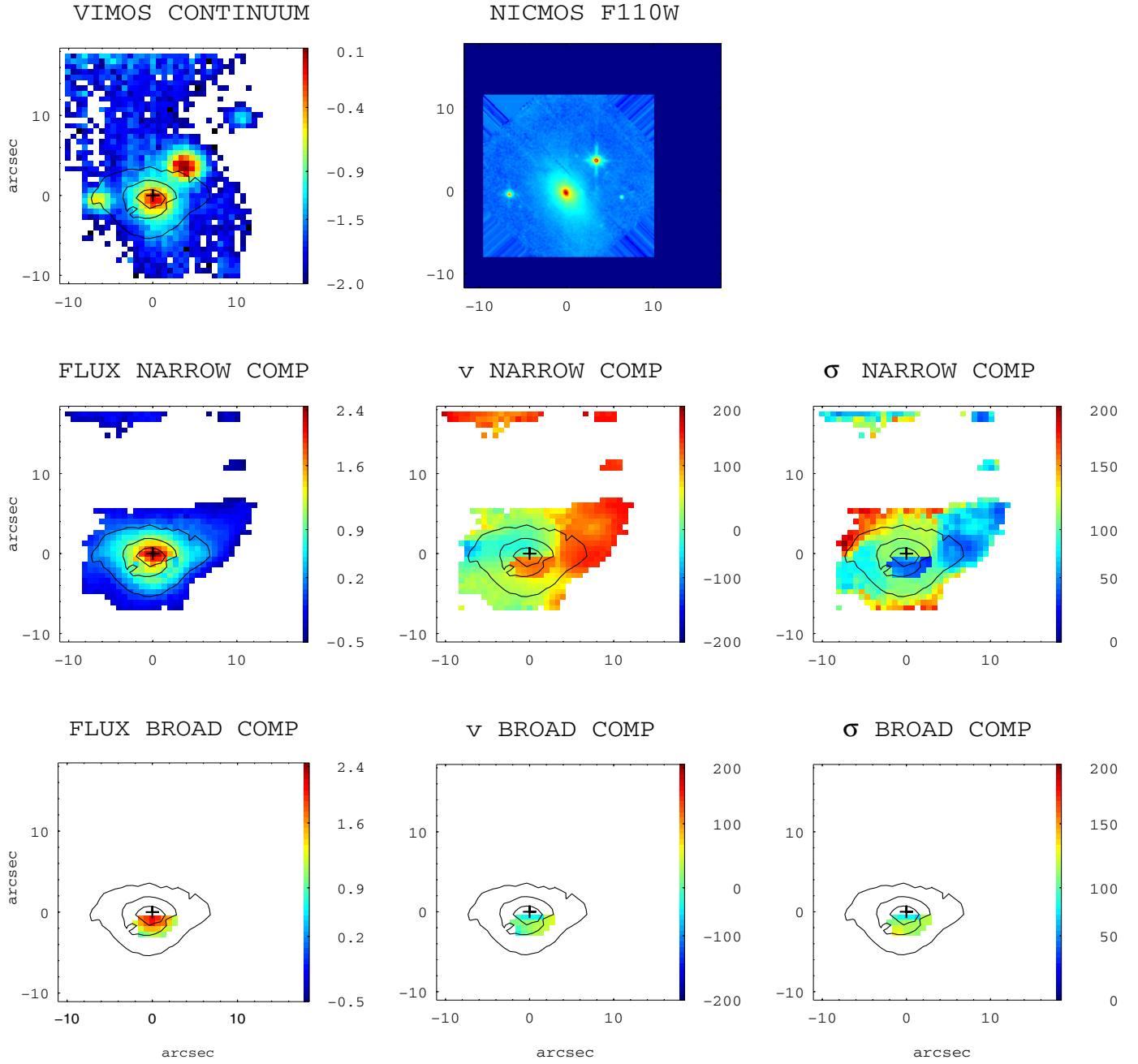


**Fig. A.39.** (General comments about the panels as in Fig. A.1.) IRAS F18093-5744 (C): the  $H\alpha$  emission from the source is highly concentrated in the nuclear region. Ionized gas emission is also observed extending towards the northwest of the nuclear region, probably as part of a tidal tail linking this galaxy with IC 4687. The VIMOS continuum emission is strongly contaminated by a star located in the northwest part with respect to the galaxy. The northern/western part of the velocity field is dominated by the kinematics of the tidal tail, which shows redshifted velocities and very low velocity dispersion: the blue part of the velocity field is not well defined, even excluding the region south of the nucleus. Due to the presence of the tidal tail, the interpretation of the broad component in the innermost region is uncertain (i.e., it may correspond to the main systemic component because it is the narrow one associated with the tidal tail). The scale is  $0.353 \text{ kpc}''$ .

## IRAS F18093-5744 S (IC 4689)

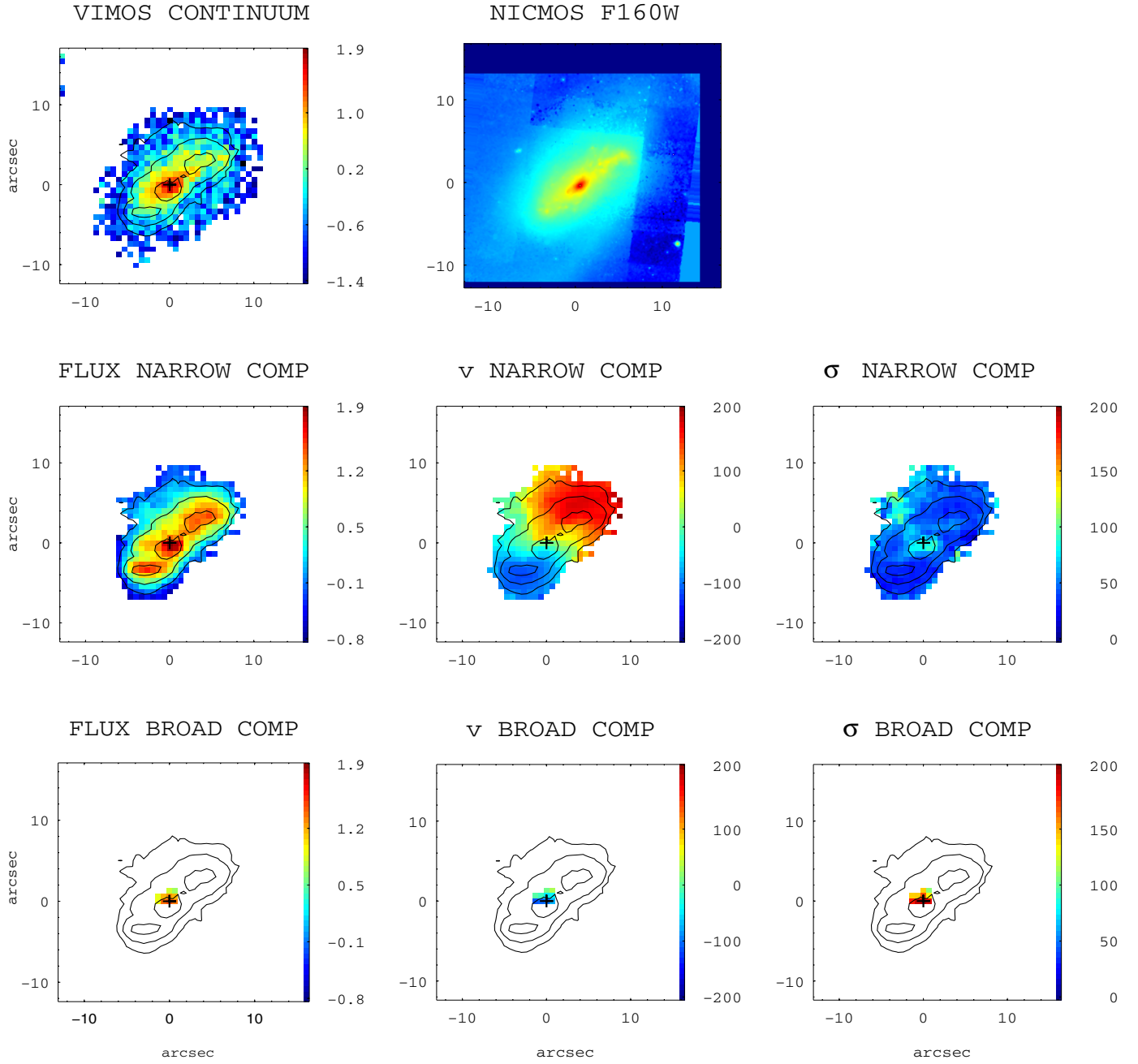


**Fig. A.40.** (General comments about the panels as in Fig. A.1.) IRAS F18093-5744 (S) (IC 4689): this galaxy has a spiral morphology in the NICMOS/HST image, without clear evidence of strong interaction with the other galaxies of the system. The kinematic center seems to be coincident with the VIMOS continuum peak: the velocity field shows a mostly regular pattern, typical of a rotation-dominated *disk*-like object. Its velocity dispersion map shows a centrally peaked structure. It also shows regions in the northern part with relatively large velocity dispersion ( $\sim 100 \text{ km s}^{-1}$ ). A small area ( $\sim 0.6 \text{ kpc}^2$ ) at the center shows the presence of a broad component, blueshifted by  $\sim 85 \text{ km s}^{-1}$ . The scale is  $0.353 \text{ kpc}''$ .

## IRAS F21130-4446

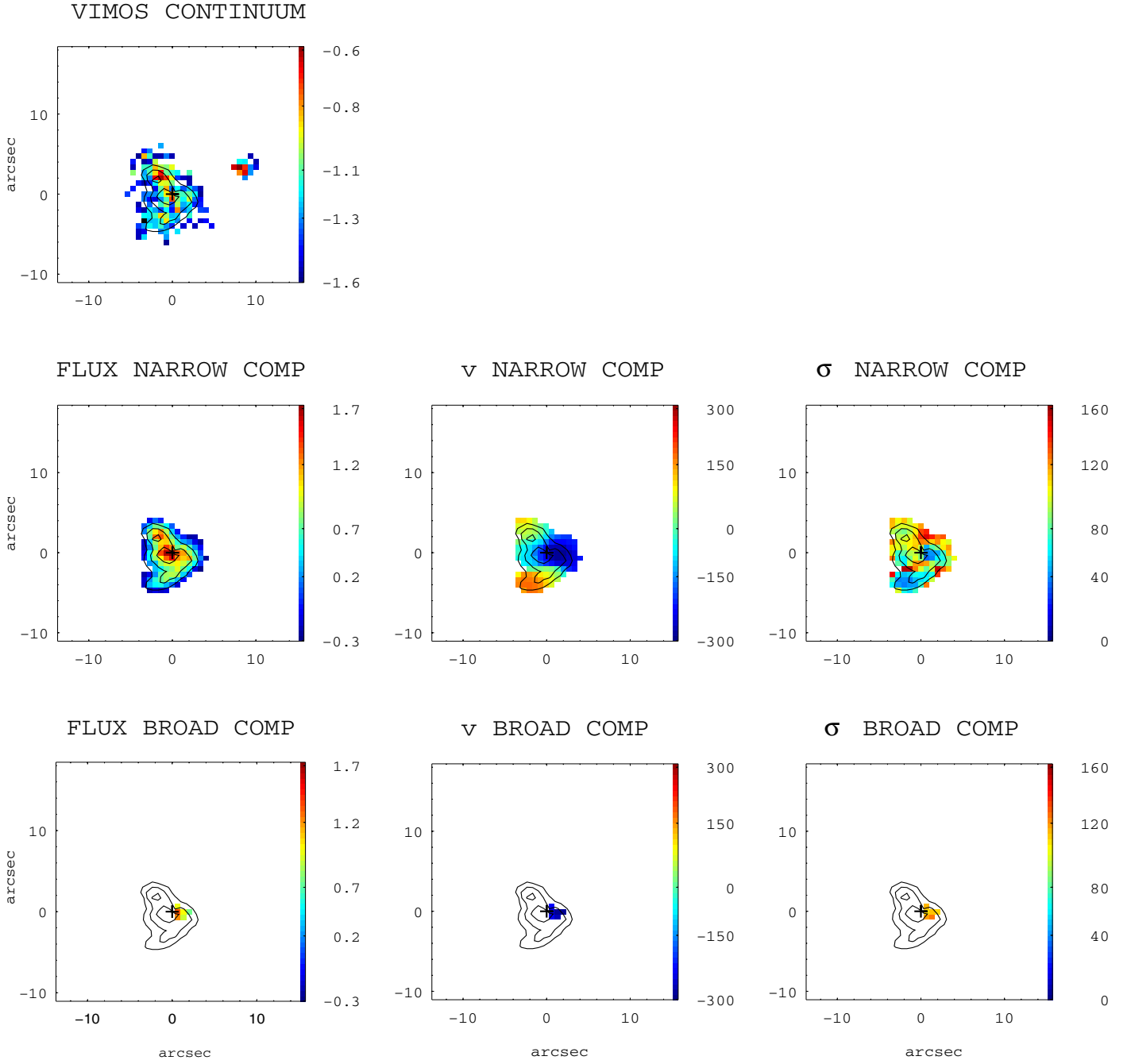


**Fig. A.41.** (General comments about the panels as in Fig. A.1.) IRAS F21130-4446: this system has a double nucleus with a separation of 5.4 kpc (i.e., [Dasyra et al. 2006b](#)). The peak of the continuum emission coincides with the location of the northern (weaker)  $H\alpha$  condensation. The velocity field has a quite complex structure. The velocity dispersion map shows a distorted and irregular structure. The scale is of 1.72 kpc''.

## IRAS F21453-3511

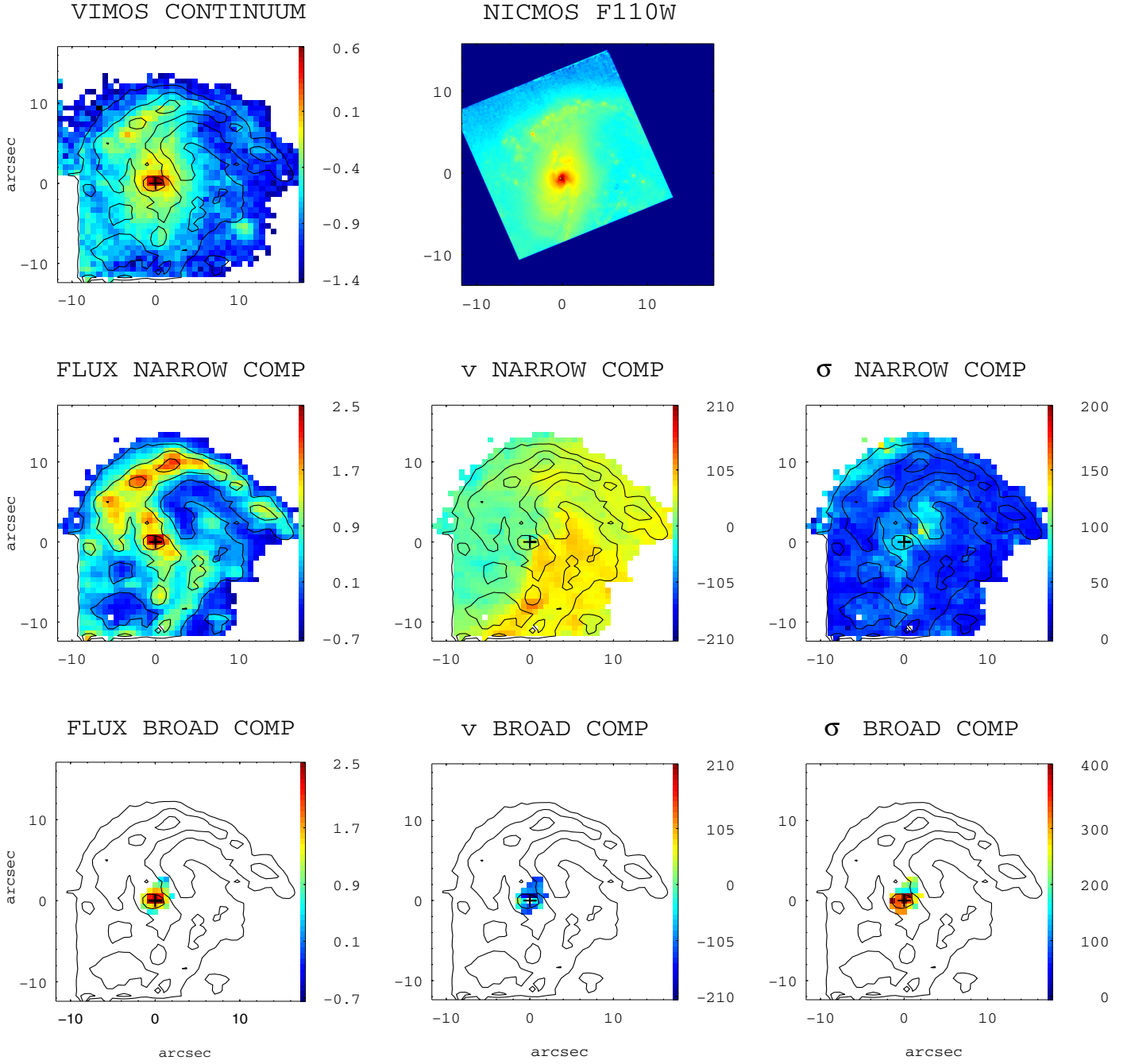


**Fig. A.42.** (General comments about the panels as in Fig. A.1.) IRAS F21453-3511 (NGC 7130): the velocity field and velocity dispersion maps of the narrow component show asymmetric patterns. In the velocity field three main regions can be identified with the rotation axes not well-defined. The velocity dispersion map shows high values in the northern arm and its central part, with values larger than  $100 \text{ km s}^{-1}$ . This object has been analyzed in [Bellocchi et al. \(2012\)](#). The scale is  $0.329 \text{ kpc''}$ .



## IRAS F22132-3705

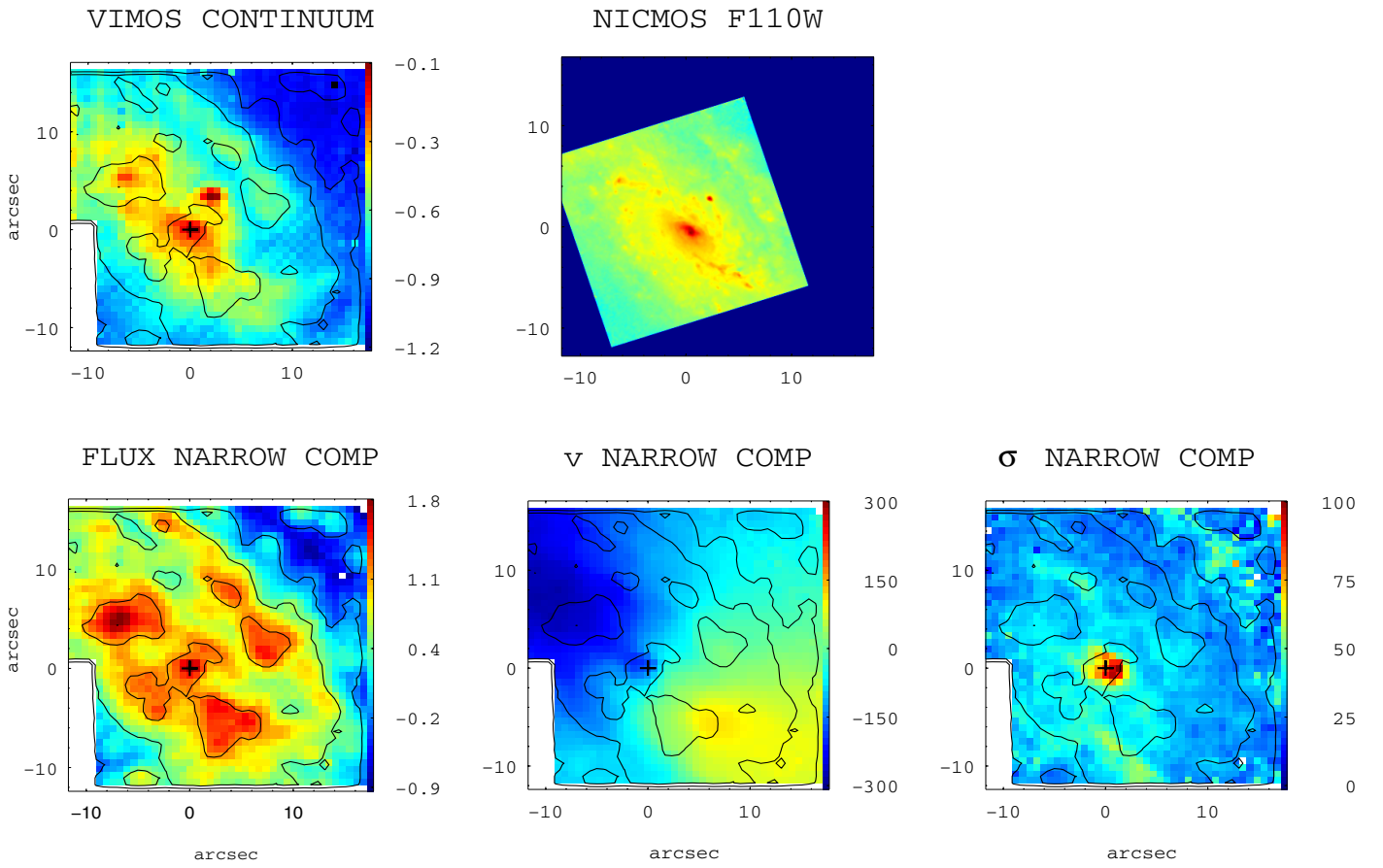


**Fig. A.43.** (General comments about the panels as in Fig. A.1.) IRAS F22132-3705 (IC 5179): the velocity field of this source has the typical “spider-diagram” shape characterizing a rotating *disk*-like object. The kinematic center and the peak of the velocity dispersion map are well defined and coincident with the VIMOS continuum maximum and the  $H\alpha$  flux peak. In the south and northwest there are regions with velocity dispersion of the order of  $50 \text{ km s}^{-1}$ . The spatial scale is  $0.234 \text{ kpc''}$ .

## IRAS F22491-1808

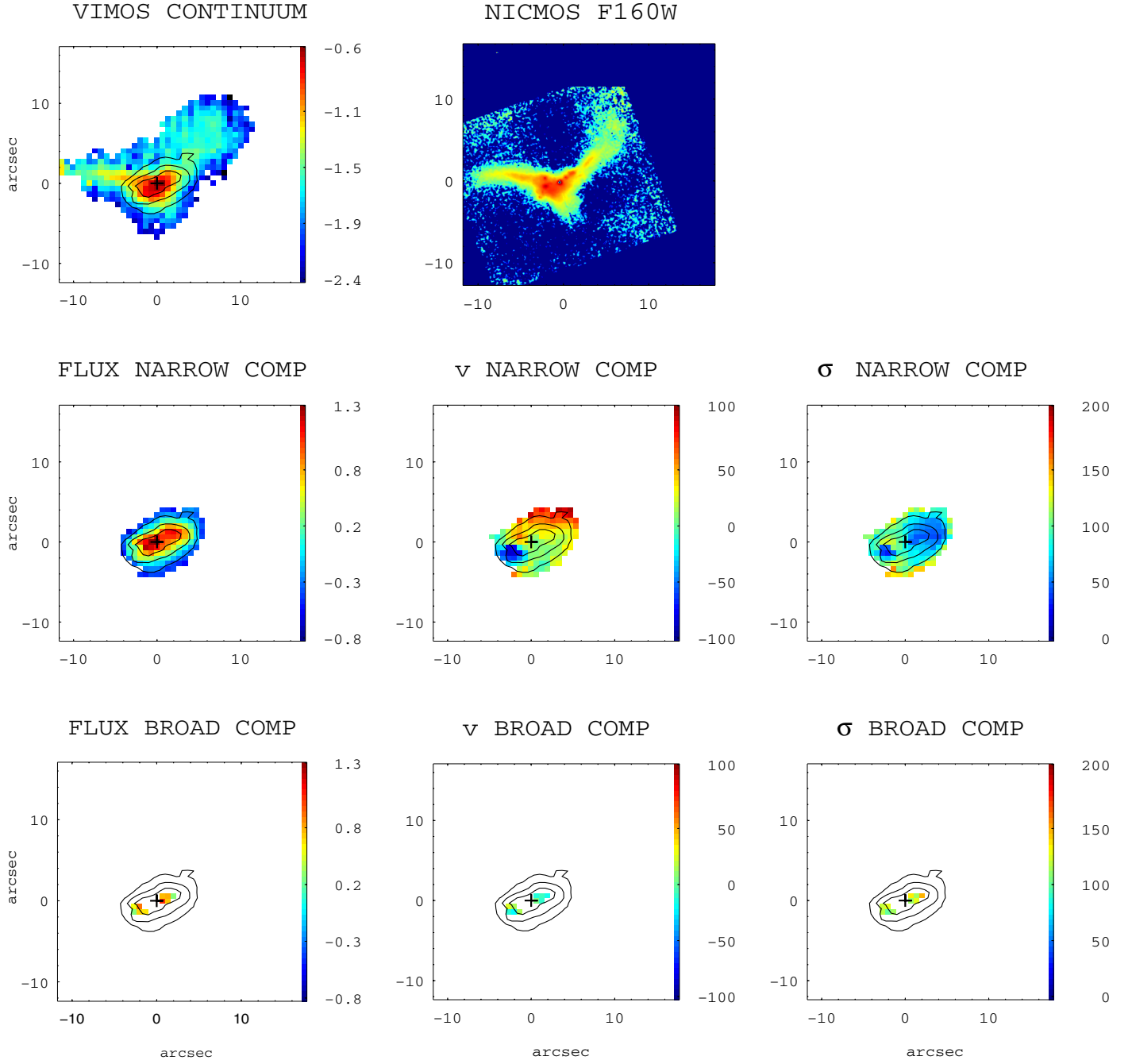


**Fig. A.44.** (General comments about the panels as in Fig. A.1.) IRAS F22491-1808: this is a double nucleus system (separation of 2.6 kpc) with several knots and condensations located in both the nuclear region and the tidal tails observed to the east and northwest of the system. The  $H\alpha$  image shows a more compact morphology than that of the continuum, with no evidence for the already mentioned tidal tails. This system seems to be kinematically disturbed, with a poorly defined minor rotation axis, although a rotation pattern is visible. The velocity dispersion map has a quite irregular structure, with an offset peak with respect to the nucleus and high values in correspondence of low  $H\alpha$  surface brightness. There are two regions where the spectra profiles suggest the presence of an extra broad component. The scale is of 1.47 kpc''.

## IRAS F23128-5919

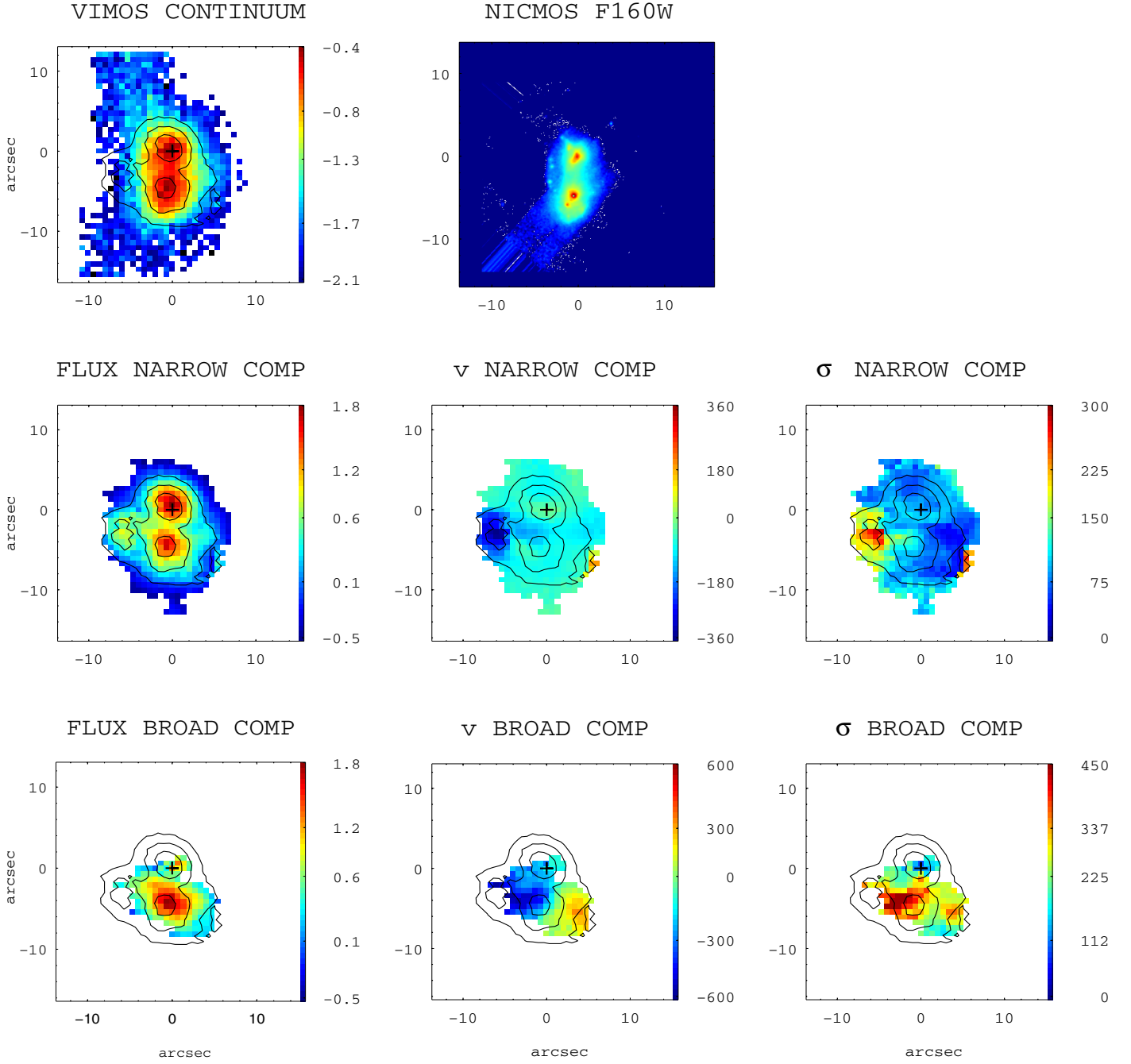


**Fig. A.45.** (General comments about the panels as in Fig. A.1.) IRAS F23128-5919 (AM 2312-591): this is a ULIRG with a double nucleus (separation of  $\sim 4$  kpc). It has not been possible to separate reliably the contribution of each individual galaxy and, therefore, the kinematic values reported in Table 4 correspond to the whole system. The velocity field has a quite complex pattern, where the two galaxies merge their velocity fields. A relatively extended broad component has been found in the inner regions of this system, covering an area of  $55 \text{ kpc}^2$  and with a mean blueshift of  $32 \text{ km s}^{-1}$ . The velocity maps of this second component suggest the presence of a strong outflow. The scale is of  $0.878 \text{ kpc''}$ .

**Table A.1.** Spatial offsets between the VIMOS continuum and H $\alpha$  flux peaks.

Galaxy ID (IRAS)	RA offset (arcsec)	Dec offset (arcsec)	Notes
(1)	(2)	(3)	
F06295-1735	0.7	-2.5	
F06592-6313	0.6	0	
F07027-6011 S	-0.5	0.4	
F07027-6011 N	0	0	
F07160-6215	-1.4	1.6	
F10015-0614	0	0	
F10409-4556	0	0	
F10567-4310	0	0.3	
F11255-4120	0	0	
F11506-3851	3.4	0.1	(a)
F12115-4656	1.9	-0.7	(a)
F13229-2934	0.6	0.5	
F22132-3705	0	0	
F01159-4443 N	0.6	0.4	
F01341/ESO G12	0	0	
F01341/ESO G11	-0.8	0.6	
F06035-7102	0.7	0	
F06076-2139 N	0	0	
F06206-6315	-0.5	0	
F06259-4780 S	-1.0	1.3	
F06259-4780 N	-0.6	0	
08424-3130 S	0	0	
F08520-6850 E	0.6	-0.4	
F09437+0317 S	1.5	0	(a)
F09437+0317 N	0.7	0.6	
12043-3140 N	0	0	
F12596-1529	1.7	-0.6	
F14544-4255 E	-6.7	3.9	(a)
F14544-4255 W	-0.6	0	
F18093-5744 S	0	0	
F18093-5744 C	0	0	
F18093-5744 N	-2.2	2.0	(a)
F22491-1808	-0.7	0	
F23128-5919	0	-0.6	
F04315-0840	0	0	
F05189-2524	-0.4	0	
08355-4944	0	0	
09022-3615	1.1	0	
F10038-3338	0.5	-0.4	
F10257-4339	0	0	
12116-5615	-0.5	-0.4	
F13001-2339	0	0	
F17138-1017	-	-	(b)
F21130-4446	1.2	2.2	
F21453-3511	0	0	

**Notes.** Spatial offsets along the right ascension (RA) and declination (Dec) directions: they are defined as the difference between the position of the H $\alpha$  flux intensity peak and that of the VIMOS continuum (rest frame 6390–6490 Å) intensity peak (i.e.,  $x_{\text{H}\alpha} - x_{\text{cont}}$ ,  $y_{\text{H}\alpha} - y_{\text{cont}}$ ). The coordinates ( $x_i$ ,  $y_i$ ) of the peaks in the maps have been derived as the flux-weighted mean position when considering  $3 \times 3$  spaxels around the maximum intensity value. A typical error of 0.34'' is estimated. For double systems having both galaxies in the VIMOS FoV, the position of the peak refers to the one used as reference to center the images. Column (4): notes with the following code: (a) the peak of the VIMOS continuum image is considered the center of the images since the H $\alpha$  peak corresponds to an extranuclear knot of star formation and does not properly define the center of the galaxy. (b) For this galaxy, it was not possible to identify the VIMOS continuum peak due to the S/N.

## Appendix B: Effective radius determinations based on near-infrared continuum imaging

Rest frame near-IR continuum light traces to first order the bulk of the galaxy stellar component. Here we obtain near-IR-based effective radii  $R_{\text{eff}}$  for the present sample from infrared imaging obtained from the literature. Specifically, we have compiled the  $K_s$ -band images from the 2MASS (Skrutskie et al. 2006), and the existing near-IR imaging obtained with HST in H-band ( $K$ -band HST imaging is restricted to a reduced number of objects). The 2MASS images have the advantage of being available for all the galaxies in the sample and without limitations by FoV. On the other hand, they have a relatively low angular resolution (i.e.,  $\sim 2''$ ), which prevents us from distinguishing kpc-scale structures for many objects in the sample. The HST imaging obviously solves this problem, but in contrast the relatively small FoV of the Near Infrared Camera and Multi-Object Spectrometer (NICMOS) imposes serious limitations for the closest systems. NICMOS/HST H-band infrared imaging existed for about 50 percent of the sample. A few cases were observed with WFC3, which combines good angular resolution and a relatively large FoV.

Two methods have been used to derive the effective radii using 2MASS and HST images: 1) GALFIT (Peng et al. 2010) and 2) the so-called A/2 method, for which the effective radius is defined as  $R_{\text{eff}} = \sqrt{(A/\pi)}$  and where  $A$  is the solid angle subtended by the minimum number of pixels encompassing 50 percent

of the galaxy light for the images considered. GALFIT and A/2 methods agree relatively well: in general, radii smaller than  $\sim 20\%$  are derived when applying the A/2 method. For those cases with clearly defined disks, the GALFIT radii were preferred to those with the A/2 method. For systems with a high ellipticity or with linear structure, GALFIT tends to interpret them as inclined or edge-on disks. This interpretation is correct in some cases, but in others the actual morphology of the system is distorted by tidal forces or it is uncertain. Also, for highly structured images (generally from HST) the A/2 measurements tend to be smaller than those from GALFIT.

The HST-based measurements tend to be smaller ( $\sim 10\%$ ) than the 2MASS ones as a consequence of the relatively small FoV, which often does not cover the whole galaxy emission. Furthermore, the wavelength dependence of the radius measurements between the  $H$ - and  $K$ -bands are expected to be very small. In fact, Veilleux et al. (2002) found that the mean values obtained from  $K$ -band imaging were about 38 percent smaller than those obtained in the optical ( $R$ -band). Assuming conservatively that this difference is mainly due to reddening, one should expect a minor change between the values inferred at  $H$  and  $K$ .

In Table B.1 we present the individual results of the derived effective radii when applying the two methods to the 2MASS and HST images, as well as the adopted values and their estimated uncertainties. The table includes a code that indicates the values considered for deriving the adopted one.

**Table B.1.** Near-IR continuum (stellar) radii determinations.

IRAS name	$R_{\text{hl}}^{2\text{MASS}}$ (kpc)	$R_{\text{hl}}^{2\text{MASS}}$ (A/2) (kpc)	Comm. code	$R_{\text{hl}}^{\text{HST}}$ (kpc)	$R_{\text{hl}}^{\text{HST}}$ (A/2) (kpc)	Comm. code	Adopted (kpc)	code	Previous $R_{\text{hl}}$ (kpc)(ref)
(1)	(2)	(3)	(4)	(5)	(6)	(7)	(8)	(9)	(10)
01159 N	$0.81 \pm 0.32$	$1.30 \pm 0.44$	1,7	...	...		$1.0 \pm 0.4$	1100	
01159 S	$2.39 \pm 0.72$	$2.09 \pm 0.47$	1	...	...		$2.2 \pm 0.6$	1100	
01341 N	$2.56 \pm 0.50$	$2.20 \pm 0.56$		$1.55 \pm 0.65$	$0.95 \pm 0.15$	c	$2.2 \pm 0.6$	1110	
01341 S	$1.50 \pm 0.60$	$0.93 \pm 0.26$	4	...	...		$1.5 \pm 0.6$	1000	
04315	$1.15 \pm 0.35$	$0.94 \pm 0.14$	4	$0.55 \pm 0.30$	$0.36 \pm 0.12$	c	$1.2 \pm 0.4$	1000	0.06 (b)
05189	...	(0.67)	6	(0.10)	(0.25)	h	(0.18)	0000	
06035	...	$4.71 \pm 1.35$		...	...		$4.7 \pm 1.4$	0100	
06076 N	$3.00 \pm 1.40$	$2.21 \pm 0.37$	1	$3.23 \pm 0.06$	...	d	$3.2 \pm 0.6$	1110	
06076 S	$3.40 \pm 1.20$	$1.73 \pm 0.45$	1	$3.11 \pm 0.06$	...	d	$3.1 \pm 0.6$	1010	
06206	(3.60)	(4.56)	5	...	$2.41 \pm 0.60$		$2.4 \pm 0.6$	0001	
06259 N	$1.09 \pm 0.20$	$1.45 \pm 0.58$	1	$1.15 \pm 0.05$	$1.02 \pm 0.02$		$1.0 \pm 0.2$	1011	
06259 C	$1.67 \pm 0.12$	$1.73 \pm 0.35$	1	$2.91 \pm 0.07$	$1.16 \pm 0.04$	f	$2.6 \pm 0.7$	1010	
06259 S	$2.60 \pm 0.50$	$1.74 \pm 0.58$	4	...	$1.14 \pm 0.04$	e	$2.6 \pm 0.7$	1000	
06295	...	$3.03 \pm 0.62$	3	...	...		$3.0 \pm 0.6$	0100	
06592	$1.53 \pm 0.60$	$1.17 \pm 0.26$		...	...		$1.2 \pm 0.4$	1100	
07027 N	...	(0.79)	6	...	(0.2)	h	(0.2)	0000	
07027 S	$1.61 \pm 0.70$	$1.54 \pm 0.69$		$1.75 \pm 0.06$	$0.96 \pm 0.02$		$1.5 \pm 0.5$	1111	
07160	$3.64 \pm 0.35$	$2.32 \pm 0.35$	4	...	$0.82 \pm 0.03$	a,e	$3.6 \pm 0.5$	1000	
08355	$0.91 \pm 0.25$	$1.21 \pm 0.34$		$2.09 \pm 0.38$	$0.91 \pm 0.18$	f	$1.3 \pm 0.8$	1110	
08424 N	$2.50 \pm 1.10$	$0.81 \pm 0.07$	1,4	...	...		$2.5 \pm 0.5$	1000	
08424 S	$2.20 \pm 0.80$	$1.02 \pm 0.10$	1	...	...		$2.2 \pm 0.4$	1000	
08520 E	$2.87 \pm 0.98$	...		$2.36 \pm 0.34$	$2.17 \pm 0.25$	g	$2.4 \pm 0.6$	1010	
08520 W	$4.00 \pm 0.30$	...	4	$5.95 \pm 0.22$	$2.64 \pm 0.30$	g	$5.3 \pm 1.4$	1010	
09022	$1.96 \pm 0.45$	$1.95 \pm 0.40$		$3.25 \pm 0.85$	$2.40 \pm 0.40$	d	$2.2 \pm 0.6$	1111	
09437 N	$6.10 \pm 1.10$	$3.46 \pm 0.71$	4	...	...		$6.1 \pm 1.3$	1000	
09437 S	$3.09 \pm 0.21$	$2.33 \pm 0.39$	4	...	...		$3.1 \pm 0.5$	1000	
10015	$3.56 \pm 0.45$	$2.75 \pm 0.48$		$1.18 \pm 0.18$	$1.36 \pm 0.10$	a	$3.2 \pm 0.6$	1100	
10038	$2.12 \pm 0.70$	$1.96 \pm 0.61$		...	...		$2.0 \pm 0.6$	1100	
10257	$2.66 \pm 0.86$	$1.76 \pm 0.27$		$1.55 \pm 0.04$	$1.33 \pm 0.01$	a,d	$1.8 \pm 0.6$	1100	
10409	$2.92 \pm 0.22$	$2.25 \pm 0.19$		...	...		$2.5 \pm 0.5$	1100	
10567	$2.88 \pm 1.50$	$3.20 \pm 0.40$	2	...	...		$3.2 \pm 0.9$	1100	
11254	$3.14 \pm 0.86$	$2.40 \pm 0.57$	2	...	...		$2.6 \pm 0.7$	1100	
11506	$1.22 \pm 0.20$	$0.94 \pm 0.17$		$0.67 \pm 0.02$	$0.61 \pm 0.02$	c	$1.1 \pm 0.2$	1100	
12042 N	$1.22 \pm 0.20$	$1.18 \pm 0.29$	1	...	...		$1.2 \pm 0.2$	1100	
12042 S	$2.32 \pm 0.32$	$1.47 \pm 0.26$	4	...	...		$2.3 \pm 0.5$	1000	
12115	$2.97 \pm 0.57$	$2.14 \pm 0.36$		...	...		$2.4 \pm 0.6$	1100	
12116	$1.17 \pm 0.35$	$1.34 \pm 0.25$	1	$1.94 \pm 0.88$	$1.12 \pm 0.11$	b,f	$1.3 \pm 0.5$	1110	
12596		$2.17 \pm 0.97$	1	...	$3.13 \pm 0.45$	c	$2.7 \pm 1.0$	0101	
13001	$3.71 \pm 1.00$	$2.89 \pm 1.10$	4	$5.79 \pm 0.15$	$3.33 \pm 0.09$	d	$5.7 \pm 1.5$	1010	
13229	$3.41 \pm 0.85$	$2.39 \pm 0.84$	4	$1.08 \pm 0.09$	$0.87 \pm 0.04$	a	$3.4 \pm 1.2$	1000	
14544 E	$4.76 \pm 0.56$	$2.63 \pm 0.48$	4	$2.66 \pm 0.19$	$1.24 \pm 0.06$	c	$4.8 \pm 1.2$	1000	
14544 W	$3.04 \pm 1.43$	$2.25 \pm 0.51$	2	$1.55 \pm 0.16$	$1.09 \pm 0.12$	a	$2.3 \pm 1.0$	1100	
17138	$1.78 \pm 0.15$	$1.46 \pm 0.25$		$1.44 \pm 0.13$	$1.06 \pm 1.14$	a	$1.7 \pm 0.2$	1100	
18093 N	$1.75 \pm 0.32$	$1.64 \pm 0.35$	1	$1.57 \pm 0.18$	$1.13 \pm 0.08$	a	$1.8 \pm 0.5$	1000	
18093 C		(1.04)	5	$0.39 \pm 0.21$	$0.26 \pm 0.14$	c,g	$>0.3 \pm 0.2$	0011	
18093 S	$2.07 \pm 0.53$	$1.46 \pm 0.30$	4	$1.89 \pm 0.27$	$1.32 \pm 0.09$	c	$2.1 \pm 0.7$	1000	
21130	$4.95 \pm 0.48$	$4.56 \pm 1.21$		...	...		$4.9 \pm 0.8$	1100	
21453	$3.68 \pm 0.51$	$2.97 \pm 0.82$		$2.59 \pm 0.29$	$1.34 \pm 0.08$	a	$3.5 \pm 0.7$	1100	
22132	$5.13 \pm 0.66$	$3.12 \pm 1.15$	2,4	...	$1.11 \pm 0.04$	a,e	$5.1 \pm 0.7$	1000	
22491	$3.70 \pm 1.00$	$3.42 \pm 2.80$	2	...	$3.00 \pm 2.40$	b	$3.6 \pm 1.5$	1101	8.29 (a)
23128	...	$1.91 \pm 0.22$		...	$1.60 \pm 0.22$		$1.8 \pm 0.3$	0101	

**Notes.** Columns: (1) Identification. (2) Half-light radius from the 2MASS *K*-band image using GALFIT. (3) Half-light radius from the 2MASS *K*-band image using the A/2 method (see text). (4) Comments associated with the 2MASS images determinations, according to the following code: 1- large uncertainties when applying the A/2 method due to galaxy decomposition; 2- uncertainty due to background value, field stars, and/or complex structure; 3- GALFIT could not obtain a reliable fit; 4- disc with  $b/a < 0.4$ , leading to discrepancies between the two methods; 5- unreliable estimates due to background and/or complex structure; 6- point-like source dominating the (unreliable) radius determination; 7- FWHM of the bulge component close to the value for the PSF, making the radii estimates uncertain. (5) Half-light radius from the HST *H*-band image using GALFIT. (6) Half-light radius from the HST *H*-band image using the A/2 method. (7) Comments associated with the HST determinations, according to the following code: a- severely limited by FoV; b- very uncertain results due to bad background definition; c- limited by FoV; d- HST image obtained with WFC3 or NIC3 (instead of NIC2); e- bad GALFIT fit; f- rich structure in the HST image; g- uncertainties when applying the A/2 method due to galaxy decomposition; h- point-like source dominating the (unreliable) radius determination. (8) Adopted values. (9) Code indication if the individual values in columns 2, 3, 5, and 6 were used in the adopted value (0 = not used, 1 = used). (10) Previous determinations with the following code: (a) [Scoville et al. \(2000\)](#), model fitting (de Vaucouleurs or exponential) to F160W images; (b) [Hinz & Rieke \(2006\)](#).